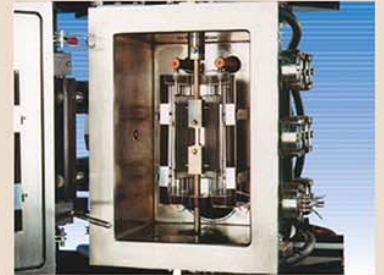




The Scientific Bulletin of Valahia University MATERIALS and MECHANICS



2019

Vol. 17 No. 17

STRUCTURAL AND PIEZOELECTRIC CHARACTERIZATION OF Pr³⁺ MODIFIED (1-x)Pb(Zr_{1-y}Ti_y)O₃ – xPb(Mn_{1/3}Sb_{2/3})O₃ CERAMIC

Alina Iulia DUMITRU¹, Georgeta VELCIU¹, Jana PINTEA¹, Delia PATROI¹, Virgil MARINESCU¹, Florentina CLICINSCHI¹, Ildiko PETER^{*2}

¹National Institute for Research & Development in Electrical Engineering ICPE-CA, 313 Splaiul Unirii, 030138, Bucharest, Romania

²University of Medicine, Pharmacy, Science and Technology „George Emil Palade”
Faculty of Engineering and Information Technology Gheorghe Marinescu 38
Targu Mures, Mures, 540139, Romania

E-mail: ildiko.peter@umfst.ro

Abstract: *0.88Pb(Zr_{0.52}Ti_{0.48})O₃ – 0.12Pb(Mn_{1/3}Sb_{2/3})O₃ – 0.02 at%E piezoelectric ceramics, with E = Pr³⁺ were synthesized by using a conventional method, namely a solid state reaction technique. X-ray diffraction (XRD) and Scanning Electron Microscopy (SEM) were employed for the structural and microstructural investigations. Piezoelectric methods were used for the dielectric and piezoelectric properties determination. The results of XRD show a perovskite structure and XRD patterns, indexing on a tetragonal cell structure, was carried out for the most common phases. The SEM micrographs of the sintered compositions reveal a homogenous structure with a sharp or rounded grain boundary. The modified PZT ceramic presents still superior piezoelectric properties. Based on the results obtained, one can conclude that the analysed piezoelectric ceramics are useful for device applications.*

Keywords: *PZT ceramics, solid state reaction, XRD, SEM, piezoelectric properties*

1. INTRODUCTION

Piezoelectric ceramic represents an intelligent functional material. In such materials one can talk about electrical energy as a results of mechanical energy. Piezoelectric ceramics have been extensively employed in various significant industrial applications because of their higher characteristics.

Because of their excellent properties the lead zirconate titanate (PZT) piezoelectric ceramics with different dopants are potential materials for electromechanical device applications like sensors, actuators and transducers [1, 2]. Largely used lead based materials where perovskite structure is predominant are the most widely used [3-5]. Lead zirconate titanate [Pb(Zr_{1-x}Ti_x)O₃, PZT] solid solution is the typical arrangement of the lead involved piezoelectrics with a composition near to the morphotropic phase boundary (MPB), where the higher dielectric/piezoelectric characteristics have been reported in [6-8].

Pb(Zr_xTi_{1-x})O₃ (PZT) based perovskite-form materials has broadly explored and effectively can be considered as a functional pioneering material [9-11].

Pb(Zr_xTi_{1-x})O₃ is rarely used in it's pure form. Commercially used PZT ceramics have been produced through doping to acquire all the requests necessary for the employment [12,13]. Usually when PZT is doped

with acceptor ions are obtained “hard” PZTs and when PZT is doped with donor ions are obtained “soft” PZTs.

The behaviour of such PZT systems associate simultaneously an extraordinary mechanical quality factor (Q_m) with a high electromechanical coupling factor (k_p) and reduced dielectric loss (tan δ).

Pb(Mn_{1/3}Sb_{2/3})O₃-PZT (PMS-PZT) arrangement possess excessive electromechanical coupling factor (k_p) and high mechanical quality factor (Q_m) [14,15]. The aforementioned higher properties suggest that for the PMS-PZT structure can be considered as a perfect element for applications such as piezoelectric transformers [16–18].

The goal of the present study is related to the investigation of the effect of Pr³⁺ addition on the structural and microstructural behavior in conditions when a variation of the temperature occurs. The dielectric constant and dielectric losses of the PMS-PZT-Pr ceramic has been investigated in relation with the temperature. The electrical properties have been considered too.

2. EXPERIMENTAL PROCEDURE

0.88Pb(Zr_{0.52}Ti_{0.48})O₃ – 0.12Pb(Mn_{1/3}Sb_{2/3})O₃ – 0.02 at% Pr³⁺ abbreviated PZT-Pr was obtained by the high temperature solid-state reaction technique. High purity reagent powders of PbO (Fluka), ZrO₂ (Merck), TiO₂ (Aldrich), MnCO₃ (Carlo Erba), Sb₂O₃ (Merck) and

Pr_6O_{11} (Aldrich) were balanced and mixed in distilled water for 6h. The combination has been further calcinated at 840°C for 4 hours. The obtained powder has been re-milled in distilled water for 10h. The resulting suspension, has been dried at 80°C in the furnace followed by mixing with 5% aqueous solution of polyvinyl alcohol (PVA), as a binder, and then has been compacted uniaxially (70 MPa) obtaining a discs (12 mm diameter and 1.5 mm height). The samples prepared in this way have been sintered in a range of 1100°C - 1200°C with a holding time of 2 h. Sintering procedure has been carried out at high temperature using a Carbolite type furnace, with a heating/cooling rate approx. 50°C. The sintered samples have been polished to 0.8 mm depth and metalized with Ag glue on both edges and then heated to 650°C with a holding time of 30 min. The as prepared samples were finally polarized under a dc electric field at 3 kV / mm in Si oil at 120°C for 30 min. in order to determine the piezoelectric properties.

Archimedes method and distilled water as medium has been used for the measurement of the sintered samples densities. X-rays diffraction (XRD, BRUKER AXS D8 Advance) with $\text{CuK}\alpha$ radiation and Ni filter has been employed for the determination of the crystallite structure in the sintered materials. The evolution of the microstructure and the development of the various phases have been identified by field emission scanning electron microscope (FESEM-FIB Workstation Auriga, Carl Zeiss, Germany). LCR meter (HAMEG type), at 1kHz serves for the dielectric properties (dielectric constant and loss) measurements. The piezoelectric properties have been studied using a resonance-antiresonance approach with an impedance analyzer 4294A (Agilent type). Calculation of the electromechanical coupling factor (k_p) has been performed starting from the resonance and anti-resonance frequencies.

3. RESULTS AND DISCUSSION

The optical micrographs realized on the welded joints which are carried out by single and double joining pass and the results are illustrated in Figures 1 and 2.

The XRD results of the PZT-Pr sintered discs are shown in Figure 1.

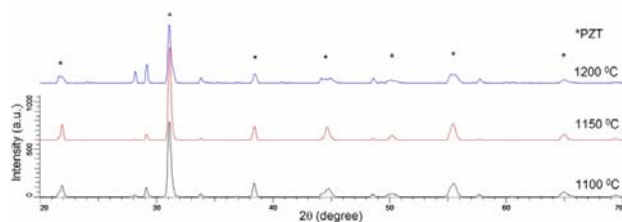


Figure 1. XRD pattern of the sample PZT-Pr thermally treated for 2 hours at 1100°C, 1150°C and 1200°C

XRD measurements indicate mostly perovskite phase with a tetragonality $c/a=1.0143$ for PZT-Pr sintered at 1200°C. The tetragonality as calculated from XRD data and given in Table 1 and reveals a slight deviation when the sintering temperature increases.

Table 1. The tetragonality (c/a ratio) and the crystallite size (D) for PZT-Pr versus sintering temperature

Samples	$T_{\text{sintering}}$ (°C)	c/a	D (nm)
PZT-Pr	1100	1.0102	100.0
	1150	1.0065	118.2
	1200	1.0143	105.0

Density and porosity measurements have been reported in Table 2 with a real indication of the material's densification which is performed during sintering. The outcomes obtained are in a good agreement with the morphological analysis, where for all sintered samples a dense microstructure has been obtained.

Table 2. The physical properties for PZT-Pr versus sintering temperature

Sample	$T_{\text{sintering}}$ (°C)	Porosity (%)	Density (g/cm^2)
PZT-Pr	1100	0,89	7,53
	1150	0,51	7,62
	1200	0,47	7,72

The micrographs (Figure 2) shows a compact behaviour where the distribution of the different grains has been conditioned by the sintering temperature; the dimension of the grains increases as the temperature increases and clear presence of the secondary phase has been revealed in the structure. In all the sintered PZT-Pr the formation of larger plates has been observed too.

For the sintered samples the semi-quantitative chemical composition was verified by EDS analysis. The SEM micrographs correlated with the chemical composition are presented in Figure 3. It is observed that the samples do not contain other impurities, fact confirmed by XRD analysis too.

Table 3 reports the result achieved for the dielectric and the piezoelectric constants. The values of the relative dielectric const. ($\epsilon_r = \epsilon_{33}^T/\epsilon_0$) as well as the loss angle tangent ($\tan\delta$) are directly associated to the sintering temperature and show a real dependance with respect to this parameter. Calculation of the electromechanical coupling factor (k_p) has been carried out using the resonance frequency and antiresonance frequency .

P-E loops for poled PZT-Pr ceramics are presented in Figure 4. The connection of the hysteresis loops and the sintering temperature is reported in Figure 4. A large strain is obtained for the poled samples. The values of the remaining polarization (Pr) and the maximum polarization (Pmax) for the poled PZT-Pr composition in relation with the temperature used for the sintering has been shown in Table 4.

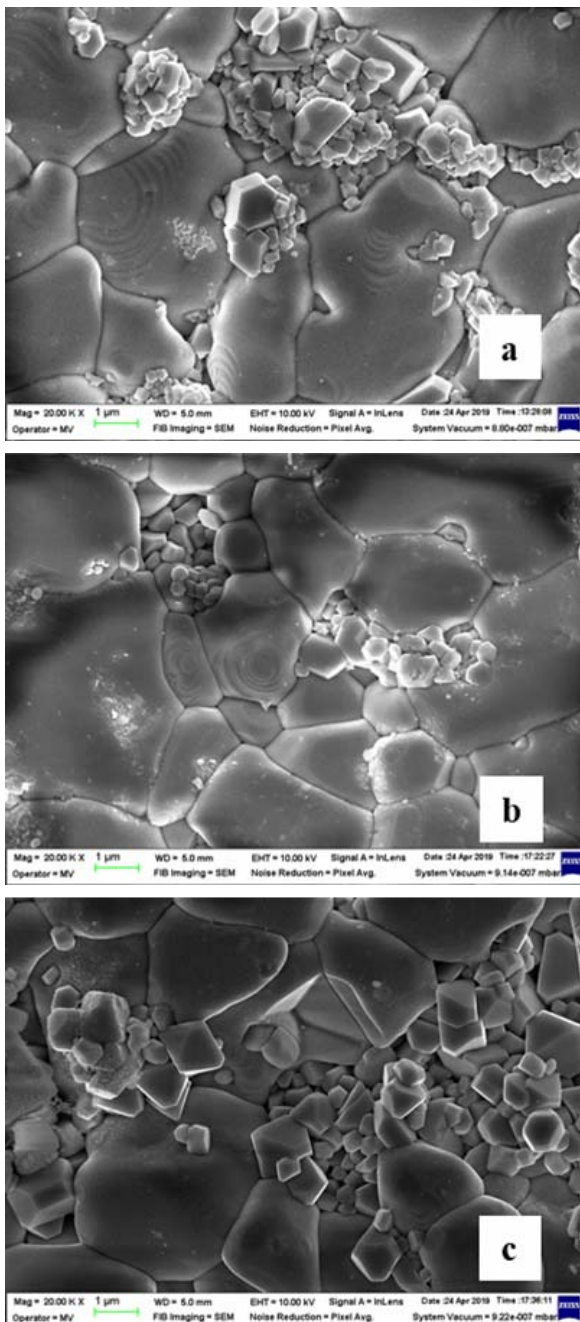


Figure 2. SEM images of samples PZT-Pr thermally treated for 2 hours at (a) 1100°C, (b) 1150°C and (c) 1200°C

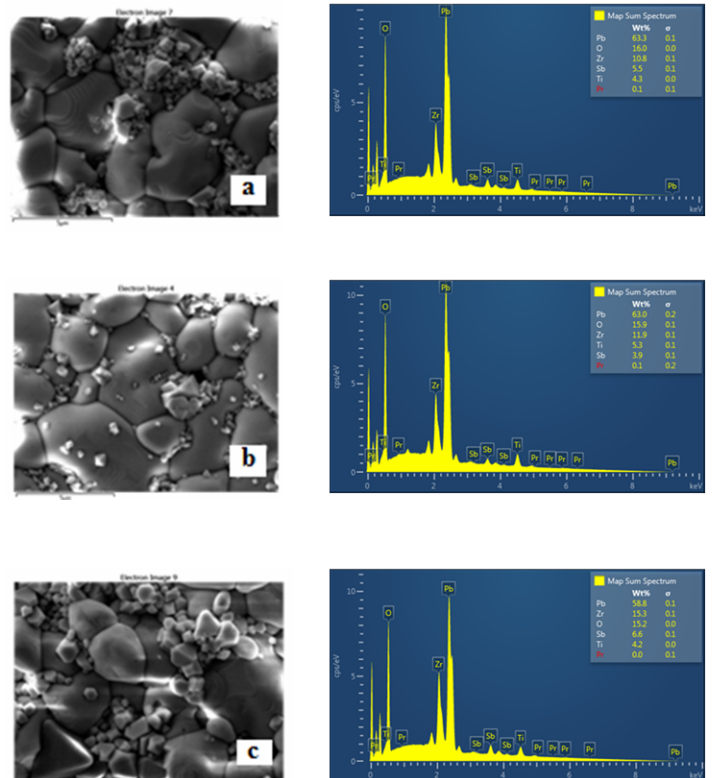


Figure 3. SEM microscopes and chemical composition for MP-Pr sintered for 2 hours at (a) 1100°C, (b) 1150°C and (c) 1200°C

Table3. The dielectric and piezoelectric properties for PZT-Pr versus sintering temperature

Sample	T _{Sintering} (°C)	ε _r	tgδ	k _p
PZT-Pr	1200	1180	6,68*10 ⁻³	0,24
	1150	1233	10,2*10 ⁻³	0,29
	1100	-	-	-

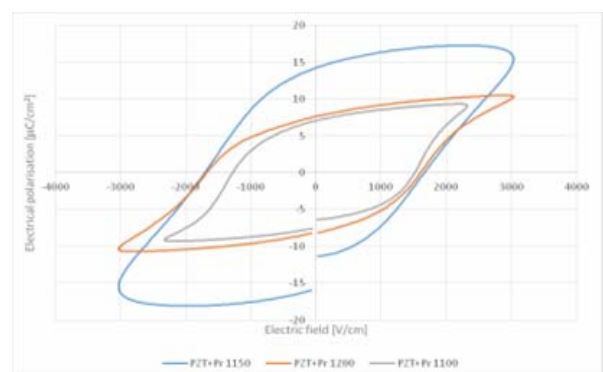


Figure 4. Hysteresis loops obtained for poled PZT-Pr samples sintered at 1100°C, 1150°C and 1200°C after poling

Table 4. The values of the remaining polarization (Pr) and the maximum polarization (Pmax) for the poled PZT-Pr composition versus sintering temperature

Type of material	Sintering Temperature (°C)	Up [V]	Pr [$\mu\text{C}/\text{cm}^2$]	Pmax [$\mu\text{C}/\text{cm}^2$]
PZT-Pr	1100	2500	7.07	9.11
	1150	2600	14.23	15.43
	1200	2900	7.63	10.33

4. CONCLUSIONS

In the present paper some consideration related to the configuration and to the electrical characteristics of 0.02 at% Pr^{3+} doping the $0.88\text{Pb}(\text{Zr}_{0.52}\text{Ti}_{0.48})\text{O}_3 - 0.12\text{Pb}(\text{Mn}_{1/3}\text{Sb}_{2/3})\text{O}_3$ ceramics were reported. Solid-state reaction technique was employed for the samples preparation at high temperature. The major phase obtained is the tetragonal perovskite phase. The density and porosity are influenced by the sintering temperature. The values of the electromechanical coupling factor (k_p) and of the relative permittivity (ϵ_r) as well as the value obtained for the remaining polarization gives a good set of values for the electrical properties. These characteristics are useful for the proposed device applications.

REFERENCES

- [1] Haertling G H 1999 J. Am. Ceram. Soc. 82 797–818
- [2] Fan F Q and Kim H E 2001 J. Am. Ceram. Soc. 84 636–8
- [3] B. Jaffe, W.R. Cook Jr., H. Jaffe, Piezoelectric Ceramics, Academic, New York, 1971.
- [4] Y.H. Xu, Ferroelectric Materials and their Applications, North-Holland, Los Angeles, 1991.
- [5] L.E. Cross, in: N. Setter, E.L. Colla (Eds.), Ferroelectric Ceramics, Birkhäuser, Basel, 1993, pp. 1–85.
- [6] D. Damjanovic, N. Klein, J. Li, V. Porokhonsky, What can be expected from lead-free piezoelectric materials, *Funct. Mater. Lett.* 3 (2010) 5–13.
- [7] G.H. Haertling, Ferroelectric ceramics: history and technology, *J. Am. Ceram. Soc.* 82 (1999) 797–818.
- [8] L. Jin, Z. He, D. Damjanovic, Nanodomains in Fe³⁺-doped lead zirconate titanate ceramics at the morphotropic phase boundary do not correlate with high properties, *Appl. Phys. Lett.* 95 (2009) 012905.
- [9] R.Yimnirun, S. Ananta and P. Laoratanakul: *Mat. Sci. Eng. B* Vol. 112 (2004), p. 79
- [10] T.Y. Zhang and C. F. Gao: *Theor. Appl. Fract. Mec.* Vol. 41 (2004), p. 339
- [11] C.H. Wang, S.J. Chang and P.C. Chang: *Mat. Sci. Eng. B* Vol. 111 (2004), p. 124
- [12] V. Porokhonsky, L. Jin, D. Damjanovic, Separation of piezoelectric grain resonance and domain wall dispersion in $\text{Pb}(\text{Zr,Ti})\text{O}_3$ ceramics, *Appl. Phys. Lett.* 94 (2009) 252906.
- [13] L. Jin, V. Porokhonsky, D. Damjanovic, Domain wall contributions in $\text{Pb}(\text{Zr,Ti})\text{O}_3$ ceramics at morphotropic phase boundary: a study of dielectric dispersion, *Appl. Phys. Lett.* 96 (2010) 242902.
- [14] X.B. Guo, H.Y. Chen and Z.Y. Meng: *Key. Eng. Mat.* Vol. 224-2 (2002), p. 105
- [15] J.W. Long, H.Y. Chen and Z.Y. Meng: *J. Inorg. Mater.* Vol. 19 (2004), p. 101
- [16] Yoon J, Kang H W, Kucheiko S I and Jung H J 1998 *J. Am.Ceram. Soc.* 81 2473–6
- [17] Gao Y K, Uchino K and Viehland D 2002 *J. Appl. Phys.* 92 2094–9
- [18] Zhu Z G, Li B S, Li G R and Yin Q R 2005 *Mater. Sci. Forum* 475 1145–8

SPECIAL BINDING FOR REFRACTORY CONCRETES

Elena Valentina STOIAN, Dan Nicolae UNGUREANU, Florin TOMA, Alexandru Gabriel COLȚA, Daniel ANCULESCU, Vasile BRATU, Nicolae ANGELESCU

Faculty of Materials Engineering and Mechanics, Valahia University of Targoviste, 13 Aleea Sinaia Street,
Targoviste, Romania

E-mail: danungureanu2002@yahoo.com

Abstract: *The paper shows data related to coexistence of various binding systems, which could be present during the hardening of special concretes. It is taken into account the Ultra Low Aluminous Cement Concretes additivated with different materials (phosphates and mineral ultra dispersed powders - Condensed Silica Fume, Hydrated Alumina etc). In correlation to the pH-value, these substances can favour the forming of new binding systems besides the hydraulic binder (which is not important in this case). The new system is the coagulation binding form. The coagulation binding system has a very important role in the advanced compactness and in the increasing mechanical strengths of concrete structures.*

Keywords: *Special concretes, Coagulation binding, pH-value, Refractory properties*

1. INTRODUCTION

The concrete is a composite material consisting in a binding matrix which is a continuous phase, and an aggregate representing the non-continuous phase. The concrete mechanical-structural properties are directly correlated to the quality of the binding matrix; the higher the properties of this matrix are – an uniform distribution, a reduced porosity, a high density and a good cohesion – the better the concretes. In view to obtain a good concrete matrix, different substances [1-12] are used with or without cement. These substances favour the development of a complex hardening system by the simultaneous existence of several binding types; the hardened concretes obtained as described above have high mechanical-structural characteristics. Thus, the new generations of concrete, with low and ultra low cement, have been so obtained [3, 12-15].

The coagulation-condensation binding system is developed both in the presence or absence of hydraulic binding. The developing of the coagulation binding system take place only for a certain pH value.

The used binding substances, which provide an optimal pH-value of the as hardening solution from the monolithic system and which, thus, can develop a new binding-type (i.e. coagulation) based on adhesion forces, are, mainly, organic by nature, as: dextrine, carboxymethocel, polyvinyl alcohol, vinyl polymers, phenol resins etc.

Also, another category of materials anorganic by nature is known, which is able to generate adhesion binding

forces between the particles of the as-hardening monolithic system (i. e. aluminium phosphates and natrium silicates).

Several theories regarding process ensuring the adhesive forces evolution between the particles of the hardened monolith, all of them representing the premise for the binding process by coagulation, the most plausible ones being as follows [3, 4, 7, 10]:

- the theory of adsorption due to the forces between molecules, which are Van der Waals forces;
- the theory of diffusion; the binder molecules and those of the components of monolithic material diffuse between them at the high temperature, thus, generating a diffusion layer concomitantly realizing a very strong binding structures;
- electrostatic theory. According to this theory, between the electrolyte and the particles of the concrete, a double electrostatic layer is obtained. The attractive force of this double electrostatic layer is the reason of the genesis and development of the new binding system.

Besides the three above emphasized theories concerning the coagulation binding system, both chemical binding and mechanical binding theories could be mentioned.

The utilisation of electrolytes – depending on the medium with an optimal pH-value in order to establish the conditions of formation and development of the coagulation binding, stipulates the presence within the system of fine clay-powders, of ultra fine refractory oxides powders (i. e. SiO₂, Al₂O₃, TiO₂, Cr₂O₃, etc.) and silica, alumina soils or aluminosilicate soils.

The coagulation binding is the result of a close contact between the fine particles (in colloidal state), which is realised by Van der Waals forces for a certain optimal pH-value.

When the colloidal particles of the system are very strong approaching one to another consequence of the Van der Waals forces, a rejection force between them appears due to the interposition of the electrostatic double layer.

The coagulation system formation of ultra fine colloidal particles and the stability of this system depend on the ratio between attractive and rejection forces, which appear between these particles [3]. The combined curve of the potential energy for both types of forces is shown in Fig. 1.

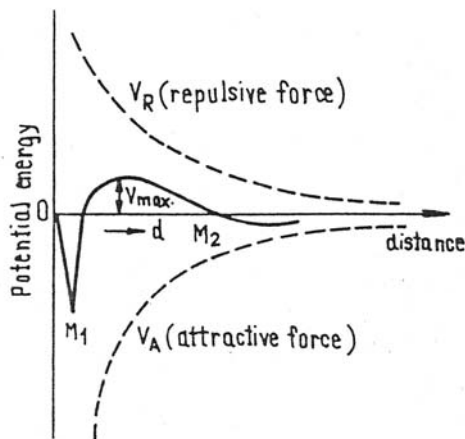


Figure 1. The relationship between the potential energy and the distance of particles

When the colloidal particles are approaching one to another at a distance sufficient to surpass the potential barrier $-V_{max}$, these ones will coagulate due to the fact that the attractive forces are stronger than the rejection forces.

The coagulation process takes place only by overcoming the rejection forces resulting from the electrostatic double layer interposition. In order to diminish the intensity of rejection forces, an electrolyte has to be supplementary added to the colloidal solution. By this way, a lot of ions which are specific to the electrolyte penetrate the electrostatic double layer, a phenomenon which subsequently impedes the ionic equilibrium and determines the tapering of the electrostatic double layer. By the depreciation of the electrostatic double layer, the rejection forces intensity between the colloidal micro particles within the system is lowered, too. If the intensity of the attractive forces is higher than the intensity of the rejection forces, the potential barrier shall be broken-down (surpassed) and the potential energy becomes null i.e. the so-called "isoelectric point".

Certain pH-values correspond to the isoelectric point, depending on the charge density on the dispersed particles surfaces and of their chemical composition. The disperse system of the mentioned oxides, including the mixt oxide system show corresponding values ranging between approximately 2,7-for SiO_2 , 4,6-for TiO_2 , 6,9-for Cr_2O_3 (see [3, 7]) and approximately 9-for Al_2O_3 , values which are inferior to those of aluminous cement suspensions, with pH 12 - fig. 2. The coagulation can be controlled by adding some electrolytes.

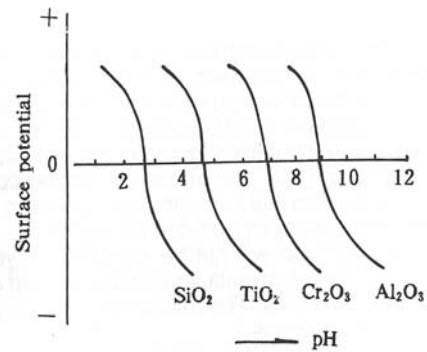


Figure 2. The relationship between the isoelectric point and the pH-value

For a certain pH-value of the as-hardening existent solution in the studied medium, a value which is determined function of the compounds nature, the coagulation process - more or less rapid - of some soils (suspensions), as those resulting from very fine clay-powders (aluminosilicate systems) or oxide-powders (as silicon dioxide- SiO_2 , titanium dioxide TiO_2 , alumina - Al_2O_3 , chromium oxide - Cr_2O_3 etc.).

2. RAW MATERIALS AND WORKING METHODS

An aluminous cement, containing 72.6% Al_2O_3 and 23.89% CaO was used as an agent of hydraulic binding. The proportion of aluminous cement is ranging between 1 and max. 5%, corresponding to the Ultra Low Cement Concretes. The fine powders of condensed silica fume (CSF) and special hydrated alumina (HA) represent the carriers of the coagulation binding system. This mineral powders were used at the value of ratio $\text{HA/CSF} = 1.88$. The electrolyte (powder phosphate which is soluble in water), acts as a pH regulator of the aqueous systems, during hardening process, and at the same time, possible, as an admixture for the chemical binding. As aggregate it was used the Clay D79 (STAS 4915/1976). Table 1 shows the main chemical properties of the raw materials.

The experimental concrete samples were realised by casting - vibration. In order to estimate the mechanical resistance, the porosity and volume mass of the monolithic, the samples with the dimensions 40 x 40 x 160 mm were shaped. After two days of free hardening, the samples, which were shaped as mentioned above, were dried at 110°C until constant weight is obtained and, thereafter, were heated at different temperatures.

Table 1. The chemical composition of raw materials

Chemical analyse, %						
Raw material	Al ₂ O ₃	SiO ₂	Fe ₂ O ₃	Alkali	CaO	Loss of ignition
Special Hydrated Alumina (AH)	64.6	0.03	0.025	0.35	-	34.8
Condensed Silica Fume (CSF)	0.46	87.5	1.73	1.20	1.1	-
Clay D79	55.2	36.6	1.78	0.2	1.3	-
Aluminous Cement	72.60	0.54	0.42	1.69	-	-
Aluminium Phosphate	P ₂ O ₅ = Minimum 55.7%					

3. RESULTS AND DISCUSSIONS

Further is presented the influence of the electrolyte on the obtaining of optimal pH conditions in order to develop the coagulation binding system. The working procedure consists in preparing a binding matrix mass which emphasizes an increasing aluminium phosphate ratio [see 16, 17, 18].

In table 2 are shown the mechanical and structural properties of the matrix prepared with following ratios: Hydrated Alumina / Cement = 1.7 and Condensed Silica Fume / Cement = 1.0. The data from table 2 show that although the cement can be found in the system, this process will not occur for the all investigated masses. The coagulation hardening doesn't take place (mass 1) or takes place at insignificant level (masses 2-5) due to

improper pH conditions (ph = 5.5 – 7.5) specific to the investigated binder. On the other hand, when the medium of the hardening system reaches the value pH = 4 (masses 6-8) the coagulation binding is initiated at a significant level (Compression Strength - Rc = 250-340 daN/cm², Porosity – P = 18 – 23%), the binding process being developed at an important scale (masses 9 – 11) for pH = 3.5 (Rc = 429 -532 daN/cm²) and completed (masses 12-14) for pH = 3 (Rc = 586 – 615 daN/cm², P = 14 – 15%). For pH = 3, when the coagulation binding process is completed, the resulting structures have performant mechanical and structural properties being less usual ones in the case of the current hardening systems. In such conditions the resulting structures are highly compact (P = 14%) and the developed mechanical resistance amounts to 615 daN/cm².

Table 2. The developing of the coagulation system for optimal values in the case of the matrix with AH/Cement = 1.7 and CSF/Cement = 1.0, at 110⁰C after 2 days under normal hardening conditions

Crt No	P ₂ O ₅ , %	Water Necessary, %	pH	Compression Strength, daN/cm ²	Porosity, %
1	0	30	7,5	-	-
2	0,32	25	6,0	-	-
3	0,45	23	6,0	18	-
4	0,64	20	5,5	36	-
5	0,80	15	5,5	58	32
6	0,96	12,7	4,0	250	23
7	1,12	11,26	4,0	277	21
8	1,25	10,35	4,0	340	18
9	1,44	9,72	3,5	429	19
10	1,61	8,86	3,5	486	17
11	1,77	8,17	3,5	532	16
12	1,93	7,5	3	615	14
13	2,09	7,0	3	586	15
14	2,25	6,35	3	500	16

By rigorous trials, repetead several times, one could find out that the coagulation binding process performed at optimal pH values, when are used the Condensed Silica Fume (CSF) and the Hydrated Alumina (HA) - as mineral powders and the Calcium Aluminate Cement, take place also by using the Clay D79 as aggregate. So,

one should observe the pH values of the wet medium within the system which enables the new binding system to induce positive influences on the mechanical and structural properties when using the Clay D79 as refractory aggregate. Therefore, binding masses were prepared, 91% consisting of the Clay D79, the rest being

represented by Hydrated Alumina, Condensed Silica Fume, Calcium Aluminate Cement. After a good mixing of the investigated mass, to this one will be added different ratios of electrolyte (Soluble Aluminium Phosphate) in order to obtain optimal pH conditions, for which the binding system is characterized by high mechanical properties, during the normal hardening process and the heat treatment, table 3.

The coagulation binding system proves to be formed also by using Clay D79 as refractory aggregate, table 3. In table 3 are presented the results of some investigations made on concretes with Clay D79, under various pH values in drying and heat treatment conditions after two days of free hardening.

Table 3. Concretes bound by coagulation with the Clay D79 for HA/ Cement = 1.7 and CSF/ Cement = 1.0 dried and heat treated after two days of free hardening

Crt No	P ₂ O ₅ , %	Water Necessary, %	pH	Heating Temperatures, °C	Compression Strength, daN/cm ²	Porosity, %	Bulk Density, g/cm ³
1	1,7	5,8	4,5	110	70	-	-
				800	167	24	2,02
				1500	400	17	2,03
2	2,25	5,0	4,0	110	220	23	2,04
				800	250	23	2,03
				1500	738	18	2,03
3	2,73	3,5	3,5	110	286	23	2,04
				800	316	23	2,03
				1500	909	17	2,03
4	3,0	2,7	3,5	110	350	23	2,06
				800	400	23	2,05
				1500	936	16	2,05
5	3,38	2,2	3,0	110	425	20	2,07
				800	560	20	2,06
				1500	1100	15	2,06
6	3,54	2	3,0	110	400	21	2,06
				800	526	21	2,05
				1500	1000	15	2,05
7	3,7	2	3,0	110	360	23	2,05
				800	450	23	2,04
				1500	920	16	2,05

The coagulation binding is intensified as the pH values range from 4.5 to 3, as well as in case of the tests performed on the binding matrix (without aggregate - see table 2), the coagulation hardening process reaches its maximum intensity for pH = 3 (mass 5), when the developed mechanical strength is 425 daN/cm² on the dry sample at 110°C. The same sample shows Rc 560 daN/cm² after 800°C heating and, respectively, 1100 daN/cm² after 1500°C heating. This mass emphasizes, under the mentioned treatment conditions, compact structures (Porosity = 15-20%). At the same time it is interesting and also important to show that the mechanical strength at 800°C (the value belonging to the critical range of temperatures for refractories with a hydraulic binding system or chemically bound masses) is clearly superior to the strengths of the respective mass, emphasized at normal hardening and then dried at 110°C.

Also, there is no evidence of a porosity increase for samples after they were heated at 800°C as compared with the value emphasized by drying. This reality sustains the conclusions that monolithics bound by

coagulation are not negatively influenced by the rising of temperature up to the critical point. Thus, one can assert that monolithics bound by coagulation do not show inferior mechanical and structural properties within the range of temperatures between 400°C and 900°C, as well as it is happening very intensively in the case of refractory concrete with the usual cement dosage (20%). The devaluation of the mechanical strengths and structural properties, which occurs, generally, within the critical range of temperatures, appears also at modern generation concrete types (concrete with low cement dosage), but the phenomenon of devaluation is decreasing by diminishing the cement content of concrete. This work does not contain any approach of the strength devaluation phenomenon.

Thus, a beneficial behaviour can be explained by the fact that under heat treatment conditions, the texture and structure of new refractory monolithics bound by coagulation, are not deeply altered. When the temperature increases, the structure of these monolithics is sufficiently stable, but it still suffers a compacting

process, fig. 3, confirmed by the determinations of distributive porosity, fig. 4.

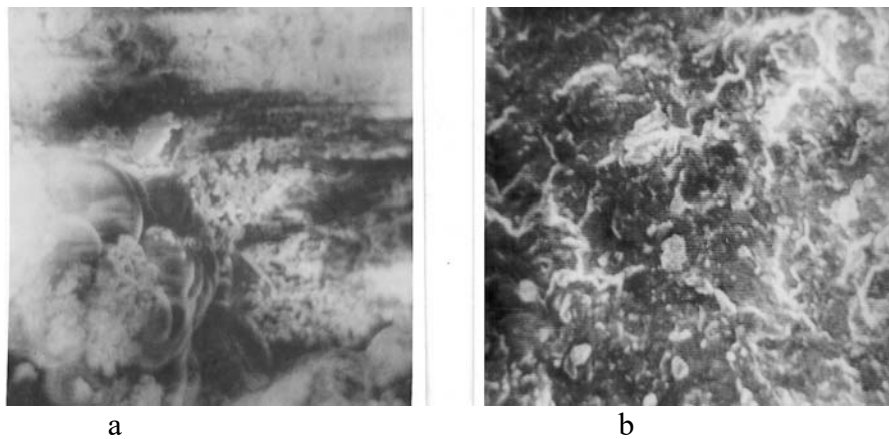
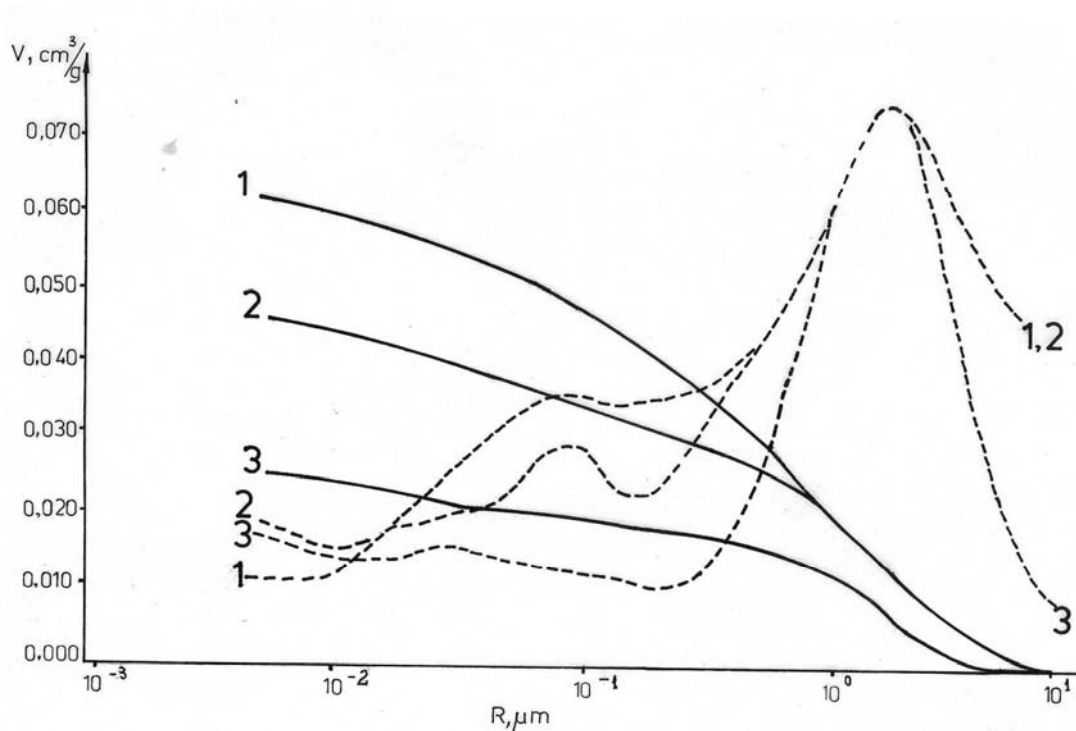


Figure 3. The microstructure of the new type concrete after two days of free Hardening (x 1000): a. Concrete 110°C dried; b. Concrete heat treated at 800°C

Although the distributive porosity graphs of the 800°C and 1500°C treated samples - fig. 3, are similar to that corresponding to the same hardened sample under normal conditions and 110°C dried, the share of pores

having the radius less than 1 μ decreases all the more as the treatment temperature is higher. The consequence of the compaction process is the increase of the mechanical strengths.



**Figure 4. Distributive porosity of concretes after two days of free hardening:
1. Sample 110°C dried; 2. Sample 800°C heat treated;
3. Sample 1500°C heat treated**

4. CONCLUSIONS

The coagulation binding (next to hydraulic binding) is developing for certain pH values, specific to the concrete composition during the hardening process of different

concretes. The optimal pH value for the hardening medium is reached by using a specific electrolyte. For the Ultra Low Aluminous Cement Content and Clay D79 used as aggregate, the optimal pH value is ranging between 3 and 4.

REFERENCES

- [1]. L Prost: Les Refractaires Moulables. L'industrie Ceramiques, (661), 1973, 279.
- [2]. N Angelescu: Heating Behaviour of Monolithics Bound by Coagulation. Turkish Cement and Concrete World, July-August 2003, 8 (3), 52-59
- [3]. Z Li, G Ye: Bonding and Recent Progress of Monolithic Refractories. Intereram, 1992, 41 (3), 169-172.
- [4]. Angelescu, N.: Low Cement Concretes. Doctorate thesis, Polytechnic University Bucharest, 1983, 200 p.
- [5]. Rebouillant L, Rigaud M, Ildefonse J P, Gabis V, Dubreuil P, and Daniellou P, Cement-free Castables with Micronized Andalusite. 9th SIMCER, Bologna, Italy, 5- 8 October, 1998.
- [6]. N Angelescu: Complex Binding Matrix. Special Magazine on Engineering Materials, Jyubliana, 1996, 1, 11-13.
- [7]. I Teoreanu, N Angelescu: Fundamentals in Developing New Generations of Refractory Concretes. Concretes with Simple and Complex Binding Systems. Rumanian Chemical Quarterly Reviews, 1996, 4 (1-2), 123-147.
- [8]. Angelescu N et al, Different Binding Systems Coexistence. The Fifth NCB International Seminar, New Delhi, 21-24 November 1996, III, XIII-112-118.
- [9]. Shataff H, Alshamsi A M, The Effect of Condensed Silica Fume on some Properties of Concrete in Hot Climate. First International Conference on Reinforced Concrete Materials in Hot Climates, Al Ain, United Arab Emirates, April, 1994, 24-27.
- [10]. N. Angelescu, A New Binding System for Concrete. Proceed. of the 6th International Conference of Concrete Technology, Amman, Iordania, October, 2002 1, 213-223.
- [11]. I Teoreanu, N Angelescu: Hardening Mechanisms and Behaviour of Low-Alumina Cement Refractory Concrete Binding Systems. Intereram, 1994, 43, 360.
- [12]. Angelescu N, Dobrea M, Iacob S, Special Low Cement Concretes. Tenth. International Congress on Polymers in Concrete, Honolulu, 23-25 May, 2001.
- [13]. R D Lankard and, H D Lease: Refractory Concretes for Steelplant Applications. Refract. Journal. (1), 1986, 6.
- [14]. J Moreau: Development of low Cement and Ultra low Cement Castable in Combustion Chamber and Boilers of Domestic Waste Incinerators. Intereram, 37 (Refractory Special Issue), 1987, 8.
- [15]. Angelescu, N., Oprea, F.: Monolitice speciale pentru oala de turnare din oțelării, First ed. Targoviste, Macarie, 2002, p.185
- [16]. Malier, Y.: Les betons a hautes performances, du materiau a l'ouvrage. Presses de L'Ecole Nationale des Ponts et Chaussees. Paris, 1990.
- [17]. Angelescu, N. - *Fundamentals of coagulation binding for special concretes*. Proceed of the 7th International Conference of Concrete Technology, October, 2004, Kuala Lumpur, Malaezia, Vol. "Innovations and Emergeting Technology in Concrete Industry", ISBN 976-958-160-8, pp. 323-331, 2004.
- [18]. Ionita, C., Angelescu, N. Abdelgader, H. S., Bratu, V., Stanciu, D., Ion, I. - The influence of hydration on the mechanical strength of the high aluminous cement. Proceedings of The International Conference on Advances in Cement and Concrete in Africa, ACCTA 2013, Johannesburg, South Africa, 2013, pp. 961 – 968.

EFFECT OF Zn CONTENT ON STRUCTURE, ROUGHNESS AND CORROSION BEHAVIOR OF Zn-Ni ALLOYS

Hayette FAID

Faculty of Technology, Department of Environmental Engineering. University Bordj Bou Arreridj, Algeria.

E-mail: mme.faid@gmail.com

Abstract: In this work, Zn-Ni alloys have been deposited on steel from sulfate bath, by electrodeposition method. The effect of Zn content on deposits properties was studied by cyclic voltammetry (CV), chronoamperometry (CA), linear stripping voltammetry (ALSV) and diffraction (XRD) and scanning electronic microscopy (SEM). The corrosion behavior in 3.5 wt. NaCl solution was examined using anodic polarization test and electrochemical impedance spectroscopy. X-ray diffraction of show that Zn-Ni alloys structure is composed of δ phase and γ phase, which increase with the decrease of Zn content in deposits. Results show that deposits obtained from bath less Zn^{2+} concentration exhibited better corrosion resistance.

Keywords: Electrodeposition, Zn-Ni alloy, Stripping voltammetry, Corrosion behavior

1. INTRODUCTION

Electrodeposition of Zn metal alloys with iron group metals, Fe, Ni and Co, has been widely studied owing to their better corrosion performance than pure Zn [1–4]. Among these alloys, Zn-Ni alloy has attracted increasing attention in recent years. Interest in the formation of Zn–Ni alloy coatings by electrochemical methods has been strong for many years due to their high corrosion resistance and excellent mechanical properties compared with pure Zn deposits [4–7]. Electroplated zinc coatings are considered as one of the main methods used for the corrosion protection of steel. Electrochemical deposition is an attractive method for the elaboration of alloys coatings and nanostructures compared with physical methods. The electrodeposition of Zn–Ni alloy from aqueous solutions is classified as an anomalous codeposition, in which the less noble metal zinc deposited preferentially under plating conditions. This anomalous codeposition can be explained by considering zinc hydroxide suppression mechanism; it is generally accepted to be related to the hydrogen evolution at the cathode causing the formation of zinc hydroxide precipitation, which inhibits the deposition of nickel [8]. Zn-Ni alloys were plated from acid and alkaline bath, in various sulfate baths based chloride or baths based on both chloride and sulfate [9-11]. Many reports are available on the influence of deferent parameters deposition on surface properties, phase structure, corrosion resistance properties of Zn-Ni alloys [12-18]. Since the composition pH of plating bath are crucial parameters, affecting the structure and morphology of the coatings, it plays an important role on its corrosion resistance properties as well. In this study, Zn-Ni alloys were deposited from sulphate bath with different content of Zn^{2+} . The electrochemical, surface properties and corrosion resistance of deposits were investigated.

2. EXPERIMENTAL

The Zn–Ni alloys are deposited potentiostatically, from a deposition solution containing Na_2SO_4 (1M), H_3BO_3 (0.4 M), $NiSO_4 \cdot 6H_2O$ (0.2 M) $ZnSO_4 \cdot 7H_2O$ with different

amounts (0.2 M, 0.02 M and 0.005 M). The pH value of the bath was nearly 4. The composition of the baths and electrodeposition conditions are summarized in Table 1.

Table 1: Solution composition for electrodeposition of Zn-Ni deposits

Composition Bath	Na_2SO_4 (M)	H_3BO_3 (M)	$ZnSO_4$ (M)	$NiSO_4$ (M)
1	-	0.4	0.2	0.2
2	1	0.4	0.02	0.2
	1	0.4	0.005	0.2

Electrochemical experiments are carried out in a conventional three-electrode cell using a VoltaLab 40 potentiostat/galvanostat controlled by a PC. A standard three electrodes system consisting of reference electrode which is Saturated Calomel Electrode (SCE) and counter electrode was a Platinum plaque electrode, working electrode was steel. Before the deposition, the substrates are cleaned in nitric acid and then rinsed with distilled water. All the experiments are performed in unstirred solutions. The baths are aerated with nitrogen. Cyclic voltammetry potentiostatic and anodic linear voltammetry techniques are used to study the electrochemical behavior of deposits. The phase structure of deposits was determined by X-ray diffraction (XRD) analysis with $\lambda_{K\alpha}(Cu)$ incident radiation (1.54 Å) using diffractometer « X'PERT PRO MPD » of Philips. For corrosion behavior, the Zn–Ni plated samples were used as working electrode and a solution of 3.5% wt. NaCl was used as the test solution. The samples were immersed in test solution for 1h. The potentiodynamic polarization was carried out at scan rate of $2 \text{ mV} \cdot \text{s}^{-1}$, with a scanning rang from -0,25V to + 0,25V of open circuit potential. The electrochemical impedance spectroscopy (EIS) was carried in the frequency range of 60 kHz to 10 mHz using perturbing voltage of 10mV.

The equivalent circuit simulation program (ZView) was used for data analysis, synthesis of the equivalent circuit and fitting of the experimental data.

3. RESULTS AND DISCUSSION

The cyclic voltammograms recorded in the different Zn^{2+} , Ni^{2+} and (Zn^{2+} and Ni^{2+}) solutions, respectively, at a scan rate of 20 mV/s are shown in figure 1.

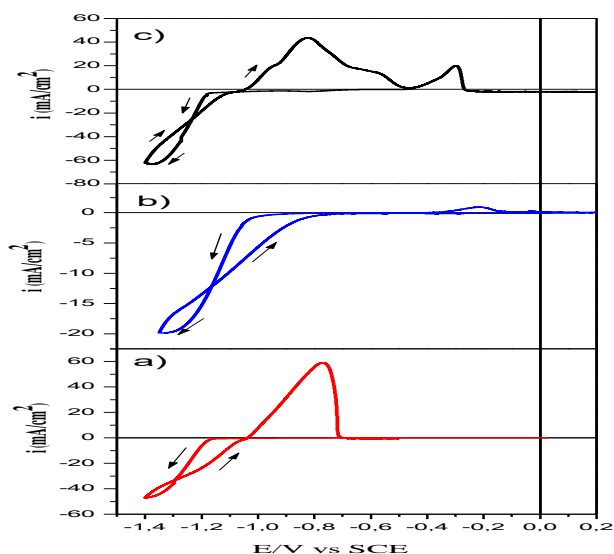


Figure 1. Voltammetric curves for steel substrate in: a) $0.2\text{M ZnSO}_4 \cdot 7\text{H}_2\text{O} + 1\text{M Na}_2\text{SO}_4 + 0.4\text{M H}_3\text{BO}_3$; b) $0.2\text{M NiSO}_4 \cdot 6\text{H}_2\text{O} + 1\text{M Na}_2\text{SO}_4 + 0.4\text{M H}_3\text{BO}_3$; c) $0.2\text{M ZnSO}_4 \cdot 7\text{H}_2\text{O} + 0.2\text{M NiSO}_4 \cdot 6\text{H}_2\text{O} + 1\text{M Na}_2\text{SO}_4 + 0.4\text{M H}_3\text{BO}_3$, $\nu = 20 \text{ mV s}^{-1}$

In the presence of the Zn^{2+} cations (fig.1.a), the reduction begins at potential of -1.2 V . On the return, the anodic peak located at -0.77 V corresponded to the dissolution of deposited Zn. In the presence of Ni^{2+} cations (fig.1.b), the reduction begins at a potential of -0.91 V and an anodic peak at -0.2 V attributed to the dissolution of Ni deposited. In the presence of Zn^{2+} and Ni^{2+} (fig.1.c), the reduction begins at -1.17 V . A cathodic peak due to the deposition of Zn-Ni alloy was observed at -1.23 V . In the reverse scan, from the same figure, two anodic peaks appeared, the first dissolution anodic peak (at -0.97 V) corresponds to the dissolution of Zn from the alloy, which shifts to more negative value comparing with that for bath containing only zinc. The second peak has appeared at about -0.64 V and is related to the dissolution of deposited previously. The first anodic peak (in -0.97 V/SHE) is associated with zinc deposition of the phase $\delta\text{-}(\text{Ni}_3\text{Zn}_{22})$. The second peak appears at -0.67 V/SHE and is related to zinc dissolution in the phase $\gamma\text{-}(\text{Ni}_5\text{Zn}_{21})$ [19]. The anodic scanning reveals anodic peak at -0.35 V is due to the dissolution of nickel, while the peaks at more negative potentials correspond to the dissolution of the zinc present in different phases of the zinc-nickel alloy [20].

It is important to note that the height of the anodic peak of the deposited Zn dissolution was higher than that observed in the case of dissolution of the Zn-Ni alloy. This indicates that the amount of zinc in the alloy is less than that of a pure metal. The curve appears between those of Zn and Ni; from where the potential deposition is closer to that of Zn than of Ni. This result indicates the formation of Zn-Ni alloy.

The dissolution curves of Zn-Ni deposits (Fig.3.b) have two anodic peaks at -0.94 and -0.3 V , respectively. The curve obtained for (bath 1), shows three anodic peaks, a peak A1 located at -0.91 V , in the region of dissolution of pure zinc (fig.3.a) with a lower intensity than that of zinc and a displacement towards less negative potentials. This peak A1 was attributed to the dissolution of zinc from its phases, and the peak C is attributed to the dissolution of nickel from its phases [10].

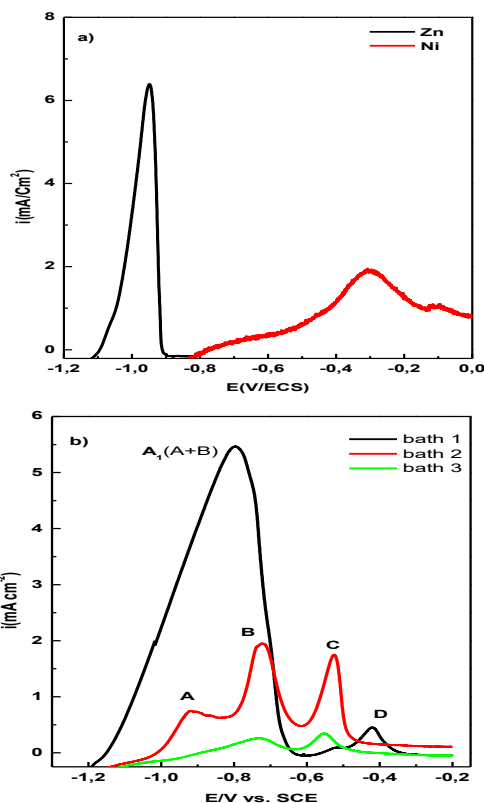


Figure 2. Potentiodynamic stripping response ($\nu = 5 \text{ mVs}^{-1}$) of Zn-Ni alloys deposited in sulfate bath at -1.25 V a) Zn, Ni b) with various $[\text{Zn}]/[\text{Ni}]$ ratio.

By decreasing the zinc concentration to 0.02 mol.l^{-1} (bath 2), the peak A1 appears as a double peak (peak A and peak B), which can be explained by the presence of a new phase. The third anode peak (C) corresponds to the anodic dissolution characterizing the dissolution of nickel from its phases. In the presence of $0.005 \text{ mol.l}^{-1} \text{ Zn}^{2+}$ (bath 3), only two peaks are present, peak A disappears while peaks B and C appear in the region of dissolution of Ni (fig.2.a) with a decrease in height. This indicates an increase in the Ni content in the deposit.

The results of the AFM analysis (Fig.3), show that the surface of the deposit obtained from the bath 3 is more compact, with minimal roughness ($\text{RMS} = 70.671 \text{ nm}$) surface roughness, decreases with decrease of Zn^{2+} content in the bath. So that of the sample obtained from bath 1 was much higher than those of the other samples, showing arithmetic average roughness (Ra) and root-mean-square roughness (Rms) of 112.7 nm and 86.46 nm , respectively. Consequently, the Zn-Ni obtained from bath has the low roughness, so a less surface area in contact with a corrosive environment.

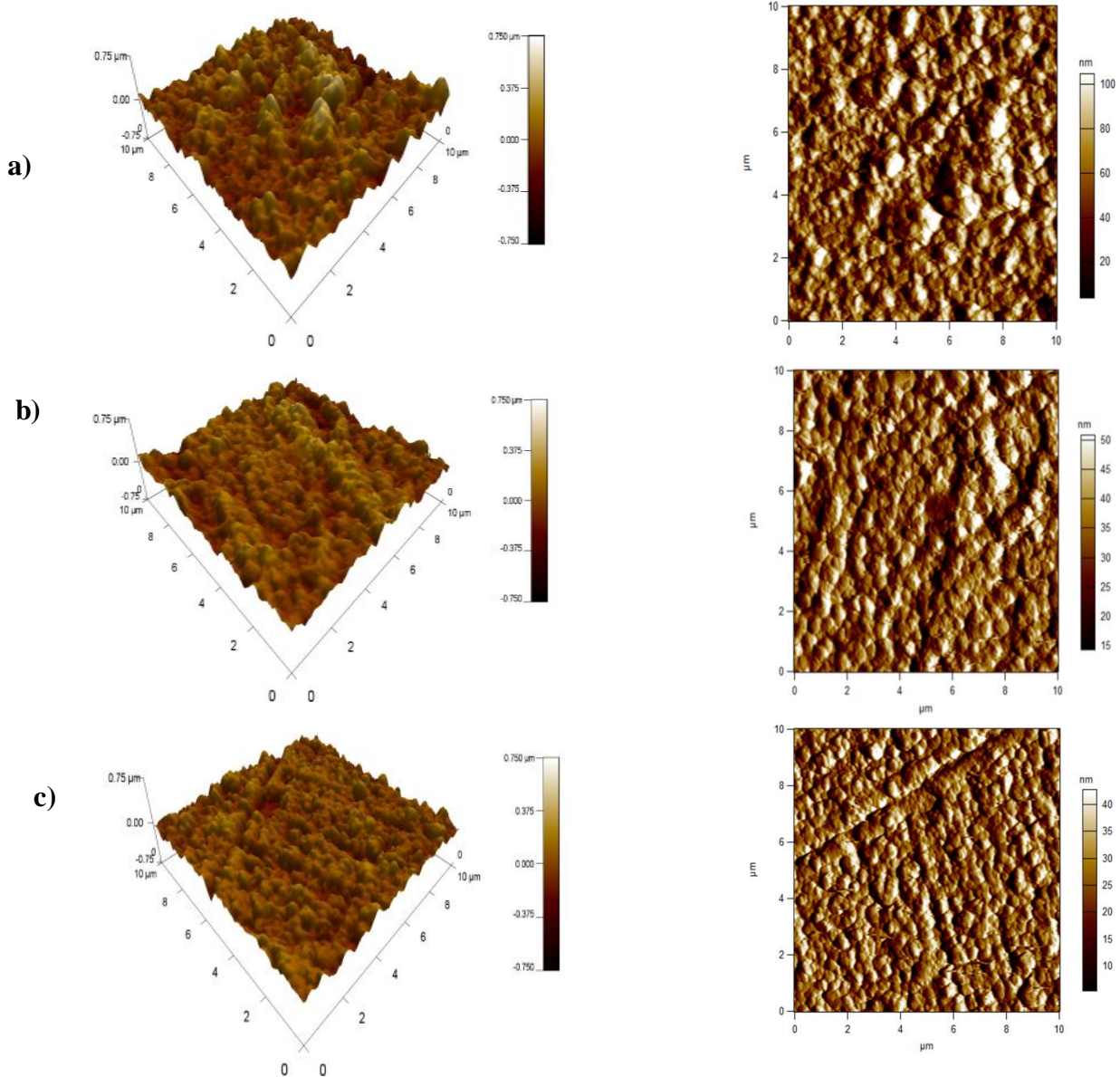


Figure 3. AFM Analysis of Zn–Ni deposits obtained from: a) bath 1, b) bath2, c) bath 3

XRD analysis for Zn-Ni obtained from different bath (Fig.4), indicate the presence of two phases corresponding to the γ ($\text{Ni}_5\text{Zn}_{21}$) and δ ($\text{Ni}_3\text{Zn}_{22}$) phases. The height of each peak considered an indication of the phase content in the deposit. The decrease in the zinc concentration leads to an increase in the γ phase and a decrease in the δ phase. A similar study has shown that the γ -single-phase centered cubic structure can be obtained with a Ni content in these layers and in the range of 13.23% to 19.11% by weight, increasing the ratio $[\text{Ni}^{2+}] / ([\text{Zn}^{2+}] + [\text{Ni}^{2+}])$ and the current density [21].

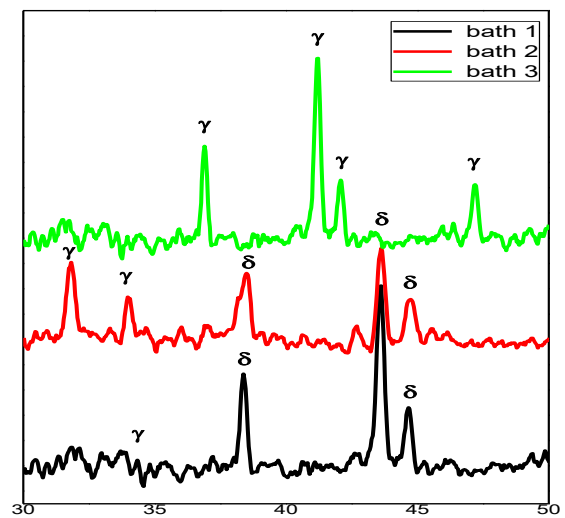


Figure 4. XRD patterns of Zn-Ni deposits with various [Zn]/[Ni] ratio

The surface morphology of coatings after immersion and EDS spectra identifying the corrosion products are presented in Fig.5. Corrosion product formed hexagonal crystals in the surface. The EDS spectra obtained on corrosion product suggested the presence of zinc, oxygen with chlorine, the formation of zinc rich corrosion products in sodium chloride. The dominant corrosion products on zinc under sodium chloride influence are simonkolleite zinc hydroxy chloride $Zn_5(OH)_8Cl_2$ (ZHC) [22, 23] forms as corrosion product as clearly evident from EDS spectra with Cl peak. $Zn_5(OH)_8Cl_2$ is more compact than other forms of Zn corrosion products.

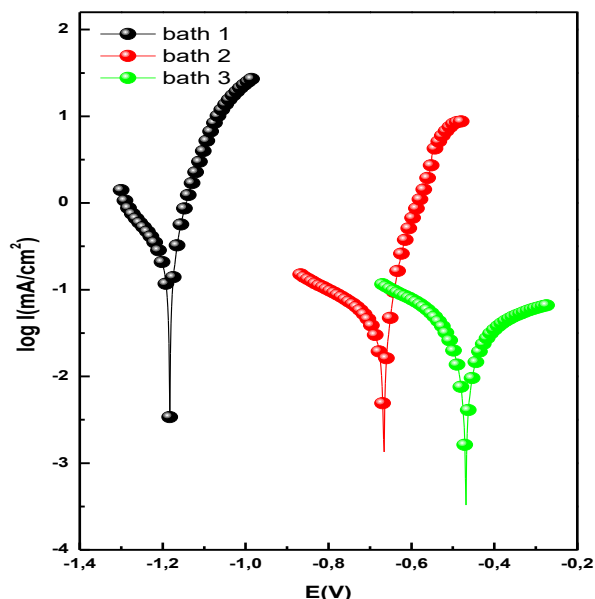


Figure 6. Polarization curves of Zn-Ni deposits obtained from: a) bath 1, b) bath2, c) bath 3.

The potentiodynamic polarization tests were carried out on Zn-Ni deposits obtained from the three baths with different Zn^{2+} concentration (0.2 M, 0.02 M and 0.005 M). The polarization curves were recorded with a scanning speed of $2 \text{ mV}\cdot\text{s}^{-1}$. The Tafel curves obtained from the potentiodynamic polarization tests for the Zn-Ni deposits are shown in the Figure 6.



Figure.5 (b)

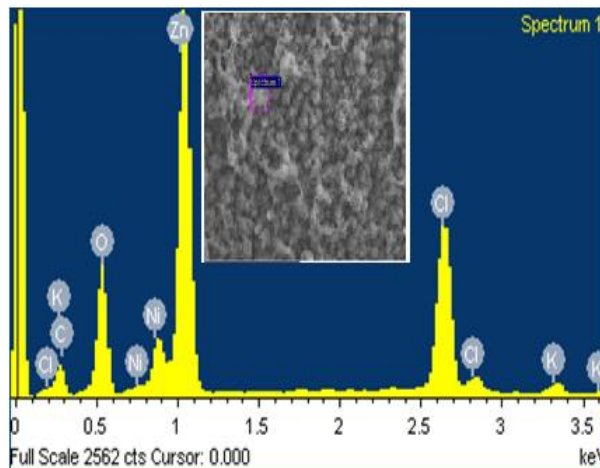


Figure.5 (a,b). SEM micrographs and EIS spectra obtained for Zn-Ni deposits after immersion in 3.5 wt.% NaCl solution.

Electrochemical parameter values; the corrosion potential E_{corr} , the corrosion current density i_{corr} , the polarization resistance obtained by the extrapolation method of Tafel lines are summarized in Table 2.

Table 2: The electrochemical parameters E_{corr} , i_{corr} , R_p of Zn-Ni deposits in 3.5 wt.% NaCl solution

Deposits	E_{corr} (mV)	i_{corr} (mA.cm ⁻²)	R_p (ohm.cm ²)
1	-1182.8	0.294.4	73.67
2	-666.7	0.046	296.0
3	-469.0	0.039	759.1

Results show that corrosion rate decreases and polarization resistance increases with the decrease of zinc concentration. The corrosion mechanism in NaCl medium can be interpreted on the basis that the corrosion of Zn-Ni alloys consists of a preferential dissolution of Zn and the surface becomes rich in Ni [7]. Electrochemical impedance spectroscopy measurements were performed for deposits prepared from baths (1, 2 and 3), to evaluate corrosion resistance of Zn-Ni deposits in 3.5 wt.% NaCl solution. Figure 7 illustrates Nyquist (Figure 7(a)) and Bode diagrams (Figure 7(b)) of deposits after immersion for 1 h in NaCl solution. The curves show a single semicircle, the diameter of this one corresponds to a charge-transfer resistance (R_{ct}). The charge transfer resistance and the double layer capacitance values were extracted from Nyquist plots and presented in table 2. The results indicate that the deposits obtained from bath with less Zn^{2+} content have the highest corrosion resistance. Furthermore, these results are consistent with results of polarization studies (Fig.6). The Bode diagrams (Fig.7.b) show a single maximum of the phase angle for the three deposits, which indicates a onetime constant, so one capacitive loop assigned to the charge transfer process. The phase angle for the deposit 1 lies in the medium frequency domain ($\sim f = 10^1 - f = 100$), for deposit 2 in the medium frequency domain ($\sim f = 10^2 - f = 100$) and for deposit 3, the phase angle is wide limited

by the mean frequencies and the low frequencies ($\sim f = 10^2 - f = 10^{-1}$). The largest module value in the low frequency domain indicating, the enhanced corrosion resistance (Fig.7.c). In addition, the maximum value of the phase angle for deposit 3 is greater than that of the other deposits, which means a high corrosion resistance.

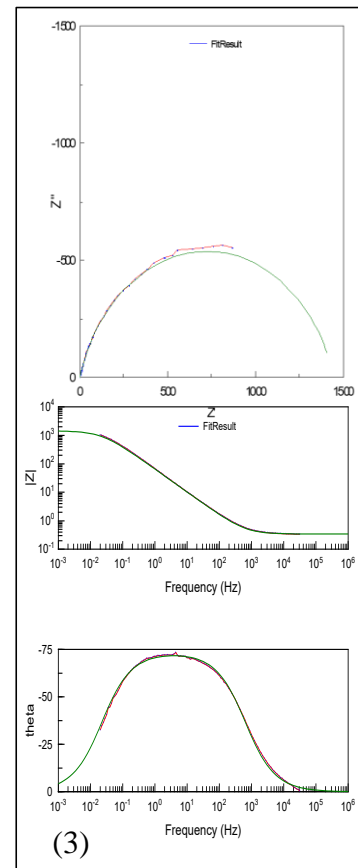
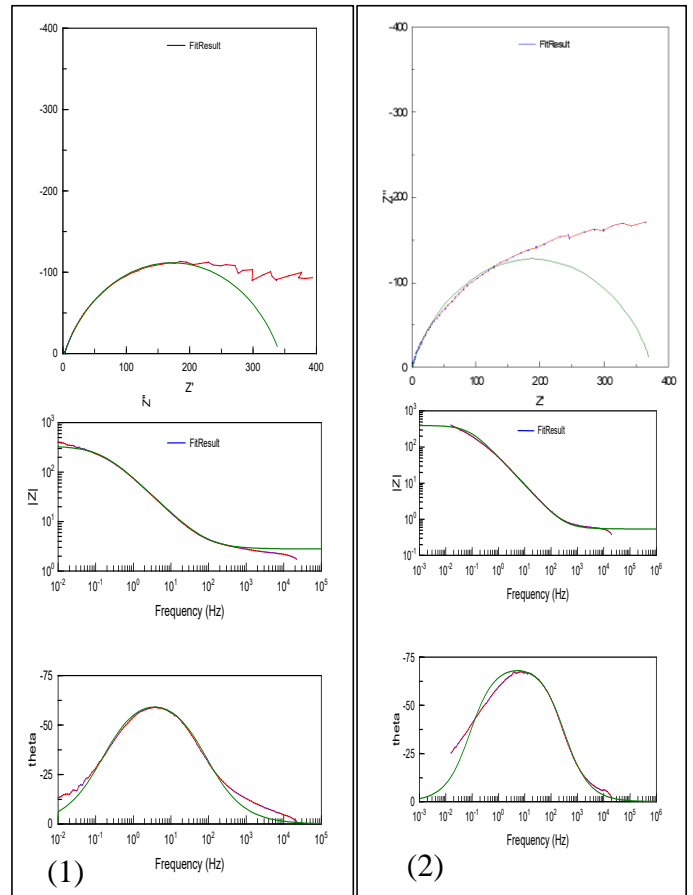
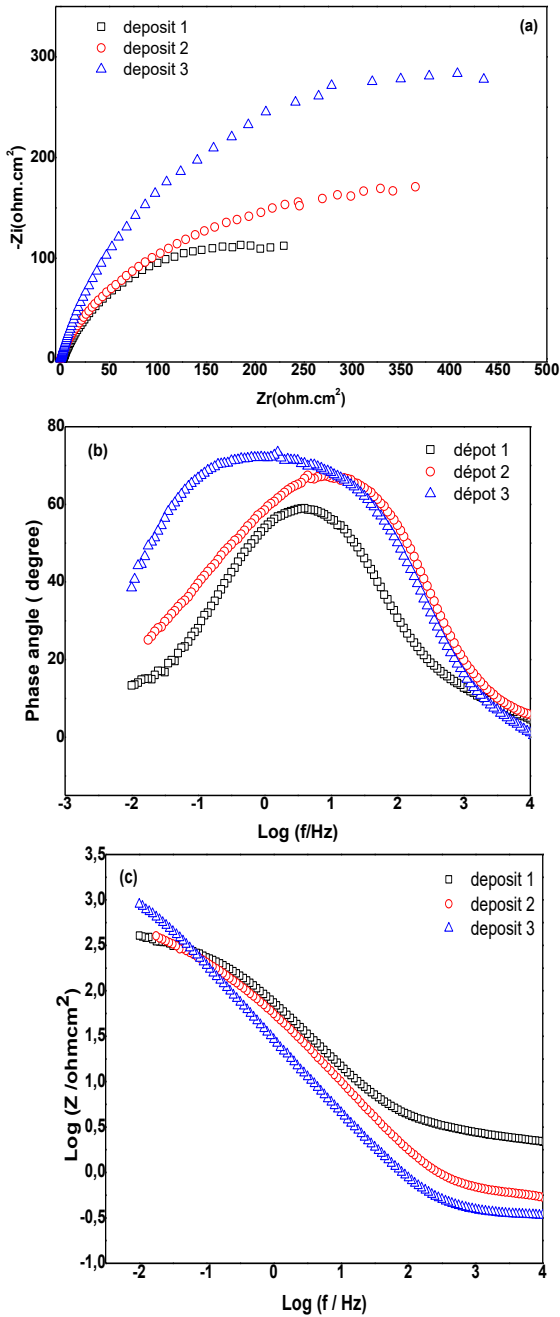


Figure 7. Impedance diagrams obtained for Zn-Ni deposits in 3.5 wt.% NaCl solution. a) Nyquist plots, b,c) Bode plots, d) Fit result

The equivalent electrical circuit (CEE) proposed to characterize the metal / electrolyte interface and allowing the modeling of the impedance spectra is shown in Table .The circuit is composed of R_s is the resistance of the electrolyte, R_{ct} charge transfer resistance and CPE constant phase element. The equivalent electrical circuit, calculated elements determined for the EIS data by Zview software and the all fit results are shown in Table 3.

Table 3: Electrical equivalent circuit and calculated circuit element values using Zview software for EIS spectra

Deposit	1	2	3
R_s (Ωcm^2)	3.4	0.51	0.34
CPE-T	3.1×10^{-3}	3.8×10^{-3}	3.21×10^{-3}
CPE-P	0.74	0.78	0.82
R_{ct} (Ωcm^2)	340	397	1518



4. CONCLUSION

The electrodeposition of Zn-Ni alloy from sulphate bath with deferent Zn^{2+} concentration was studied. The stripping voltammetry, XRD and EDX analysis indicated that phase composition and structure of the Zn-Ni alloys are significantly dependent on the bath composition. Moreover, polarization test and electrochemical impedance spectroscopy measurements reveal that Zn-Ni alloy films electrodeposited from bath with less Zn^{2+} content (0.005M) exhibit enhanced corrosion resistance in 3.5 wt% NaCl aqueous solutions.

REFERENCES

[1] R. Ramanauskas, P. Quintana, L. Maldonado, R. Pomés, M.A. Pech-Canul, Corrosion resistance and microstructure of electrodeposited Zn and Zn alloy coatings, Surf. Coat. Technol. 92 (1997) 16–21
 [2] A.M. Alfantazi, J. Page, U. Erb, J. Appl. Electrochem. 26 (1996) 1225.
 [3] Gharahcheshmeh. MH, Sohi MH (2009) Study of the corrosion behavior of zinc and Zn–Co alloy electrodeposits obtained from alkaline bath using direct current. Mater Chem Phys 117:414-421.
 [4] C. Müller, M. Sarret, M. Benballa, Some peculiarities in the codeposition of zinc–nickel alloys, Electrochim. Acta 46 (2001) 2811–2817.
 [5] M.J. Rahman, S.R. Sen, M. Moniruzzaman, K.M. Shorowordi, Morphology and properties of electrodeposited Zn–Ni alloy coatings on mild steel, J. Mech. Eng.40 (2009) 9–14.
 [6] Pushpavanam M, Natarajan SR, Balakrishnan K, et al. Corrosion behavior of electrodeposited zinc-nickel alloys. J Appl Electrochem. 1991;21:642–645.
 [7] S.H. Mosavat, M.H. Shariat, M.E. Bahrololoom. Study of corrosion performance of Electrodeposited nano crystalline Zn–Ni alloy coatings, Corros. Sci. 59 (2012) 81–87.

[8] Brenner A (1963) Electrodeposition of Alloys, Academic Press, New York.
 [9] Miranda FF, Barcia OE, Diaz SL, Mattos OR, Wiart R (1996) Electrodeposition of Zn–Ni alloys in sulfate electrolytes. Electrochim Acta 41:1041-1049.
 [10] Petrauskas A, Grincevičienė L, Češuniene A, Juskenas R (2005) Studies of phase composition of Zn–Ni alloy obtained in acetate-chloride electrolyte by using XRD and potentiodynamic stripping. Electrochim Acta 50:1189-1196.2004
 [11] Ivanov I, Kirilova I (2003) Corrosion resistance of compositionally modulated multilayered Zn–Ni alloys deposited from a single bath. J Appl Electrochem 33:239-244.
 [12] T.V. Byk, T.V. Gaevskaya, L.S. Tsybul'skaya, Effect of electrodeposition conditions on the composition, microstructure, and corrosion resistance of Zn–Ni alloy coatings, Surf. Coat. Technol. 202 (2008) 5817–5823.
 [13] Hammami O, Dhouibi L, Triki E (2009) Influence of Zn–Ni alloy electrodeposition techniques on the coating corrosion behaviour in chloride solution. Surf Coat Technol 203:2863-2870.
 [14] X. Qiao, H. Li, W. Zhao, D. Li, Effects of deposition temperature on electrodeposition of zinc–nickel alloy coatings, Electrochim. Acta 89 (2013) 771–777
 [15] S. Fashu, C.D. Gu, X.L. Wang, J.P. Tu, Influence of electrodeposition conditions on the microstructure and corrosion resistance of Zn–Ni alloy coatings from a deep eutectic solvent, Surf. Coat. Technol. 242 (2014) 34–41.
 [16] H. Faid, L. Mentar, M. R. Khelladi and A. Azizi, Deposition potential effect on surface properties of Zn–Ni coatings, Surf. Eng., 2017, 33(7), 529–535.
 [17] Z. Feng, M. An, L. Ren, J. Zhang, P. Yang and Z. Chen, Corrosion mechanism of nanocrystalline Zn–Ni alloys obtained from a new DMH-based bath as a replacement for Zn and Cd coatings, RSC Adv., 2016, 6(69), 64726–64740.
 [18] Chang LM, Chen D, Liu JH, Zhang RJ (2009) Effects of different plating modes on microstructure and corrosion resistance of Zn–Ni alloy coatings. J. Alloys. Compd 479:489-493.2008.
 [19] Abou-Krishna, M.M., Assaf, F.H., and Toghan, A.A., J. Solid State Electrochem., 2007, vol. 11, p. 244.
 [20] F. Elkhatabi, M. Sarret, C. Müller, J. Electroanal. Chem. 404 (1996) 45.
 [21] Z. Feng, Q. Li, J. Zhang, P. Yang, H. Song, M. An, Surf. Coat. Technol. 270 (2015) 47.
 [22] Q. Qu, L. Li, W. Bai, C. Yan, C.N. Cao, Corros. Sci. 47 (2005) 2832–2840.
 [23] J.B. Bajat, V.B.M. Stankovic, M.D. Masimovic, D.M. Drazic, S. Zee, Electrochim. Acta 47 (2002) 4101–4112.

SYNTHESIS OF CERAMIC BIOMATERIALS BASED ON CALCIUM AND PHOSPHORUS FROM AQUEOUS SOLUTIONS

Dan Nicolae UNGUREANU ¹, Nicolae ANGELESCU ¹, Adrian CATANGIU ¹, Daniela AVRAM ²,
 Florina Violeta ANGHELINA ¹, Ileana Nicoleta POPESCU ¹

¹Faculty of Materials Engineering and Mechanics, Valahia University of Targoviste,
 13 Aleea Sinaia Street, Targoviste, Romania

²Valahia University of Targoviste, Faculty of Environmental Engineering and Food Science,
 13 Aleea Sinaia Street, Targoviste, Romania

E-mail: avramdana75@yahoo.com

Abstract: *This paper presents the most used processes for the synthesis of hydroxyapatite from aqueous solutions: chemical precipitation, the hydrothermal process and the sol-gel method. The experimental part includes the synthesis of hydroxyapatite by chemical precipitation. The obtained results confirm the obtaining of a ceramic with a high purity and a high degree of crystallization.*

Keywords: *hydroxyapatite, synthesis methods, chemical precipitation, XRD, SEM*

1. INTRODUCTION

Hydroxyapatite is one of the most studied ceramic materials with medical applications in the field of reconstruction and regeneration of bone structures, for which the researchers have shown a special interest since the 1970s. The variety of technological routes through which this material can be synthesized, such as: processing of hard tissues from mammal or coral structure and laboratory synthesis (chemical co-precipitation methods, solid state synthesis reactions, hydrothermal methods, sol-gel processes, microwave synthesis etc) [1-4]. This material can be used in various forms as a sintered powder, in a compact or porous shape, for coating applications, as a bioactive material on bioinert support, as a filler for bone grafts, or as a composite e.g. hydroxyapatite – polyethylene etc. Thus, this bioceramic is a material with a wide range of applicability in the field of medicine [5].

Wet synthesis methods involve the use of aqueous solutions. These methods lead to the production of hydroxyapatites characterized by a large specific surface area and small particle size. In most cases deviations from stoichiometry occur and, at the same time, amorphous structures are obtained. All this depends on a number of factors, such as: chemical reagents, concentration and initial pH of the solutions used in the synthesis process, synthesis temperature, stirring speed etc [6].

Chemical precipitation presents certain advantage by comparison with the other hydroxyapatite synthesis technology: the use of aqueous solutions; the probability of their contamination during the synthesis process is

very low; the method imposes a relatively low cost of production [6-7].

The synthesis of hydroxyapatite by hydrothermal methods confers the advantage to obtain products where crystallites size that can exceed 600 nm, under the conditions of synthesis and heat treatment temperatures between 200 and 950°C and pressures from 100 to 200 MPa [8, 9].

The sol-gel method allows the use of very small colloidal particles (on the order of nanometers or even smaller) as precursors for hydroxyapatite synthesis, thus ensuring a high degree of homogeneity and purity of the final product. Basically, the process involves the synthesis in aqueous solutions of ceramic particles by mixing some metal alkoxide precursors, followed by hydrolysis, gelation, aging of the gel and heat treatment, in order to obtain crystalline hydroxyapatite [10].

1.2 Methods for the synthesis of hydroxyapatite

1.2.1 Chemical precipitation

Many methods for hydroxyapatite synthesis by chemical precipitation are presented in the literature. The most popular methods use calcium hydroxide, calcium nitrate and, respectively, phosphoric acid, diammonium hydrogen phosphate as starting reagents.

Thus, Abidi and Murtaza [11] synthesize hydroxyapatite in which the calcium ions come from the calcium hydroxide obtained from the reaction between calcium oxide and water, in the following conditions: temperature: 20°C, stirring: 1000 rpm, time: one day. The corresponding amounts of Ca(OH)₂ and H₃PO₄ were

added to obtain the compound based on calcium and phosphorus. The acid was added to the alkaline solution at a rate of 1.5 ml / min. The precipitate was aged by stirring of the bath, for 24 hours at 20°C. Also, pH was corrected with ammonia water NH₄OH. The obtained material was dried at 100°C and heat treated at different temperatures between 100 and 800°C. The hydroxyapatite crystallinity crystallite size was dependent by thermal treatment temperature.

Vasquez et al.[12] present a method for hydroxyapatite synthesis in which Ca(NO₃)₂· 4H₂O and (NH₄)₂HPO₄ it uses as a source of calcium and phosphorus. The authors use two solutions based on Ca²⁺ and PO₄³⁻ ions in concentrations of 1M and, respectively, 0.6 M. The reaction takes place at 95°C, the addition speed of (NH₄)₂HPO₄ solution was 22mL / min. The precipitate was aged for 2 weeks at room temperature. The dry precipitate was heat treated at 850°C.

The XRD analysis highlights a well crystallized hydroxyapatite, after heat treatment, in which the presence of β-tricalcium phosphate (Ca₃(PO₄)₂) is found. The Ca / P molar ratio was less than 1.67. The morphological analysis shows particles with similar morphology, the particle size was 500 nm.

1.2.2 Hydrothermal method

In order to obtain a stoichiometric hydroxyapatite, Earl et al. [13] prepares two solutions based on Ca(NO₃)₂·4H₂O and (NH₄)₂HPO₄. The authors obtain a mixture with a pH of 5.1 which is transferred to a container in which the hydrothermal reaction takes place (200°C for a period between 24 and 72 hours). The precipitates were washed with distilled water, and in some cases with ethanol to prevent particle agglomeration. In the end, pH of precipitates was equal to 7. The samples were dried in the oven for 4 hours at 50°C.

X-ray diffraction analysis shows the formation of hydroxyapatite in all the samples obtained. In the cases where the reaction lasted 48 and 72 hours, the formation of secondary phase monetite CaHPO₄ was found.

The morphological analysis shows the formation of rod-like particles with the diameter between 10 and 60nm and the length between 100 and 600nm, suitable to be used for alleviation of hypersensitivity by infiltration into the dentinal tubules.

In another work [2] hydroxyapatite is synthesized by the hydrothermal process by using Ca(NO₃)₂ and disodium hydrogen phosphate (Na₂HPO₄) in the presence of ammonia water NH₄OH.

In order to change the morphology of the particles, in the bath, sodium tripolyphosphate (Na₅P₃O₁₀) was added. In the first stage of the synthesis process the bath was set at temperatures in the range of 40-60°C with the pH between 8 and 10. The precipitate obtained was transferred to a container in which the conditions were: temperature: 160°C, pressure: 2MPa, time: 4-12 hours. The precipitate was finally washed with distilled water and ethanol and dried for 24 hours at 50°C.

In all cases, the formation of hydroxyapatite was confirmed by X-ray diffraction analysis and FTIR analysis. The addition of Na₅P₃O₁₀ led to the modification of the hydroxyapatite crystallite size. Their diameter increases with the addition of sodium tripolyphosphate.

1.2.3 Sol-gel synthesis

Beganskiene et al. [14] obtain hydroxyapatite by the sol-gel method by using as calcium and phosphorous precursors calcium nitrate tetrahydrate, trimethyl phosphate ((CH₃O)₃PO) and diethyl phosphite ((C₂H₅O)₂POH). One of the two phosphorus-based reagents is added to the alkaline calcium ion solution. After gel formation, it was matured for different periods of time (2 to 72 hours) at room temperature. The products were heated to 60°C for 24 hours, after which the dried gels were heat treated in two steps. First stage 6 hours at 250°C, and the second, 3 hours at temperatures between 400 and 1000°C.

The obtaining of hydroxyapatite was confirmed by X-ray diffraction. Calcium hydroxide Ca(OH)₂ and calcium oxide CaO were highlighted as secondary phases, in case of samples aged at different periods of time and heat treated at 1000°C. The results were also confirmed by FTIR chemical analysis. The use of dimethyl phosphite was performed in order to improve the sol gel process by eliminating the aging period.

In the paper mentioned above, Vasquez et al. [12] synthesizes a hydroxyapatite with a high degree of purity and by the sol-gel process. The chemical reagents used were calcium nitrate tetrahydrate Ca(NO₃)₂·4H₂O, triethyl phosphate (C₂H₅O)₃P(O), and as a solvent 2-methoxyethanol ether CH₃O(CH₂)₂OH. In order to obtain a sol, the three reagents are added to an Erlenmeyer flask, under stirring. The aging process was carried out at 80°C for 4 days with stirring. The gelation process was performed at temperatures of 90-100°C. The obtained product was heat treated at different temperatures.

The XRD analysis shows the formation of hydroxyapatite in all cases. After heat treatment of samples at 200, 600 and 800°C, the appearance of secondary phases (tricalcium phosphate, calcium oxide and calcite) have been observed.

From the scanning electron microscopy analysis, hydroxyapatite formations can be observed, with a uniform morphology and significantly smaller dimensions (300 nm) by comparison with the other synthesis processes.

2. EXPERIMENTAL PROCEDURE

In this paper hydroxyapatite has been synthesized by the chemical precipitation method [5-7]. The chemical reagents used were calcium hydroxide and phosphoric acid. In order to obtain a hydroxyapatite characterized by a high degree of purity, with good crystallinity and degree of crystallization, high-purity chemical reagents

have been used. Initially, a suspension of 2M Ca(OH)₂ (Acros Organics) and a solution 1.2 M H₃PO₄ (Fisher Scientific) in deionized water were prepared. For pH correction NH₄OH was used. The acid solution was added drop wise (1ml / min) over the alkaline bath, under conditions of intense stirring (1000 rpm). In order to avoid the formation of secondary phases such as tricalcium phosphate and calcium oxide, the pH of the bath was measured at values greater than 10. The precipitate was aging for 48 hours at room temperature. The precipitate obtained was washed with deionized water several times, after which it was dried in an oven at 100⁰C for 24 hours. Finally, the material obtained was ground and heat treated 1200⁰C, in order to obtain a hydroxyapatite with the desired characteristics.

3. CHARACTERIZATION

The samples obtained were analyzed in terms of structure and morphology by X-ray diffraction (Rigaku SmartLab) and scanning electron microscopy (FE-SEM - Carl Zeiss). In the case of XRD analysis, the characteristics of the equipment were: U = 200 mA, V = 45 kV, Cu-Kα = 1.541874 Å. The characteristics of the

SEM equipment: resolution: 1 nm at 15 kV; 1.9 nm at 1 kV; magnification: 12x ... 1.000.000x;

4. RESULTS AND DISCUSSION

4.1 XRD analysis

X-ray diffraction analysis revealed the formation of hydroxyapatite in the structure of the obtained material. Other secondary crystalline phases have not been identified. The most important hydroxyapatite specific peaks were: 25.78 2θ, 28.08 2θ, 28.88 2θ, 31.75 2θ, 32.12 2θ, 32.88 2θ, 34.01 2θ, 39.72 2θ, 46.67 2θ, 48.05 2θ, 49.51 2θ, 50.53 2θ, 51.33 2θ, 52.09 2θ, 53.18 2θ. An analysis was made regarding the degree of crystallization and the crystallite size, in the case of heat treated hydroxyapatite powder. The degree of crystallization was estimated at 96% and the average crystallite size at 40 nm. The estimations were made according to the methods described in other works [15, 16] and the ICCD-PDF 2 database, file: 00-009-0432.

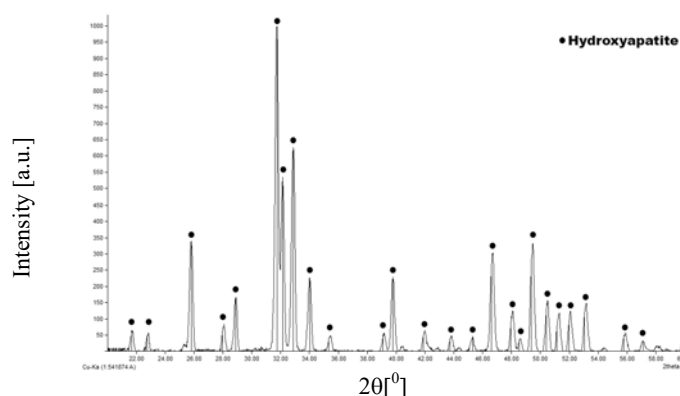


Figure 1. XRD analysis for heat treated ceramic powder

4.2 SEM analysis

As expected, the morphological analysis reveals a typical surface for a structure with a high degree of crystallinity. It can be seen from the SEM micrograph, presented in figure 1, hydroxyapatite formations with average size of 1 μm. Also, one can observe the high degree of packing of the particles, associated in a

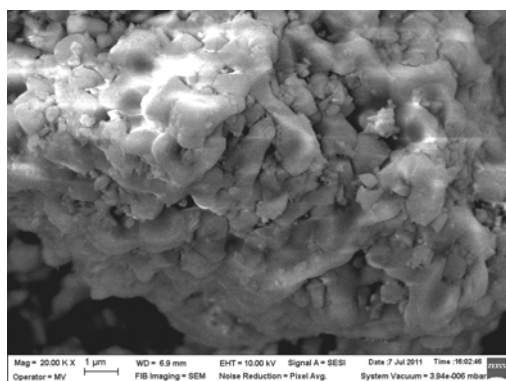


Figure 2. SEM analysis for heat treated ceramic powder

cluster, effect of the applied heat treatment. All these have been confirmed by X-ray diffraction analysis. The stability of the hydroxyapatite implants depends very much on the high crystallinity of this material, practically a heat treatment carried out at a high temperature (1200⁰C) prevents the appearance of the degradation phenomenon upon contact with the body fluids.

At the same time, the stability of this compound based on calcium and phosphorus also depends on its purity. With the heat treatment at high temperature, crystalline formations such as calcium oxide, tricalcium phosphate - β may appear in the structure of the material.

All this related to the synthesis process (setting of inadequate process parameters) and / or the heat treatment performed in the absence of a protective atmosphere.

5. CONCLUSIONS

In this paper the synthesis of a bioceramic compound based on calcium and phosphorus has been presented.

Synthesis of hydroxyapatite used as a substitute in bone structures depends on the optimal selection of process parameters. In this sense, the paper is based on a series of previous studies written by the authors but also from the literature, regarding the most applied methods for hydroxyapatite synthesis in aqueous solutions.

The experimental procedure confirms the synthesis of hydroxyapatite. X-ray diffraction analysis reveals a product with a high crystallinity, under the conditions of heat treatment at high temperature (1200°C).

Also, no other crystalline formations were identified, which would affect the stability of hydroxyapatite when used as an implant material.

6. ACKNOWLEDGMENTS

The authors gratefully acknowledge Ms. Claudia Gavrilesco - Product Manager from AMS 2000 – Rigaku representative Analytical Division, Mr. Mihai Dănilă from IMT-Bucharest and Mr. Virgil Marinescu from ICPE-CA Bucharest for their support.

REFERENCES

- [1] Correia R. N., Magalahaes M. C. F., Marques P. A. A. P., Senos A.M.R., Wet synthesis and characterization of modified hydroxyapatite powders, *Journal of Materials Science: Materials in Medicine*, 7 (8), 1996, p. 501.
- [2] Zhang H. , Zhou K. , Li Z., Huang S Plate-like hydroxyapatite nanoparticles synthesized by the hydrothermal method, *Journal of Physics and Chemistry of Solids*, 70, 2009, p. 243–248.
- [3] Liu D. M., Yang Q. Z., Troczynski T., Water-based solgel synthesis of hydroxyapatite: process development, *Biomaterials*, 23, 2002 p.691.
- [4] Wang K.W., Zhu Y., Chen F., Cheng G.F., Huan Y.H Microwave-assisted synthesis of hydroxyapatite hollow microspheres in aqueous solution, *Materials Letters*, 65, 15–16, 2011, p.2361-2363
- [5] Angelescu N., Ungureanu D. N., Catangiu A., Synthesis of Crystalline Hydroxyapatite Prepared from Aqueous Solutions, *Chemistry Magazine*, 62(7), 2011, p. 702 – 706.
- [6] Ungureanu D.N., Angelescu N., Tsakiris V., Marinescu V., Investigations Regarding Chemical Synthesis of Calcium Hydroxyapatite, *Romanian Journal of Materials*, 42(1) 2012, p. 52-60.
- [7] Angelescu N., Ungureanu D.N., Anghelina F.V., synthesis and Characterization Of Hydroxyapatite Obtained In Different Experimental Conditions, *The Scientific Bulletin of Valahia University - Materials and Mechanics*, 6(9), 2011, p. 15 – 18.
- [8] Kuśnieruk S. et al., Influence of hydrothermal synthesis parameters on the properties of hydroxyapatite nanoparticles, *Beilstein J Nanotechnol.*, 7, 2016, 1586–1601.
- [9] Skinner H., Studies in the basic mineralizing system CaO-P2O5-H2O, *Calcified Tissue Research*, 14, 1974, p. 3–14.
- [10] Okada M., Matsumoto T., Synthesis and modification of apatite nanoparticles for use in dental and medical applications, *Japanese Dental Science Review*, 51, 2015, p. 85-95.
- [11] Abidi S.S.A., Murtaza Q., Synthesis and Characterization of Nano-hydroxyapatite Powder Using Wet Chemical Precipitation Reaction, *J. Mater. Sci. Technol.*, 30(4), 2014, p. 307-310.
- [12] Vazquez C.G., Barba C.P., Munguia N., Stoichiometric hydroxyapatite obtained by precipitation and sol gel processes, *Revista Mexicana De Fisica*, 51, 3, p.284–293, 2005.
- [13] Earl J.S., Wood D.J., Milne S.J., Hydrothermal synthesis of hydroxyapatite, *Journal of Physics: Conference Series* 26, 2006, p. 268–271.
- [14] Beganskienė A., Dudko O., Sirutkaitis R., Giraitis R., Water Based Sol-Gel Synthesis of Hydroxyapatite, *Materials Science (Medžiagotyra)*, 9, 4., 2003.
- [15] Sanosh, K. P., Chu, M.C., Balakrishnan, A., Kim, T.N., Cho, S.J., Preparation and characterization of nano-hydroxyapatite powder using sol-gel technique, *Bull. Mater. Sci.*, 32, 5, 2009, p. 465
- [16] Landi, E., Tampieri, A., Celotti, G., Sprio, S., Densification Behavior and Mechanisms of Synthetic Hydroxyapatites, *J. Eur. Ceram.Soc.*, 20, 14, 2000, p. 2377.

SYNTHESIS AND CHARACTERIZATION OF DEPOSITED NiO THIN FILMS BY SPRAY PYROLYSIS TECHNIQUE

Chouaieb ZAOUCHE ¹, Yacine AOUN ², Said BENRAMACHE ^{1,*}, Abdelouahab GAHTAR ³

¹ Material Sciences Department, Faculty of Science, University of Biskra, Biskra 07000, Algeria, ² Mechanical department, Faculty of Technology, University of El-Oued, El-Oued 39000, Algeria

³ Biological department, Faculty of Technology, University of El-Oued, El-Oued 39000, Algeria

Email:* s.benramache@univ-biskra.dz, benramache.said@gmail.com

Abstract: In this work, nickel oxide was fabricated on glass substrate at 450 °C by spray pyrolysis technique. The NiO layers were obtained with 0.05M molarity, which were deposited by various deposition rates 20, 40, 60 and 80 ml. The effects of deposition rate on the structural, electrical and optical properties were examined. All fabricated NiO thin films were observed a nanocrystalline a cubic structure with a strong (111) preferred orientation, it is only phase was observed in all deposited NiO. The film elaborated with 60 ml have a minimum value of crystallite size was 15.8 nm. All NiO thin films have an average transmittance is about 70 % in the visible region. The NiO thin films have a verity in the band gap energy from 3.34 to 3.51 eV because the effect of deposition, the minimum value was found at 80 ml, this condition have a lowest Urbach energy. The NiO thin films have an electrical resistivity was decreased from 0.625 to 0.152 ($\Omega \cdot \text{cm}$) with increasing the deposition rate from 20 to 80ml. The best results of NiO thin films are obtained in the deposition NiO films by 40 and 80 ml.

Key words: Nickel oxide; Thin films; Transparency; Spray pyrolysis method.

1. INTRODUCTION

Nickel oxide (NiO) is one of the p-type semiconducting material with optical band gap was varied between 3.6 to 4 eV [1]. In the latest research, the NiO is forming of nickel metal and oxygen element, it was found in the cubic structure with lattice parameter ($a = 0.4816 \text{ nm}$) [2]. NiO is one of the most important semiconductor materials in the latest research; this observation was based on the durability and excellent chemical stability in any solvent, low toxicity in water, large span optical density, low cost and good thermal stability [3]. NiO was developed as thin films to be used as a gas sensing application due to their good optical transparent in visible and good electrical conductivity [4,5]. The use of NiO thin films in the detection of toxic gases has a role in improving the physico-chemical properties, by researching how to prepare and any possible method. Gavale et al. [6] studied the physical properties of nanocrystalline NiO thin films fabricated by spray pyrolysis deposition, where investigated the influence of film thickness on the structural, morphological and optical characterizations of nanocrystalline NiO films, they found that the crystallinity and the morphological properties were increased with increasing the film thickness, also obtained a good transmission in the region of visible is found to be 80% with optical band gap energy found to in the range of 3.48 eV to 3.53 eV.

However, the NiO as the thin films were used in various applications due to the simplicity of synthesis can be investigated in solar cells [7], chemical sensors [8],

photodetectors [9], electro chromic mirrors [10], organic light emitting diodes [11], UV detectors [12], vanadium pentoxide diodes [13], and defrosting windows [14]. NiO thin films can be prepared by various methods likely molecular beam epitaxy techniques (MBE) [15], electrochemical techniques [16], chemical vapor techniques [17], sol-gel process [18], reactive evaporation [19], pulsed laser deposition techniques (PLD) [20], magnetron sputtering technique [21] and spray pyrolysis techniques [22]. The spray method was used for technological applications because it is one of the most important techniques to deposition a large-scale production. The prepared thin films by this method have a good adhesion mechanical, and good electrical conductivity; also it has a high optical transparency and magnetic properties of nanostructures NiO.

In the present research work, the nanocrystalline NiO thin films were fabricated to find a good high crystalline structure, good optical and electrical characterizations for further applications in gas sensing. In the present work, nanostructure NiO thin films were investigated, which are elaborated by spray pyrolysis method, the NiO was heated on the glass substrates at a deposition temperature of 450 °C with various deposition rates of

20, 40, 60 and 80 ml. the effect of deposition rate on structural, optical and electrical properties were investigated in the section of results and discussion.

2. EXPERIMENTAL

NiO solution was prepared by dissolving 0.05M of the $(\text{Ni}(\text{CH}_3\text{COO})_2 \cdot 4\text{H}_2\text{O})$ in the solvent of the absolute ethanol solution (99.995% purity), the stabilization was carried with stirring the NiO solution for 60 min without heating and addition of drops of HCl solution to find a 4 PH. The final solution of NiO was stirred and heated at 50 °C for 60 min to good transparent solution. The preparation was performed on the glass substrates by spray pyrolysis technique with heating at 450 °C. The NiO thin films were elaborated at 450 °C in air with various deposition rates of 20, 40, 60 and 80 ml. The crystalline structure of fabricated final films was carried by X-ray diffraction of the model (XRD, Bruker AXS-8D) with $(\lambda_{\text{CuK}\alpha} = 0.15406 \text{ nm})$ by varying the scanning range of (2θ) from 20° and 70°. The transmittance and absorbance of the spayed NiO films was investigated in the wavelength range of 300–900 nm by spectrophotometer (SHUMATZU 1800). Finally, the

electrical resistivity was calculated by the four point's techniques. All characterizations were measured at room temperature RT.

3. RESULTS AND DISCUSSION

The X-ray diffraction spectra's (XRD) of the fabricated NiO thin films by spray pyrolysis is presented in Figure 1. The fabricated NiO thin films were obtained at various deposition rates are 20, 40, 60 and 80 ml. The XRD spectrum of the sprayed NiO thin films was matched the structure of thin films of fabricated NiO is cubic structure with JCPDS (No. 73- 1519) [20]. From this data can observed an only diffraction peak at $2\theta = 37.4^\circ$, which is related to the plan of (111). All the spectra's of fabricated NiO thin films having one peak with higher in the sharper indicating that the obtain NiO thin film has a nanocrystalline structure. The good results were found for the film prepared with 60 and 80 ml due to the increase in the FWHM of the peaks. However, the preferred orientation is perpendicular with (104) plane. The crystallite size value of all deposited thin films of NiO was calculated by the Debye-Scherrer formula [23]:

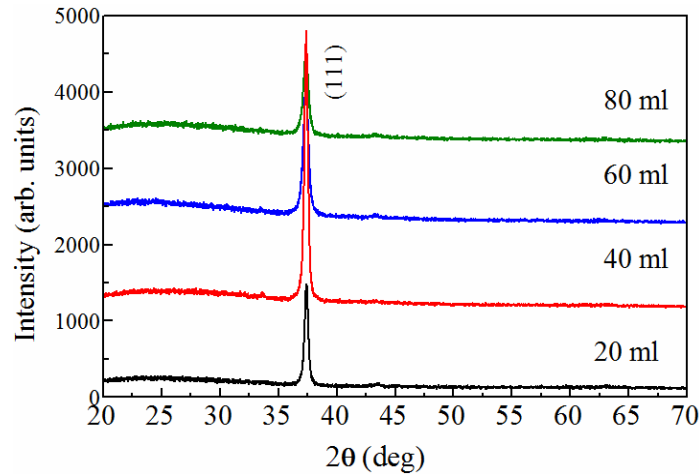


Figure 1. X-ray diffraction spectra of fabricated NiO thin films at different deposition rates

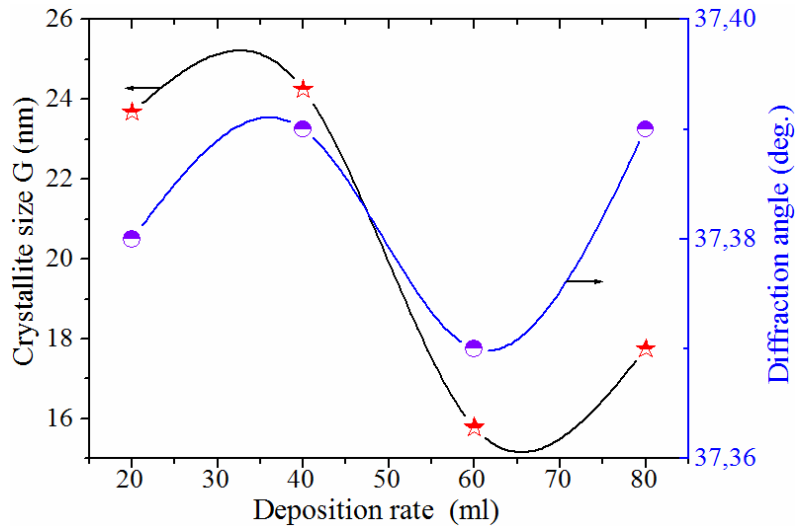


Figure 2. The variation of crystallite size and diffraction angle as a function of deposition rate of fabricated NiO thin films

$$G = \frac{0.9\lambda}{\beta \cos \theta} \quad (1)$$

where G is the crystallite size measured of (111) diffraction peak, λ is the longer of wavelength of X-ray ($\lambda = 1.5406 \text{ \AA}$), β is the FWHM and θ is the angle of (111) diffraction peak.

Reported in the Figure 2 the variation of the crystallite size and the diffraction angle of (111) crystal diffraction peak as a function of deposition rate. The crystallite sizes were stabilized at 20 ml and 40 ml of are taking two values 23.6 and 24.3 nm, respectively. Then decreased to minimum value was found at 60 ml of deposition rate it is 15.8 nm. The decrease in the crystallite size with the increase of deposition rate of fabricated NiO thin films was indicated to improve of crystalline structure. However, the decrease of diffraction angle with decreasing crystallite size caused by the existence of sufficiently thicker films in less strained state (or more relaxed state).

The Optical characterizations of fabricated NiO thin films fabricated at various deposition rates were performed by measuring the transmittance and absorbance in the wavelength region 300 to 900 nm, it are shown in Figure 3. Can see that the height transparency of the NiO thin films in the region of visible with an average transmission is about 70 %, so that the films exhibit high transparency by comparing with original nature, it is found by various literatures in the range 40 to 60% [24,25]. The fabricated NiO thin films have an absorption edge region (320–370 nm) was observed when the transmission was decreased, which is related the transition between the conduction band and valence the band. The inset of Figure 3 was present the variation of absorbance data of thin films of NiO, the absorption edge shifts was observed clearly at wavelength shorter than 400 nm. The absorption edge shifts of NiO thin films were decreased with increasing the deposition rate. As can be note, the optical property of thin films of NiO is affected by deposition rate.

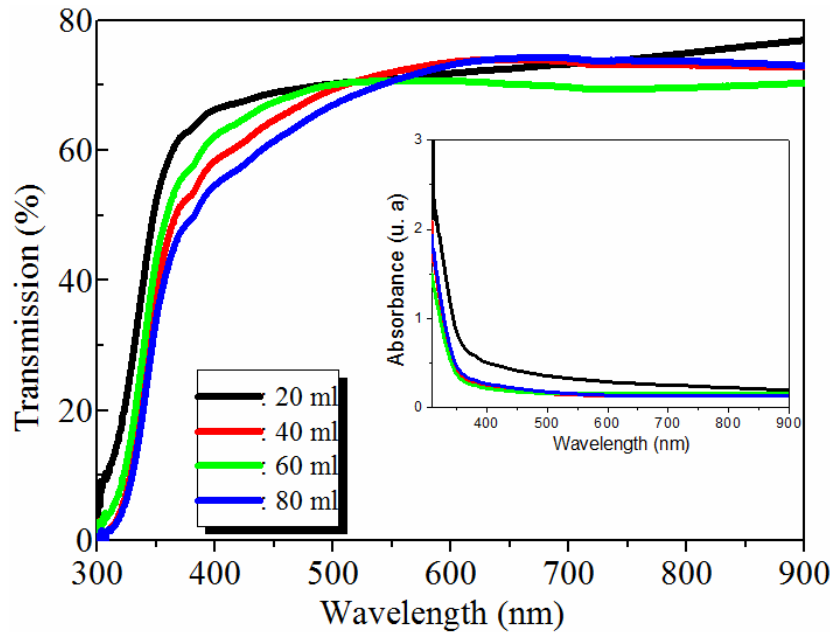


Figure 3. Transmission spectra of fabricated ZnO thin films as a function of deposition rate, the inset present the absorbance of the thin films

The role of deposition rate on the transmission of thin films of NiO was clearly observed on the thin films quality due to the higher transparency. But the absorption edge region of fabricated NiO film was observed to red shift can be explained by the changes in the optical bandgap energy. So that absorbance and the optical bandgap energy E_g of fabricated NiO thin films were determined by the following relations [3,26]:

$$A = \alpha d = -\ln T \quad (2)$$

$$(Ah\nu)^2 = C(h\nu - E_g) \quad (3)$$

where A is the absorbance of fabricated NiO thin films, α is the absorption coefficient, d is the film thickness, T is the transmission of fabricated NiO thin films; C is a

constant, $h\nu$ is the energy of photon ($h\nu = \frac{1240}{\lambda(\text{nm})}(\text{eV})$) and E_g the bandgap energy of the semiconductor. However, the disorder or Urbach energy (E_u) also was determined by the expression follow [27,28]:

$$A = A_0 \exp\left(\frac{h\nu}{E_u}\right) \quad (4)$$

where A_0 is a constant $h\nu$ is the energy of photon and E_u is the Urbach energy, the tail width of the Urbach energy was used for characterize the order of the defects. The variation of optical bandgap energy and Urbach energy of fabricated NiO thin films as a function of

deposition rate are presented in the Figure 4. The band gap energy was observed a smaller than 3.5 eV, it is change and decreased with the increase in the deposition rate from 3.51 to 3.34 eV of 20 to 80 ml, respectively. The diminution in the optical bandgap energy value of NiO thin films can be explain by the effect of quantum confinement due to the diminution in the crystallite size

of fabricated NiO thin films (see Figure 2). As can be seen in Figure 4 that the value of the Urbach energy was increases from 20 to 60 ml, and decrease to minimum value was found at 80 ml is 0.286 eV. This is can be related by the diminution of the crystallite size value (see Figure 2).

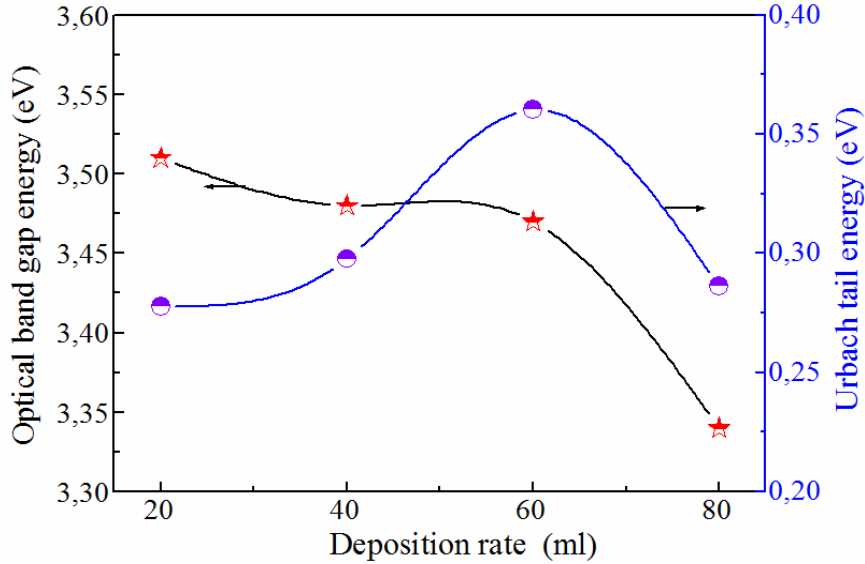


Figure 4. The variation of optical band gap E_g and Urbach energy E_u of fabricated NiO thin films with deposition rate

Figure 5 shows the variation with deposition rate of the electrical resistivity of fabricated NiO thin films. The deposited with various rates can be playing an important parameter in the fabricated NiO thin films. The variation of electrical resistivity of fabricated NiO thin films was measured at several deposition rates (increase in the film

thickness). These variations are rapid decreases to minimum value at 80 ml is 0.152 Ω .cm. The diminution in the electrical resistivity of fabricated NiO thin films can be explained by the diminution of defects, which was related by the decreasing in the Urbach energy (see Figure 4).

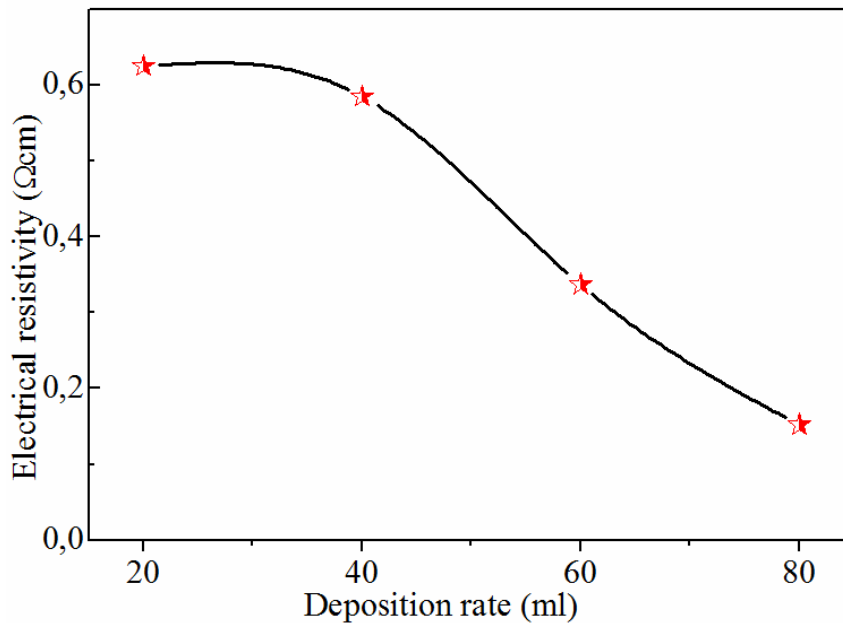


Figure 5. Electrical resistivity of fabricated NiO thin films at different deposition rate

4. CONCLUSIONS

In summary, the NiO thin films were fabricated by spray pyrolysis technique on the glass substrates at 450 °C with various deposition rates (film thickness). The crystalline structure, optical and electrical characterizations of nanostructures NiO thin films were investigated at several deposition rates. The fabricated NiO thin films were observed a nanocrystalline a cubic structure with a strong (111) preferred orientation, it is only phase was observed in all deposited films. The minimum value of crystallite size (15.8 nm) was measured of deposited film with 60 ml. The average transmittance is about 70 % was observed in all NiO thin films. The NiO thin films have a verity in the band gap energy from 3.34 to 3.51 eV because the effect of deposition, the minimum value was found at 80 ml, this condition have a lowest Urbach energy. The NiO thin film elaborated with 80 ml has a minimum electrical resistivity was 0.152 (Ω .cm). The NiO thin films sprayed with 60 and 80 ml have good structural, optical and electrical properties.

REFERENCES

- [1] Manouchehri, I., Mehrparvar, D., Moradian, R., Gholami, K., Osati, T., Investigation of structural and optical properties of copper doped NiO thin films deposited by RF magnetron reactive sputtering, *Optik*, 127 (2016) 8124–8129.
- [2] Krunks, M., Soon, J., Unt, T., Mere, A., Mikli, V., Deposition of p-type NiO films by chemical spray pyrolysis, *Vacuum*, 107 (2014) 242-246.
- [3] Diha, A., Benramache, S., Benhaoua, B., Transparent nanostructured Co doped NiO thin films deposited by sol-gel technique, *Optik*, 172 (2018) 832-839.
- [4] Benramache, S., Benhaoua, B., Influence of substrate temperature and Cobalt concentration on structural and optical properties of ZnO thin films prepared by Ultrasonic spray technique, *Superlattices and Microstructures*, 52 (2012) 807–815.
- [5] Benramache, S., Benhaoua, B., Influence of annealing temperature on structural and optical properties of ZnO: In thin films prepared by ultrasonic spray technique, *Superlattices and Microstructures*, 52 (2012) 1062–1070.
- [6] Gavale, H.S., Wagh, M.S., Ahirrao, R.B., Gosavi, S.R., Study of Physical Properties of Nanocrystalline NiO Thin Films Prepared by Spray Pyrolysis Technique, *Journal of Nanoscience and Technology*, 5 (2019) 610–612.
- [7] Benramache, S., Benhaoua, B., Chabane, F., Kachai, N., Elaboration and characterisation of ZnO thin films, *Matériaux & Techniques*, 100 (2012) 573–580.
- [8] Jlassi, M., Sta, I., Hajji, M., Ezzaouia, H., Synthesis and characterization of nickel oxide thin films deposited on glass substrates using spray pyrolysis, *Applied Surface Science*, 308 (2014) 199–205.
- [9] Denayer, J., Bister, G., Simonis, P., Colson, P., Maho, A., Aubry, P., Vertruyen, B., Henrist, C., Lardot, V., Cambier, F., Cloots, R., Surfactant-assisted ultrasonic spray pyrolysis of nickel oxide and lithium-doped nickel oxide thin films, toward electrochromic applications, *Applied Surface Science*, 321 (2014) 61–69.
- [10] Berkat, L., Cattin, L., Reguig, A., Regragui, M., Bernède, J.C., Comparison of the physico-chemical properties of NiO thin films deposited by chemical bath deposition and by spray pyrolysis, *Materials Chemistry and Physics*, 89 (2005) 11–20.
- [11] Khodair, Z.T., Kamil, A.A., Abdalaah, Y.K., Effect of annealing on structural and optical properties of Ni_(1-x)Mn_xO nanostructures thin films, *Physica B*, 503 (2016) 55–63.
- [12] Amor, M.B., Boukhachem, A., Labidi, A., Boubaker, K., Amlouk, M., Physical investigations on Cd doped NiO thin films along with ethanol sensing at relatively low temperature, *Journal of Alloys and Compounds*, 693 (2017) 490-499.
- [13] Kim, H., Yang, S., Ahn, S.H., Lee, C.S., Effect of particle size on various substrates for deposition of NiO film via nanoparticle deposition system, *Thin Solid Films*, 600 (2016) 109–118.
- [14] Moghe, S., Acharya, A.D., Panda, R., Shrivastava, S.B., Gangrade, M., Shripathi, T., Ganesan, V., Effect of copper doping on the change in the optical absorption behavior in NiO thin films, *Renewable Energy*, 46 (2012) 43-48.
- [15] Cattin, L., Reguig, B.A., Khelil, A., Morsli, M., Benchouk, K., Bernède, J.C., Properties of NiO thin films deposited by chemical spray pyrolysis using different precursor solutions, *Applied Surface Science*, 254 (2008) 5814–5821.
- [16] Reguig, B.A., Khelil, A., Cattin, L., Morsli, M., Bernède, J.C., Properties of NiO thin films deposited by intermittent spray pyrolysis process, *Applied Surface Science*, 253 (2007) 4330–4334.
- [17] Desai, J.D., Min, S.K., Jung, K.D., Joo, O.S., Spray pyrolytic synthesis of large area NiOx thin films from aqueous nickel acetate solutions, *Applied Surface Science*, 253 (2006) 1781–1786.
- [18] Chen, C., Perdomo, P.J., Fernandez, M., Barbeito, A., Wang, C., Porous NiO/graphene composite thin films as high performance anodes for lithium-ion batteries, *Journal of Energy Storage*, 8 (2016) 198–204.
- [19] Shi, N., Yu, S., Chen, S., Ge L., Chen, H., Guo, L., Dense thin YSZ electrolyte films prepared by a vacuum slurry deposition technique for SOFCs, *Ceramics International*, 43 (2017) 182–186.
- [20] Patil, P.S., Kadam, L.D., Preparation and characterization of spray pyrolyzed nickel oxide (NiO) thin films, *Applied Surface Science*, 199 (2002) 211–221.
- [21] Chen, C., Perdomo, P.J., Fernandez, M., Barbeito, A., Porous NiO/graphene composite thin films as high performance anodes for lithium-ion batteries, *Journal of Energy Storage*, 8 (2016) 198–204.
- [22] Amiruddin, R., Kumar, M.C.S., Role of p-NiO electron blocking layers in fabrication of (P-

- N):ZnO/Al:ZnO UV photodiodes, *Current Applied Physics*, 16 (2016) 1052-1061.
- [23] Diha, A., Benramache, S., Fellah, L., The Crystalline Structure, Optical and Conductivity Properties of Fluorine Doped ZnO Nanoparticles, *Journal of Nano- and Electronic Physics*, 11 (2019) 03002.
- [24] Ukoba, K.O., Eloka-Eboka, A.C., Inambao, F.L., Review of nanostructured NiO thin film deposition using the spray pyrolysis technique, *Renewable and Sustainable Energy Reviews*, 82 (2018) 2900-2915.
- [25] Iftimie, S., Mallet, R., Merigeon, J., Ion, L., Girtan, M., Antohe, S., On the structural, morphological and optical properties of ITO, ZnO, ZnO:Al and NiO thin films obtained by thermal oxidation, *Digest Journal of Nanomaterials and Biostructures*, 10 (2015) 221 -229.
- [26] Benramache, S, Aoun, Y, Lakel, S, Mourghade, H, Gacem, R, Benhaoua, B, Effect of Annealing Temperature on Structural, Optical and Electrical Properties of ZnO Thin Films Prepared by Sol-Gel Method, *Journal of Nano- and Electronic Physics*, 10 (2018) 06032.
- [27] Daranfed, W., Aida, M.S., Hafdallah, A., Lekiket, H., Substrate temperature influence on ZnS thin films prepared by ultrasonic spray, *Thin Solid Films*, 518 (2009) 1082–1084.
- [28] Benramache, S., Fabrication and characterisation of ZnO thin film by sol–Gel technique, *Annals of West University of Timisoara-Physics*, 61 (1), 64-70.

PROPERTIES AND STRUCTURE OF LOW-CEMENT CONCRETE ACCORDING TO ITS COMPOSITIONAL PARAMETERS

**Dan Nicolae UNGUREANU, Elena Valentina STOIAN, Florin TOMA, Daniel ANCULESCU,
 Alexandru Gabriel COLȚA, Nicolae ANGELESCU, Vasile BRATU**

Faculty of Materials Engineering and Mechanics, Valahia University of Targoviste, 13 Aleea Sinaia Street, Targoviste,
 Romania

E-mail: elenastoian22@gmail.com

Abstract: Refractory concretes with the usual cement content (about 20%) present, besides their well-known advantages, several important disadvantages which make such concretes unfit for certain applications. The relatively high CaO content in concretes, the presence of even small amounts of SiO₂ and Fe₂O₃ in cement reduce in the first place the concretes refractoriness; if their relatively high porosity is also taken into account, the concretes behavior is further damaged in regard to the structural and thermal-chemical stability, especially at their high operating temperatures. This work is an attempt to correct the shortcomings shown by reducing the cement dosage and using appropriate admixtures in the technological process of concrete making.

Keywords: cement dosage, admixtures, aluminous cement, different aggregates, mechanical and structural properties, refractoriness

1. INTRODUCTION

A possible way to avoid the disadvantages encountered in refractory concrete with normal cement dosage (20%) is to decrease the cement content, using at the same time such admixtures whose effects would make up for the decrease of the cement ratio; this requirement would be accompanied, at the same time, by an improvement of the mechanical properties of the high cement concrete. The desirable effects of the mentioned additives could be essentially achieved by:

- their dispersing action, with an increase of the specific volume of the products of hydration, having positive consequences on the gel/space ratio and on the paste-aggregate adherence [1-8];
- their action on the hardening process in relation with their dispersing influence; by modifying the chemical-morphological nature of the hardening products, such

additives improve the paste texture of the concrete and influence its physical-mechanical characteristics (certain additives of this kind can also act as hardening agents of the oxide-acid type as in the case of the Cr⁺⁶ substances [6 - 14].

2. EXPERIMENTAL CONDITIONS

A CA2 type (R₀₀₆=20%) cement and three aggregate types: tabular alumina (99.5% Al₂O₃), fire-clay (49,37% Al₂O₃ and 47,6% SiO₂) and sintered magnesite have been used in order to obtain the concrete mixture under investigation. From a granulometric point of view the mixture have been calculated taking as a model the Boloney granulometric curve. The Calcium Lignosulphonate (LSC) and a phosphatic compound (TFS) have been used as additives. Table 1 shows the composition of the concretes under investigation.

Table 1. Composition of concretes

Concrete Index	Cement Contents	Aggregate		Aditives		Water Gravimetric Ratio in the Concrete [%]	Refractoriness [°C]
		Nature	Maximum Grain Size [mm]	LSC	TFS		
1	20	Tabular alumina	3	-	-	10.8	1820
2	15	Idem	3	-	-	9.8	1840
3	12.5	Idem	3	-	-	9.4	1850
4	10	Idem	3	-	-	9.2	1850
5	7.5	Idem	3	-	-	8.9	1850
6	5	Idem	3	-	-	8.7	1850

7	10	Idem	6	-	-	7.3	1850
8	10	Fire-Clay	6	-	-	9.3	1700
9	10	Sintered magnesite	6	-	-	7.3	unspecifed
10	12.5	Tubular alumina	3	0.0125	-	9.0	1850
11	12.5	Idem	3	0.05	-	9.0	1850
12	12.5	Idem	3	0.1	-	9.0	1850
13	12.5	Idem	3	0.5	-	9.0	1850
14	12.5	Idem	3	-	0.05	8.8	1850
15	12.5	Idem	3	-	0.125	8.8	1850
16	12.5	Idem	3	-	0.5	8.8	1850
17	12.5	Idem	3	-	1	8.8	1850
18	12.5	Idem	3	-	2	8.8	1850
19	12.5	Idem	3	-	3	8.8	1850
20	12.5	Idem	3	-	5	8.8	1850

Porosity and strength determinations have been carried out on free-hardened concrete samples for different periods (1, 3, 7 and 28 days); after drying at 110⁰C; these heating characteristics have been studied up to 1700-1800⁰C by trials on free hardened samples for 3 days.

3. RESULTS AND INTERPRETATIONS

The results obtained have been graphically processed and are presented in Fig.1-5 (the curves in the figures have numbers which correspond to the concretes index, according to Table 1).

A close examination of the cement contents influence on

the concrete strength shows a sharp decrease of the latter when cement content is lower than 10-15% - including heat treatment; the same applies to porosity (Fig. 1). Strength decrease under circumstances of reduced porosity can be explained by the paste high porosity and by the inadequate paste-aggregate adherence in low cement concretes without hardening agents or dispersing additives. These additives remove the difficulties (Fig.2 and Fig.3), maintaining the advantage of a higher refractoriness in low cement concretes; thus, when using an optimal content of additives, it is possible to obtain strength of 130 and 300% for 12.5% cement refractory concretes as so compared with the corresponding concretes with 20% aluminous cement and without additives.

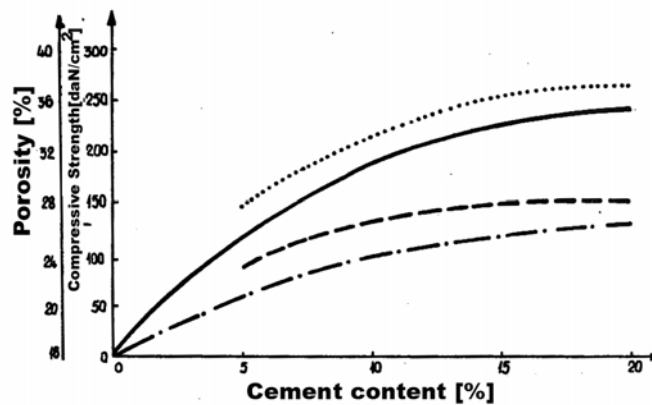


Figure 1. Concrete strength and porosity variation as function of the cement contents (concretes 1-6):

— compression strength 3 days after hardening; - · - compression strength for concretes heated at 1200⁰C;
 - - porosity, 3 days after hardening; · · · porosity, for concretes heated at 1200⁰C

The TFS phosphates additive makes for a significant increase of the concrete strength even for short periods of hardening; in the case of optimal additive ratios its effect is the trebling of the strength as compared to the corresponding concrete without additives (Fig.3 a), the explanation lying in the sharp porosity decrease as a result of its high dispersating action. There is an obvious parallelism between the porosity variation and the strength variation (Fig.3 a and Fig.3 b). It is worth noticing that higher phosphates additive ratios determining a stronger dispersing effect on the new

hydration products without delaying the cement hydration lead to a significant reduction of the concrete porosity during the 1-3 [7] days of hardening; for longer hardening intervals not only that the concrete porosity is not reduced but, on the contrary, it increases, this fact being shown by the strength reduction; the causes of this behavior must be subject to further examination. Small TFS ratios lead to a continuous porosity decrease and therefore to a continuous increase in time of the concrete strength; this effect is a maximum at an optimal addition ratio.

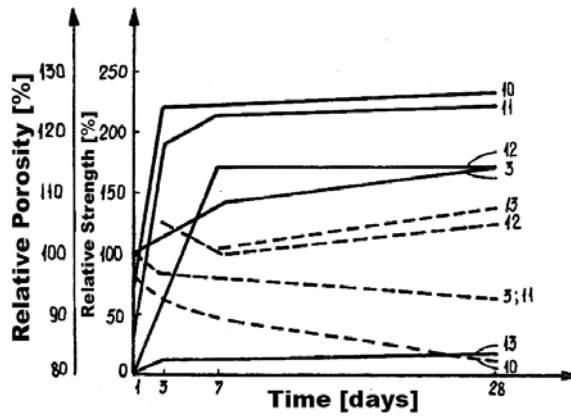
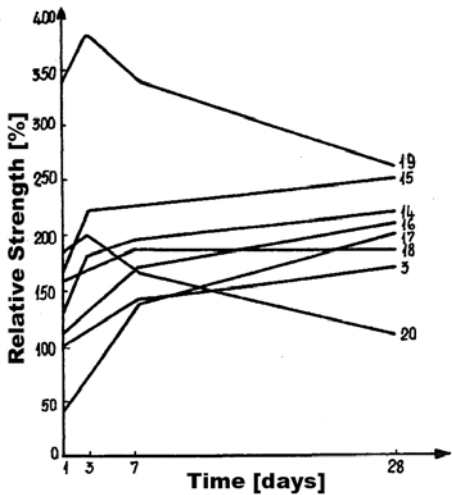


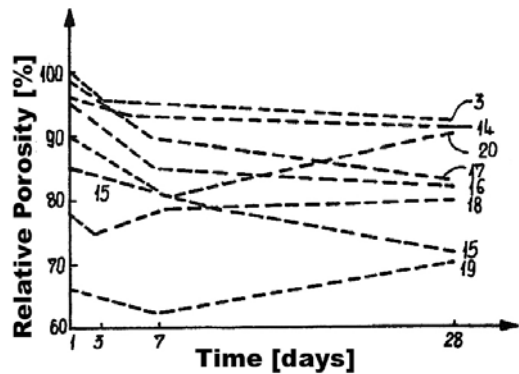
Figure 2. Concrete strength and porosity evolution in time, as function of the LSC ratio:
 — compression strength; --- porosity

The LSC additive is a delay factor of the cement hydration, so that, although it has, as a dispersing agent, a positive influence on the hardened concrete texture, for short periods of hardening, a lower strength than in the

case of the standard concrete (Fig.2) could be obtained, even in the case of optimum LSC ratios; it should also be noticed that the higher the ratio, the more intense the LSC delaying action.



a



b

Figure 3. Concrete strength (a) and porosity (b) evolution in time, as function of TFS ratio

Taking into account the influence of the compositions under examination, based on tabular alumina have the best of the aggregate nature for any it appears that the concretes behavior (Table 1 and Fig. 4); in the case of the same aggregate, the increase of its maximum grain-size leads to the concrete strength improvement.

We must point out here that, although the concretes with sintered magnesite have the lowest porosities, they also have the lowest strengths; this behavior is accounted for by the regular form and the less coarse surface, also by the nonaluminous nature of the calcined magnesite grains, which lead to a less void fraction and a weaker paste-aggregate adherence than when using tabular alumina or fire-clay.

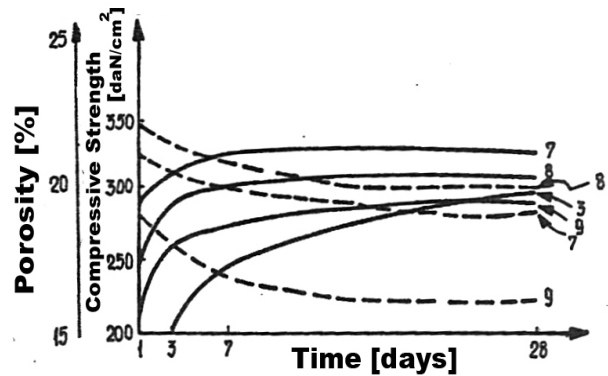


Figure 4. The time variation of the strength and porosity of the 10% aluminous cement concretes as function of the aggregate nature and size: — compression strength; --- porosity

Under conditions of heat treatment a strength drop is found to occur while there are sharp porosity increases at temperatures ranging from 800-1200°C, after which, following the ceramic hardening, both a densification and a strength increase take place up to temperatures depending on the concrete refractoriness.

The compositions having as additive dispersing agents in optimal ratios obviously have higher strengths than the standard, also at higher temperatures (Fig.5).

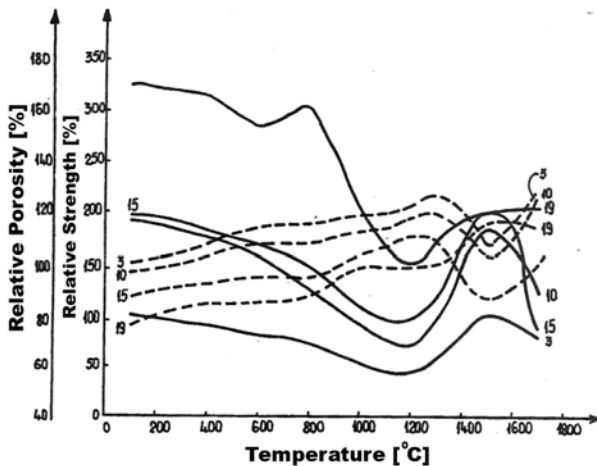


Figure 5. The compression strength variation and the porosity variation of the concretes with or without dispersing additives, as function of the temperature: — compression strength; --- porosity

Among the studied concretes, the 3% TFS composition has the best behavior; at the same time it displays the severest strength drop, while at temperatures around 1500-1600 °C it has strengths equivalent to those of the 0,125% LSC as TFS concretes, but notably higher than those of the standard concrete.

A peculiarity of this composition is the maximal strength noticed at about 800°C, which could be explained by the polycondensation of the phosphates additive for such an addition ratio and at the above-mentioned temperature this fact could have a very important effect on the concrete mechanical characteristics.

4. CONCLUSIONS

By interpreting the results obtained we may draw several important conclusions:

- the cement content decrease in refractory concretes leads to a sharp porosity decrease and to a significant refractoriness increase;
- the cement content decrease in refractory concretes under 10-15% also determines a sudden reduction of the concrete strength, as a consequence of the paste high porosity and of the inadequate paste-aggregate adherence;
- the above-mentioned drawbacks of the low cement contents are removed by using dispersing additives; there is an optimal ratio of the dispersing additives related to the modifications they are determining in the

cement hydration kinetics and in the concrete paste texture;

- the dispersing additives influence is also obvious in the concrete behavior at high temperatures; their mechanical characteristics are superior to those of the standard concrete, also at high temperatures.

REFERENCES

- [1] Prost, L., - L'industrie Ceramique 661, 279 (1975).
- [2] Prost, L., - Proceed.Internat.Symp.Refractory Concretes. Karlovy-Vary,Czechoslovakia, 275 (1971).
- [3] Teoreanu, I., Angelescu, N., - Materiale de Constructii.8 (3),127, (1978).
- [4] Teoreanu, I., Angelescu, N., CrO₃ Influence on Low Cement Refractory Concretes Properties and Hardening". CONSILOX III, 11-13 septembrie 1980, Brasov
- [5] Ionita, C., Angelescu, N. Abdelgader, H. S., Bratu, V., Stanciu, D., Ion, I. - *The influence of hydration on the mechanical strength of the high aluminous cement*. Proceedings of The International Conference on Advances in Cement and Concrete in Africa, ACCTA 2013, Johannesburg, South Africa, 2013, pp. 961 – 968.
- [6] Ionita, C., Angelescu, N., Amziane, S. - *Caracterizarea cimenturilor superaluminose utilizând analiza termogravimetrică și difracția de raze X*. Culegerea de lucrari a Celei de-a XI-a Conferinta de Stiinta si Ingineria Materialelor Oxidice – CONSILOX XI. Bucuresti Romania, Octombrie, 2012.
- [7] Angelescu, N., Ionita, C., Ion, I., Stanciu, D. - *Silica Fume Additivated Special Concretes*. Abstract Volume of 4th International Conference on Seismic Retrofitting, Tabriz, Iran, 2 – 4 mai 2012, p. 9.
- [8] Angelescu, N., Dan Ungureanu, Florin Toma - *Special refractories resistant to the melt metals and slags attack*. The Scientific Bulletin of VALAHIA University – MATERIALS and MECHANICS, DOI 10.2478/bsmm-2019-0004, Volume 17, Issue 16 (Jun 2019), p. 28 - 31.
- [9] Lankard, D R, et al.- *Refractory Concretes for Steelplant Applications*, Refract. Journal, 1, pp.6, 1986.
- [10] Li, Z, Ye, G. - *Bonding and Recent Progress of Monolithic Refractories*, Interceram, 41, (3), pp. 169- 172, 1992.
- [11] Moreau, J. - *Development of low Cement and Ultra low Cement Castable in Combustion Chamber and Boilers of Domestic Waste Incinerators*”, Interceram, (Refractory Special Issue), 1987, 37, pp. 8.
- [12] Avis, R., Clavaud, B. and Randal, JP. - *Monolithic Permanent Linings in Tundishes*, Interceram, (Special Issue), 36, pp. 33-38, 1987.
- [13] Auvray, J. M. *Elaboration et caracterisation a haute temperature de betons refractaires a base d'alumine spinelle*, doctorate thesis, Universitatea din Limoges, Janvier, 2003.
- [14] Angelescu, N., Ionita, G. Nicolae, A. - *New Special Concretes*, World of Coal Ash (WOCA 2007), Covington - Cincinnati, SUA, 2007

NUMERICAL KINEMATICAL ANALYSIS OF THE SHAPING MECHANISM

Vladimir Dragoş TĂTARU¹, Mircea Bogdan TĂTARU²

¹ University “Valahia” of Târgovişte, ² University of Oradea

E-mail: vdtataru@gmail.com, btataru@uoradea.ro

Abstract: *The paper deals with the complete kinematical analysis of the mechanism that enters the machine tool structure designed to generate, in particular, plane surfaces. A machine tool of this kind is called shaping machine. For this purpose, Euler’s relations concerning the velocities distribution, written in projections on the fix reference system axes will be used. Starting from these relations we will get to a system of the first order linear differential equations whose unknowns are the kinematical parameters of the mechanism elements. The variation in time of these parameters will be obtained by solving the differential equations system the differential equations system using numerical integration methods.*

Keywords: *kinematical analysis, kinematical parameters, numerical integration methods*

NOMENCLATURE

$T(Oxyz)$ -fix reference system

s_{23} -the relative displacement parameter

v_{23} -the relative velocity

a_{23} -the relative acceleration

\vec{u}_{23} -unit vector that specifies the direction of the $\vec{O_3O_4}$ vector

u_{23} -column matrix associated to the \vec{u}_{23} unit vector

l_1 -length of the “1” element

l_2 -length of the “2” element

l_4 -length of the “4” element

x_{O_1}, y_{O_1} -coordinates of the O_1 point relative to the fixed reference system

$v_{O_1,x}, v_{O_1,y}$ -projections of the speed of the O_1 point on the axes of the fixed reference system axes

$a_{O_1,x}, a_{O_1,y}$ -projections of the acceleration of the O_1 point on the axes of the fixed reference system axes

x_{O_2}, y_{O_2} -coordinates of the O_2 point relative to the fixed reference system

$v_{O_2,x}, v_{O_2,y}$ -projections of the speed of the O_2 point on the axes of the fixed reference system axes

$a_{O_2,x}, a_{O_2,y}$ -projections of the acceleration of the O_2 point on the axes of the fixed reference system axes

x_{O_3}, y_{O_3} -coordinates of the O_3 point relative to the fixed reference system

$v_{O_3,x}, v_{O_3,y}$ -projections of the speed of the O_3 point on the axes of the fixed reference system axes

$a_{O_3,x}, a_{O_3,y}$ -projections of the acceleration of the O_3 point on the axes of the fixed reference system axes

x_{O_4}, y_{O_4} -coordinates of the O_4 point relative to the fixed reference system

$v_{O_4,x}, v_{O_4,y}$ -projections of the speed of the O_4 point on the axes of the fixed reference system axes

$a_{O_4,x}, a_{O_4,y}$ -projections of the acceleration of the O_4 point on the axes of the fixed reference system axes

x_{O_5}, y_{O_5} -coordinates of the O_5 point relative to the fixed reference system

$v_{O_5,x}, v_{O_5,y}$ -projections of the speed of the O_5 point on the axes of the fixed reference system axes

a_{O_5x}, a_{O_5y} -projections of the acceleration of the O_5 point on the axes of the fixed reference system axes

$\mathbf{0}_{m \times n}$ -zero matrix with “m” lines and “n” columns

T -exponent that indicates the transposition matrix operation

1. INTRODUCTION

The mechanism presented in the figure below will be considered [2] (Fig.1).The “1” element of the mechanism is linked to the “2” element by a joint. The “2” element is linked to the “3” element by a slide.

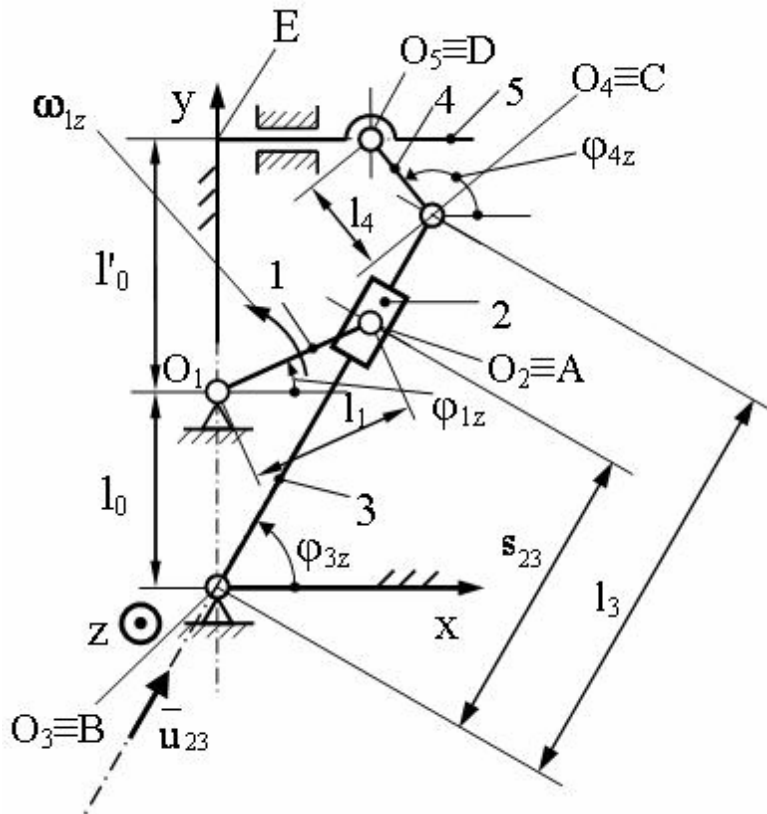


Figure 1. Shaping mechanism

The “3”, “4” and “5” elements are linked each other by joints. The “5” element is linked to the fixed element by a joint. All mechanism elements describe motions in xOy plane. We aim ourselves to perform the complete kinematical analysis of this mechanism.

$$\vec{v}_{O_1} + \vec{\omega}_1 \times \vec{O_1O_2} - \vec{v}_{O_2} = \vec{0} \quad (1)$$

The above relationship may be written in an equivalent form as follows:

2. ESTABLISHING LINK RELATIONS BETWEEN THE FIRST ORDER KINEMATICAL PARAMETERS OF THE MECHANISM ELEMENTS

$$\vec{v}_{O_1} + \vec{\omega}_1 \times (\vec{r}_{O_2} - \vec{r}_{O_1}) - \vec{v}_{O_2} = \vec{0} \quad (2)$$

Between the speed of the O_1 point and the velocity of the O_2 point we may write Euler’s relation concerning the distribution of velocities because they belong to the same rigid solid body. In vector form in projections on the fix reference system $T(Oxyz)$, it may be written as follows:

In the relationship (2) \vec{r}_{O_1} and \vec{r}_{O_2} represent the position vectors of the O_1 and O_2 points respectively relative to the fix reference system $T(Oxyz)$. The relationship (2) may also be written in matrix form as follows:

$$\vec{v}_{O_1} + \vec{\omega}_1 \cdot (\vec{r}_{O_2} - \vec{r}_{O_1}) - \vec{v}_{O_2} = \mathbf{0}_{2 \times 1} = [0 \ 1 \ 0]^T \quad (3)$$

In the relationship (3) the terms that occur may be written as follows:

$$\mathbf{v}_{O_1} = [v_{O_1x} \mid v_{O_1y}]^T \quad (4)$$

$$\tilde{\boldsymbol{\omega}}_1 = \begin{bmatrix} 0 & -\omega_{1z} \\ \omega_{1z} & 0 \end{bmatrix} \quad (5)$$

$$\mathbf{r}_{O_1} = [x_{O_1} \mid y_{O_1}]^T \quad (6)$$

$$\mathbf{r}_{O_2} = [x_{O_2} \mid y_{O_2}]^T \quad (7)$$

$$\mathbf{v}_{O_2} = [v_{O_2x} \mid v_{O_2y}]^T \quad (8)$$

The following two scalar relationships can be deduced from the matrix relationship (3):

$$v_{O_1x} - \omega_{1z} \cdot (y_{O_2} - y_{O_1}) - v_{O_2x} = 0 \quad (9)$$

$$v_{O_1y} + \omega_{1z} \cdot (x_{O_2} - x_{O_1}) - v_{O_2y} = 0 \quad (10)$$

The scalar relationships (9) and (10) may be written together in matrix form as follows:

$$\mathbf{A}_{11} \cdot \mathbf{v}_1 + \mathbf{A}_{12} \cdot \mathbf{v}_2 = \mathbf{0}_{2 \times 1} = [0 \mid 0]^T \quad (11)$$

In the relationship (11) the terms that occur have the following expressions:

$$\mathbf{A}_{11} = \begin{bmatrix} 1 & 0 & -(y_{O_2} - y_{O_1}) \\ 0 & 1 & (x_{O_2} - x_{O_1}) \end{bmatrix} \quad (12)$$

$$\mathbf{A}_{12} = \begin{bmatrix} -1 & 0 & 0 & 0 \\ 0 & -1 & 0 & 0 \end{bmatrix} \quad (13)$$

$$\mathbf{v}_1 = [v_{O_1x} \mid v_{O_1y} \mid \omega_{1z}]^T \quad (14)$$

$$\mathbf{v}_2 = [v_{O_2x} \mid v_{O_2y} \mid \omega_{2z} \mid v_{23}]^T \quad (15)$$

Between the speed of the O_2 point and the speed of the O_3 point, taking into account the relative movement between the “2” and “3” elements, the following matrix relationship in projections on the fix reference frame system axe may be written:

$$\mathbf{v}_{O_3} + \tilde{\boldsymbol{\omega}}_3 \cdot (\mathbf{r}_{O_2} - \mathbf{r}_{O_3}) + \underbrace{\dot{s}_{23} \cdot (1/l_3)}_{u_{23}} \cdot (\mathbf{r}_{O_4} - \mathbf{r}_{O_3}) - \mathbf{v}_{O_2} = \mathbf{0}_{2 \times 1} = [0 \mid 0]^T \quad (16)$$

In the relationship (16) the terms that occur may be written in the following form:

$$\mathbf{v}_{O_3} = [v_{O_3x} \mid v_{O_3y}]^T \quad (17)$$

$$\tilde{\boldsymbol{\omega}}_3 = \begin{bmatrix} 0 & -\omega_{3z} \\ \omega_{3z} & 0 \end{bmatrix} \quad (18)$$

$$\mathbf{r}_{O_2} = [x_{O_2} \mid y_{O_2}]^T \quad (19)$$

$$\mathbf{r}_{O_3} = [x_{O_3} \mid y_{O_3}]^T \quad (20)$$

$$\mathbf{r}_{O_4} = [x_{O_4} \mid y_{O_4}]^T \quad (21)$$

$$\mathbf{v}_{O_2} = [v_{O_2x} \mid v_{O_2y}]^T \quad (22)$$

The matrix relationship (16) is equivalent to two scalar relationships:

$$-v_{O_2x} + v_{O_3x} - (y_{O_2} - y_{O_3}) \cdot \omega_{3z} + (1/l_3) \cdot (x_{O_4} - x_{O_3}) \cdot v_{23} = 0 \quad (23)$$

$$-v_{O_2y} + v_{O_3y} + (x_{O_2} - x_{O_1}) \cdot \omega_{3z} + (1/l_3) \cdot (y_{O_4} - y_{O_3}) \cdot v_{23} = 0 \quad (24)$$

In the relationships (23) and (24) v_{23} represents the relative velocity of the slide “2” relative to the solid rigid “3”. It is calculated using the following relationship:

$$v_{23} = \dot{s}_{23} = ds_{23}/dt \quad (25)$$

The rigid solids “2” and “3” are linked together by a slide so their angular velocities are equal to each other:

$$\omega_{2z} = \omega_{3z} \quad (26)$$

The relationships (23), (24) and (26) may be written together in matrix form as follows:

$$\mathbf{A}_{22} \cdot \mathbf{v}_2 + \mathbf{A}_{23} \cdot \mathbf{v}_3 = \mathbf{0}_{3 \times 1} = [0 \mid 0 \mid 0]^T \quad (27)$$

$$\mathbf{A}_{22} = \begin{bmatrix} -1 & 0 & 0 & (1/l_3) \cdot (x_{O_4} - x_{O_3}) \\ 0 & -1 & 0 & (1/l_3) \cdot (y_{O_4} - y_{O_3}) \\ 0 & 0 & 1 & 0 \end{bmatrix} \quad (28)$$

$$\mathbf{v}_2 = [v_{O_2x} \mid v_{O_2y} \mid \omega_{2z} \mid v_{23}]^T \quad (29)$$

$$\mathbf{A}_{23} = \begin{bmatrix} 1 & 0 & -(y_{O_2} - y_{O_3}) \\ 0 & 1 & (x_{O_2} - x_{O_3}) \\ 0 & 0 & -1 \end{bmatrix} \quad (30)$$

$$\mathbf{v}_3 = [v_{O_3x} \mid v_{O_3y} \mid \omega_{3z}]^T \quad (31)$$

Between the speeds of O_3 and O_4 points the following matrix relationship may be written:

$$\mathbf{v}_{O_3} + \tilde{\omega}_3 \cdot (\mathbf{r}_{O_4} - \mathbf{r}_{O_3}) - \mathbf{v}_{O_4} = \mathbf{0}_{2 \times 1} = [0 \mid 0]^T \quad (32)$$

In the relationship (32) the terms that occur may be written as follows:

$$\mathbf{r}_{O_4} = [x_{O_4} \mid y_{O_4}]^T \quad (33)$$

$$\mathbf{v}_{O_4} = [v_{O_4x} \mid v_{O_4y}]^T \quad (34)$$

The matrix relation (32) is equivalent to two scalar relationships as follows:

$$v_{O_3x} - \omega_{3z} \cdot (y_{O_4} - y_{O_3}) - v_{O_4x} = 0 \quad (35)$$

$$v_{O_3y} + \omega_{3z} \cdot (x_{O_4} - x_{O_3}) - v_{O_4y} = 0 \quad (36)$$

The relationships (35) and (36) may be written together in matrix form as follows:

$$\mathbf{A}_{33} \cdot \mathbf{v}_3 + \mathbf{A}_{34} \cdot \mathbf{v}_4 = \mathbf{0}_{2 \times 1} = [0 \mid 0]^T \quad (37)$$

$$\mathbf{A}_{33} = \begin{bmatrix} 1 & 0 & -(y_{O_4} - y_{O_3}) \\ 0 & 1 & (x_{O_4} - x_{O_3}) \end{bmatrix} \quad (38)$$

$$\mathbf{v}_3 = [v_{O_3x} \mid v_{O_3y} \mid \omega_{3z}]^T \quad (39)$$

$$\mathbf{A}_{34} = \begin{bmatrix} -1 & 0 & 0 \\ 0 & -1 & 0 \end{bmatrix} \quad (40)$$

$$\mathbf{v}_4 = [v_{O_4x} \mid v_{O_4y} \mid \omega_{4z}]^T \quad (41)$$

Between the velocities of the O_4 and O_5 points the following matrix relationship given by Euler’s relation concerning the speeds distribution in projections on the fix reference system axes $T(Oxyz)$ may be written as follows:

$$\mathbf{v}_{O_4} + \tilde{\omega}_4 \cdot (\mathbf{r}_{O_5} - \mathbf{r}_{O_4}) - \mathbf{v}_{O_5} = \mathbf{0}_{2 \times 1} = [0 \mid 0]^T \quad (42)$$

$$\tilde{\omega}_4 = \begin{bmatrix} 0 & -\omega_{4z} \\ \omega_{4z} & 0 \end{bmatrix} \quad (43)$$

$$\mathbf{r}_{O_5} = [x_{O_5} \mid y_{O_5}]^T \quad (44)$$

$$\mathbf{v}_{O_5} = [v_{O_5x} \mid v_{O_5y}]^T \quad (45)$$

The matrix relationship (42) is equivalent to two scalar relationships as follows:

$$v_{O_4x} - \omega_{4z} \cdot (y_{O_5} - y_{O_4}) - v_{O_5x} = 0 \quad (46)$$

$$v_{O_4y} + \omega_{4z} \cdot (x_{O_5} - x_{O_4}) - v_{O_5y} = 0 \quad (47)$$

The scalar relationships (46) and (47) may be written together in matrix form as follows:

$$\mathbf{A}_{44} \cdot \mathbf{v}_4 + \mathbf{A}_{45} \cdot \mathbf{v}_5 = \mathbf{0}_{2 \times 1} = [0 \mid 0]^T \quad (48)$$

$$\mathbf{A}_{44} = \begin{bmatrix} 1 & 0 & -(y_{O_5} - y_{O_4}) \\ 0 & 1 & (x_{O_5} - x_{O_4}) \end{bmatrix} \quad (49)$$

$$\mathbf{v}_4 = [v_{O_4x} \mid v_{O_4y} \mid \omega_{4z}]^T \quad (50)$$

$$\mathbf{A}_{45} = \begin{bmatrix} -1 & 0 \\ 0 & -1 \end{bmatrix} \quad (51)$$

$$\mathbf{v}_5 = [v_{O_5x} \mid v_{O_5y} \mid \omega_{5z}]^T \quad (52)$$

Taking into account that the “5” element of the mechanism is connected to the fix element by a slide, its angular velocity ω_{5z} and the projection along Oy axis are equal to zero because its movement is a translational movement along Ox axis:

$$v_{O_5y} = 0 \quad (53)$$

$$\omega_{5z} = 0 \quad (54)$$

The scalar relationships (53) and (54) may be written together in matrix form as follows:

$$\mathbf{A}_{55} \cdot \mathbf{v}_5 = \mathbf{0}_{2 \times 1} = [0 \mid 0]^T \quad (55)$$

$$\mathbf{v}_5 = [v_{O_5x} \mid v_{O_5y} \mid \omega_{5z}]^T \quad (56)$$

$$\mathbf{A}_{55} = \begin{bmatrix} 0 & 1 & 0 \\ 0 & 0 & 1 \end{bmatrix} \quad (57)$$

The elements “1” and “3” are linked to the fix element in O_1 and O_3 points. Therefore their velocities are equal to zero. In mathematical form, the condition for the points O_1 and O_3 to be at rest will be written in matrix form as follows:

$$\mathbf{v}_{O_1} = [v_{O_1x} \mid v_{O_1y}]^T = \mathbf{0}_{2 \times 1} = [0 \mid 0]^T \quad (58)$$

$$\mathbf{v}_{O_3} = [v_{O_3x} \mid v_{O_3y}]^T = \mathbf{0}_{2 \times 1} = [0 \mid 0]^T \quad (59)$$

The matrix relationships (58) and (59) are equivalent to the following scalar relationships:

$$v_{O_1x} = \dot{x}_{O_1} = dx_{O_1}/dt = 0 \quad (60)$$

$$v_{O_1y} = \dot{y}_{O_1} = dy_{O_1}/dt = 0 \quad (61)$$

$$v_{O_3x} = \dot{x}_{O_3} = dx_{O_3}/dt = 0 \quad (62)$$

$$v_{O_3y} = \dot{y}_{O_3} = dy_{O_3}/dt = 0 \quad (63)$$

The relationships (58) and (59) may be written in an equivalent form as follows:

$$\mathbf{A}_{61} \cdot \mathbf{v}_1 = \mathbf{0}_{2 \times 1} = [0 \mid 0]^T \quad (64)$$

$$\mathbf{A}_{63} \cdot \mathbf{v}_3 = \mathbf{0}_{2 \times 1} = [0 \mid 0]^T \quad (65)$$

The expressions of the matrices \mathbf{A}_{61} and \mathbf{A}_{63} are the follows:

$$\mathbf{A}_{61} = \mathbf{A}_{63} = \begin{bmatrix} 1 & 0 & 0 \\ 0 & 1 & 0 \end{bmatrix} \quad (66)$$

The relationships (11), (27), (37), (48), (55), (64) and (65) may be written together in matrix form as follows:

$$\mathbf{A} \cdot \mathbf{v} = \mathbf{0} = \underbrace{\begin{bmatrix} 0 & \dots & 0 \end{bmatrix}}_{1 \times 16}^T \quad (67)$$

In the relationship (67) the quantities that occur have the following expressions:

$$\mathbf{A} = \begin{bmatrix} \mathbf{A}_{11} & \mathbf{A}_{12} & \mathbf{0} & \mathbf{0} & \mathbf{0} \\ \mathbf{0} & \mathbf{A}_{22} & \mathbf{A}_{23} & \mathbf{0} & \mathbf{0} \\ \mathbf{0} & \mathbf{0} & \mathbf{A}_{33} & \mathbf{A}_{34} & \mathbf{0} \\ \mathbf{0} & \mathbf{0} & \mathbf{0} & \mathbf{A}_{44} & \mathbf{A}_{45} \\ \mathbf{0} & \mathbf{0} & \mathbf{0} & \mathbf{0} & \mathbf{A}_{55} \\ \mathbf{A}_{61} & \mathbf{0} & \mathbf{0} & \mathbf{0} & \mathbf{0} \\ \mathbf{0} & \mathbf{0} & \mathbf{A}_{63} & \mathbf{0} & \mathbf{0} \end{bmatrix} \quad (68)$$

$$\mathbf{v} = \begin{bmatrix} \mathbf{v}_1^T & \mathbf{v}_2^T & \mathbf{v}_3^T & \mathbf{v}_4^T & \mathbf{v}_5^T \end{bmatrix}^T \quad (69)$$

In the relationship (68) the mathematical expressions of the matrices $\mathbf{A}_{11}, \mathbf{A}_{12}, \dots, \mathbf{A}_{61}$ are given by the relationships (12), (13), (28), (30), (38), (40), (49), (51), (57) and (66) respectively. The following scalar relationship will be added to the matrix relationship (67):

$$\omega_{1z} = \omega_1 = const. \quad (70)$$

The scalar relationship (70) may also be written in matrix form as follows:

$$\mathbf{B} \cdot \mathbf{v} = \omega_1 = const. \quad (71)$$

In the relationship (71) the matrix \mathbf{B} has the following expression:

$$\mathbf{B}_{1 \times 16} = \begin{bmatrix} 0 & 0 & 1 & 1 & 0 & \dots & 0 & 0 & 0 & 0 & 0 & 0 & 0 & 0 \end{bmatrix} \quad (72)$$

The matrix relationships (67) and (72) may be written together in one single relationship as follows:

$$\mathbf{C} \cdot \mathbf{v} = \mathbf{D} \cdot \omega_1 \quad (73)$$

In the matrix relationship (73) the terms have the following expressions:

$$\mathbf{C} = \begin{bmatrix} \mathbf{A}^T & \mathbf{B}^T \end{bmatrix}^T \quad (74)$$

$$\mathbf{D}_{16 \times 1} = \begin{bmatrix} 0 & 0 & 0 & 0 & 0 & 0 & 0 & 0 & 0 & 0 & 0 & 0 & 0 & 0 & 0 & 1 \end{bmatrix}^T \quad (75)$$

Starting from the relationship (73) in the next chapter we will establish the differential equations that characterize the movement of the mechanism from a cinematic point of view.

3. SETTING THE DIFFERENTIAL EQUATIONS WHICH CHARACTERIZE THE MOVEMENT OF THE SHAPING MECHANISM

In order to determine the differential equations the shaping mechanism from kinematical point of view, we will derive matrix relation (73) twice in relation to time and we will obtain:

$$\mathbf{C} \cdot \dot{\mathbf{v}} + \dot{\mathbf{C}} \cdot \mathbf{v} = \mathbf{0}_{1 \times 16} \quad (76)$$

$$\mathbf{C} \cdot \ddot{\mathbf{v}} + 2 \cdot \dot{\mathbf{C}} \cdot \dot{\mathbf{v}} + \ddot{\mathbf{C}} \cdot \mathbf{v} = \mathbf{0}_{1 \times 16} \quad (77)$$

In the differential equations system written in matrix form (77) the terms that occur have the following expressions:

$$\dot{\mathbf{C}} = [\dot{\mathbf{A}}^T \mid \dot{\mathbf{B}}^T]^T \quad (78)$$

$$\dot{\mathbf{B}} = \underbrace{[0 \mid 0 \mid \dots \mid 0 \mid 0]}_{1 \times 16} \quad (79)$$

$$\dot{\mathbf{A}} = \begin{bmatrix} \dot{\mathbf{A}}_{11} & \dot{\mathbf{A}}_{12} & \mathbf{0} & \mathbf{0} & \mathbf{0} \\ \mathbf{0} & \mathbf{A}_{22} & \mathbf{A}_{23} & \mathbf{0} & \mathbf{0} \\ \mathbf{0} & \mathbf{0} & \mathbf{A}_{33} & \mathbf{A}_{34} & \mathbf{0} \\ \mathbf{0} & \mathbf{0} & \mathbf{0} & \mathbf{A}_{44} & \mathbf{A}_{45} \\ \mathbf{0} & \mathbf{0} & \mathbf{0} & \mathbf{0} & \mathbf{A}_{55} \\ \mathbf{A}_{61} & \mathbf{0} & \mathbf{0} & \mathbf{0} & \mathbf{0} \\ \mathbf{0} & \mathbf{0} & \mathbf{A}_{63} & \mathbf{0} & \mathbf{0} \end{bmatrix} \quad (80)$$

$$\dot{\mathbf{A}}_{11} = \begin{bmatrix} 0 & 0 & -(v_{O_2y} - v_{O_1y}) \\ 0 & 0 & (v_{O_2x} - v_{O_1x}) \end{bmatrix} \quad (81)$$

$$\dot{\mathbf{A}}_{12} = \begin{bmatrix} 0 & 0 & 0 & 0 \\ 0 & 0 & 0 & 0 \end{bmatrix} = \mathbf{0}_{2 \times 4} \quad (82)$$

$$\dot{\mathbf{A}}_{22} = \begin{bmatrix} 0 & 0 & 0 & (1/l_3) \cdot (v_{O_4x} - v_{O_3x}) \\ 0 & 0 & 0 & (1/l_3) \cdot (v_{O_4y} - v_{O_3y}) \\ 0 & 0 & 0 & 0 \end{bmatrix} \quad (83)$$

$$\dot{\mathbf{A}}_{23} = \begin{bmatrix} 0 & 0 & -(v_{O_2y} - v_{O_3y}) \\ 0 & 0 & (v_{O_2x} - v_{O_3x}) \\ 0 & 0 & 0 \end{bmatrix} \quad (84)$$

$$\dot{\mathbf{A}}_{33} = \begin{bmatrix} 0 & 0 & -(v_{O_4y} - v_{O_3y}) \\ 0 & 0 & (v_{O_4x} - v_{O_3x}) \end{bmatrix} \quad (85)$$

$$\dot{\mathbf{A}}_{34} = \begin{bmatrix} 0 & 0 & 0 \\ 0 & 0 & 0 \end{bmatrix} = \mathbf{0}_{2 \times 3} \quad (86)$$

$$\dot{\mathbf{A}}_{44} = \begin{bmatrix} 0 & 0 & -(v_{O_5y} - v_{O_4y}) \\ 0 & 0 & (v_{O_5x} - v_{O_4x}) \end{bmatrix} \quad (87)$$

$$\dot{\mathbf{A}}_{45} = \dot{\mathbf{A}}_{55} = \begin{bmatrix} 0 & 0 & 0 \\ 0 & 0 & 0 \end{bmatrix} = \mathbf{0}_{2 \times 3} \quad (88)$$

$$\dot{\mathbf{A}}_{61} = \dot{\mathbf{A}}_{63} = \begin{bmatrix} 0 & 0 & 0 \\ 0 & 0 & 0 \end{bmatrix} = \mathbf{0}_{2 \times 3} \quad (89)$$

$$\ddot{\mathbf{C}} = [\ddot{\mathbf{A}}^T \mid \ddot{\mathbf{B}}^T]^T \quad (90)$$

$$\ddot{\mathbf{B}} = \underbrace{[0 \mid 0 \mid \dots \mid 0 \mid 0]}_{1 \times 16} \quad (91)$$

$$\ddot{\mathbf{A}} = \begin{bmatrix} \ddot{\mathbf{A}}_{11} & \ddot{\mathbf{A}}_{12} & \mathbf{0} & \mathbf{0} & \mathbf{0} \\ \mathbf{0} & \mathbf{A}_{22} & \mathbf{A}_{23} & \mathbf{0} & \mathbf{0} \\ \mathbf{0} & \mathbf{0} & \mathbf{A}_{33} & \mathbf{A}_{34} & \mathbf{0} \\ \mathbf{0} & \mathbf{0} & \mathbf{0} & \mathbf{A}_{44} & \mathbf{A}_{45} \\ \mathbf{0} & \mathbf{0} & \mathbf{0} & \mathbf{0} & \mathbf{A}_{55} \\ \mathbf{A}_{61} & \mathbf{0} & \mathbf{0} & \mathbf{0} & \mathbf{0} \\ \mathbf{0} & \mathbf{0} & \mathbf{A}_{63} & \mathbf{0} & \mathbf{0} \end{bmatrix} \quad (92)$$

$$\ddot{\mathbf{A}}_{11} = \begin{bmatrix} 0 & 0 & -(a_{O_2y} - a_{O_1y}) \\ 0 & 0 & (a_{O_2x} - a_{O_1x}) \end{bmatrix} \quad (93)$$

$$\ddot{\mathbf{A}}_{12} = \begin{bmatrix} 0 & 0 & 0 & 0 \\ 0 & 0 & 0 & 0 \end{bmatrix} = \mathbf{0}_{2 \times 4} \quad (94)$$

$$\ddot{\mathbf{A}}_{22} = \begin{bmatrix} 0 & 0 & 0 & (1/l_3) \cdot (a_{O_4x} - a_{O_3x}) \\ 0 & 0 & 0 & (1/l_3) \cdot (a_{O_4y} - a_{O_3y}) \\ 0 & 0 & 0 & 0 \end{bmatrix} \quad (95)$$

$$\ddot{\mathbf{A}}_{23} = \begin{bmatrix} 0 & 0 & -(a_{O_2y} - a_{O_3y}) \\ 0 & 0 & (a_{O_2x} - a_{O_3x}) \\ 0 & 0 & 0 \end{bmatrix} \quad (96)$$

$$\ddot{\mathbf{A}}_{33} = \begin{bmatrix} 0 & 0 & -(a_{O_4y} - a_{O_3y}) \\ 0 & 0 & (a_{O_4x} - a_{O_3x}) \end{bmatrix} \quad (97)$$

$$\dot{\mathbf{a}} = \left[\dot{\mathbf{a}}_1^T \mid \dot{\mathbf{a}}_2^T \mid \dot{\mathbf{a}}_3^T \mid \dot{\mathbf{a}}_4^T \mid \dot{\mathbf{a}}_5^T \right]^T \quad (111)$$

$$\ddot{\mathbf{A}}_{34} = \begin{bmatrix} 0 & 0 & 0 \\ 0 & 0 & 0 \end{bmatrix}_{2 \times 3} = \mathbf{0} \quad (98)$$

$$\dot{\mathbf{a}}_1 = [\dot{a}_{O_1x} \quad \dot{a}_{O_1y} \quad \dot{\varepsilon}_{1z}]^T \quad (112)$$

$$\ddot{\mathbf{A}}_{44} = \begin{bmatrix} 0 & 0 & -(a_{O_5y} - a_{O_4y}) \\ 0 & 0 & (a_{O_5x} - a_{O_4x}) \end{bmatrix} \quad (99)$$

$$\dot{\mathbf{a}}_2 = [\dot{a}_{O_2x} \quad \dot{a}_{O_2y} \quad \dot{\varepsilon}_{2z} \quad \dot{a}_{23}]^T \quad (113)$$

$$\ddot{\mathbf{A}}_{45} = \ddot{\mathbf{A}}_{55} = \begin{bmatrix} 0 & 0 & 0 \\ 0 & 0 & 0 \end{bmatrix}_{2 \times 3} = \mathbf{0} \quad (100)$$

$$\dot{\mathbf{a}}_3 = [\dot{a}_{O_3x} \quad \dot{a}_{O_3y} \quad \dot{\varepsilon}_{3z}]^T \quad (114)$$

$$\ddot{\mathbf{A}}_{61} = \ddot{\mathbf{A}}_{63} = \begin{bmatrix} 0 & 0 & 0 \\ 0 & 0 & 0 \end{bmatrix}_{2 \times 3} = \mathbf{0} \quad (101)$$

$$\dot{\mathbf{a}}_4 = [\dot{a}_{O_4x} \quad \dot{a}_{O_4y} \quad \dot{\varepsilon}_{4z}]^T \quad (115)$$

$$\dot{\mathbf{a}}_5 = [\dot{a}_{O_5x} \quad \dot{a}_{O_5y} \quad \dot{\varepsilon}_{5z}]^T \quad (116)$$

$$\dot{\mathbf{v}} = \left[\dot{\mathbf{v}}_1^T \mid \dot{\mathbf{v}}_2^T \mid \dot{\mathbf{v}}_3^T \mid \dot{\mathbf{v}}_4^T \mid \dot{\mathbf{v}}_5^T \right]^T = \mathbf{a} \quad (102)$$

The system of the second order differential equations (77) will be transformed into a system of differential equations of the first order. For this, the following notation will be introduced:

$$\mathbf{a} = \left[\mathbf{a}_1^T \mid \mathbf{a}_2^T \mid \mathbf{a}_3^T \mid \mathbf{a}_4^T \mid \mathbf{a}_5^T \right]^T \quad (103)$$

$$\dot{\mathbf{v}} = \mathbf{a} \quad (117)$$

$$\mathbf{a}_1 = [a_{O_1x} \quad a_{O_1y} \quad \varepsilon_{1z}]^T \quad (104)$$

By replacing the relation (117) the relation (77) into the matrix relation (77) we will obtain:

$$\mathbf{a}_2 = [a_{O_2x} \quad a_{O_2y} \quad \varepsilon_{2z} \quad a_{23}]^T \quad (105)$$

$$\mathbf{C} \cdot \dot{\mathbf{a}} + 2 \cdot \dot{\mathbf{C}} \cdot \mathbf{a} + \ddot{\mathbf{C}} \cdot \mathbf{v} = \mathbf{0}_{1 \times 16} \quad (118)$$

$$a_{23} = \dot{v}_{23} \quad (106)$$

$$\mathbf{a}_3 = [a_{O_3x} \quad a_{O_3y} \quad \varepsilon_{3z}]^T \quad (107)$$

The matrix relations (117) and (118) form together a system of thirty two differential equations of the first order. In order to perform a complete kinematical study namely to determine the variation of the positional kinematical parameters in relation to time, the following matrix relation will be added to the relationships (117) and (118):

$$\mathbf{a}_4 = [a_{O_4x} \quad a_{O_4y} \quad \varepsilon_{4z}]^T \quad (108)$$

$$\dot{\mathbf{x}} = \mathbf{v} \quad (119)$$

$$\mathbf{a}_5 = [a_{O_5x} \quad a_{O_5y} \quad \varepsilon_{5z}]^T \quad (109)$$

In the relationship (119) the column matrix $\dot{\mathbf{x}}$ will be written as follows:

$$\ddot{\mathbf{v}} = \left[\ddot{\mathbf{v}}_1^T \mid \ddot{\mathbf{v}}_2^T \mid \ddot{\mathbf{v}}_3^T \mid \ddot{\mathbf{v}}_4^T \mid \ddot{\mathbf{v}}_5^T \right]^T = \dot{\mathbf{a}} \quad (110)$$

$$\dot{\mathbf{x}} = \left[\dot{x}_1^T \mid \dot{x}_2^T \mid \dot{x}_3^T \mid \dot{x}_4^T \mid \dot{x}_5^T \right]^T \quad (120)$$

$$\dot{\mathbf{x}}_1 = [\dot{x}_{O_1} \mid \dot{y}_{O_1} \mid \dot{\phi}_{1z}]^T \quad (121)$$

$$x_{O_1}^0 = 0 [meters] \quad (132)$$

$$\dot{\mathbf{x}}_2 = [\dot{x}_{O_2} \mid \dot{y}_{O_2} \mid \dot{\phi}_{2z} \mid \dot{s}_{23}]^T \quad (122)$$

$$y_{O_1}^0 = 4 [meters] \quad (133)$$

$$\dot{\mathbf{x}}_3 = [\dot{x}_{O_3} \mid \dot{y}_{O_3} \mid \dot{\phi}_{3z}]^T \quad (123)$$

$$\phi_1^0 = 0 [radians] \quad (134)$$

$$\dot{\mathbf{x}}_4 = [\dot{x}_{O_4} \mid \dot{y}_{O_4} \mid \dot{\phi}_{4z}]^T \quad (124)$$

$$x_{O_2}^0 = 1 [meters] \quad (135)$$

$$\dot{\mathbf{x}}_5 = [\dot{x}_{O_5} \mid \dot{y}_{O_5} \mid \dot{\phi}_{5z}]^T \quad (125)$$

$$y_{O_2}^0 = 4 [meters] \quad (136)$$

The matrix relationships (117), (118) and (119) form together a system with forty eight differential equations with forty eight unknowns.

$$\phi_2^0 = 1.32582 [radians] \quad (137)$$

4. INTEGRATION OF THE DIFFERENTIAL EQUATIONS SYSTEM AND THE RESULTS DETERMINATION

$$s_{23}^0 = 4.123 [meters] \quad (138)$$

The differential equations system expressed by the matrix relationships (117), (118) and (119) will be integrated using numerical integration methods. In order to do this, using MATLAB software, a computational program that integrates the system of differential equations mentioned above was designed. The following input data are required in order to run the program.

$$x_{O_3}^0 = 0 [meters] \quad (139)$$

$$y_{O_3}^0 = 0 [meters] \quad (140)$$

$$\phi_3^0 = 1.32582 [radians] \quad (141)$$

$$l_1 = 1 [meters] \quad (126)$$

$$x_{O_4}^0 = l_3 \cdot \cos \phi_3^0 = 1.455 [meters] \quad (142)$$

$$l_3 = 6 [meters] \quad (127)$$

$$y_{O_4}^0 = l_3 \cdot \sin \phi_3^0 = 5.821 [meters] \quad (143)$$

$$l_4 = 1.5 [meters] \quad (128)$$

$$\phi_4^0 = 2.2371 [radians] \quad (144)$$

$$l_0' = 3 [meters] \quad (129)$$

$$l_0 = 4 [meters] \quad (130)$$

$$x_{O_5}^0 = l_3 \cdot \cos \phi_3^0 + l_4 \cdot \cos \phi_4^0 = 0.528 [meters] \quad (145)$$

$$\omega_1 = 10 [radians / sec.] = const. \quad (131)$$

$$y_{O_5}^0 = l_3 \cdot \sin \phi_3^0 + l_4 \cdot \sin \phi_4^0 = 7 [meters] \quad (146)$$

The following initial conditions are also required:

$$\varphi_5^0 = 0 [\text{radians}] \quad (147) \quad \omega_{5z}^0 = 0 [\text{radians / sec.}] \quad (163)$$

$$v_{O_1x}^0 = 0 [\text{meters / sec.}] \quad (148) \quad a_{O_1x}^0 = 0 [\text{meters / sec}^2] \quad (164)$$

$$v_{O_1y}^0 = 0 [\text{meters / sec.}] \quad (149) \quad a_{O_1y}^0 = 0 [\text{meters / sec}^2] \quad (165)$$

$$\omega_{1z}^0 = 10 [\text{radians / sec.}] \quad (150) \quad \varepsilon_{1z}^0 = 0 [\text{radians / sec}^2] \quad (166)$$

$$v_{O_2x}^0 = 0 [\text{meters / sec.}] \quad (151) \quad a_{O_2x}^0 = -100 [\text{meters / sec}^2] \quad (167)$$

$$v_{O_2y}^0 = 10 [\text{meters / sec.}] \quad (152) \quad a_{O_2y}^0 = 0 [\text{meters / sec}^2] \quad (168)$$

$$\omega_{2z}^0 = 0.588 [\text{radians / sec.}] \quad (153) \quad \varepsilon_{2z}^0 = 20.761 [\text{radians / sec}^2] \quad (169)$$

$$v_{23}^0 = 9.7014 [\text{meters / sec.}] \quad (154) \quad a_{23}^0 = -22.827 [\text{meters / sec}^2] \quad (170)$$

$$v_{O_3x}^0 = 0 [\text{meters / sec.}] \quad (155) \quad a_{O_3x}^0 = 0 [\text{meters / sec}^2] \quad (171)$$

$$v_{O_3y}^0 = 0 [\text{meters / sec.}] \quad (156) \quad a_{O_3y}^0 = 0 [\text{meters / sec}^2] \quad (172)$$

$$\omega_{3z}^0 = 0.588 [\text{radians / sec.}] \quad (157) \quad \varepsilon_{3z}^0 = 20.761 [\text{radians / sec}^2] \quad (173)$$

$$v_{O_4x}^0 = -3.424 [\text{meters / sec.}] \quad (158) \quad a_{O_4x}^0 = -121.352 [\text{meters / sec}^2] \quad (174)$$

$$v_{O_4y}^0 = 0.856 [\text{meters / sec.}] \quad (159) \quad a_{O_4y}^0 = 28.198 [\text{meters / sec}^2] \quad (175)$$

$$\omega_{4z}^0 = 0.923 [\text{radians / sec.}] \quad (160) \quad \varepsilon_{4z}^0 = 29.3293 [\text{radians / sec}^2] \quad (176)$$

$$v_{O_5x}^0 = -4.513 [\text{meters / sec.}] \quad (161) \quad a_{O_5x}^0 = -155.145 [\text{meters / sec}^2] \quad (177)$$

$$v_{O_5y}^0 = 0 [\text{meters / sec.}] \quad (162) \quad a_{O_5y}^0 = 0 [\text{meters / sec}^2] \quad (178)$$

$$\varepsilon_{s_z}^0 = 0 \text{ [radians / sec}^2\text{]} \quad (179)$$

Following integration, the results presented in the figures below (Fig.2-Fig.6) are obtained.

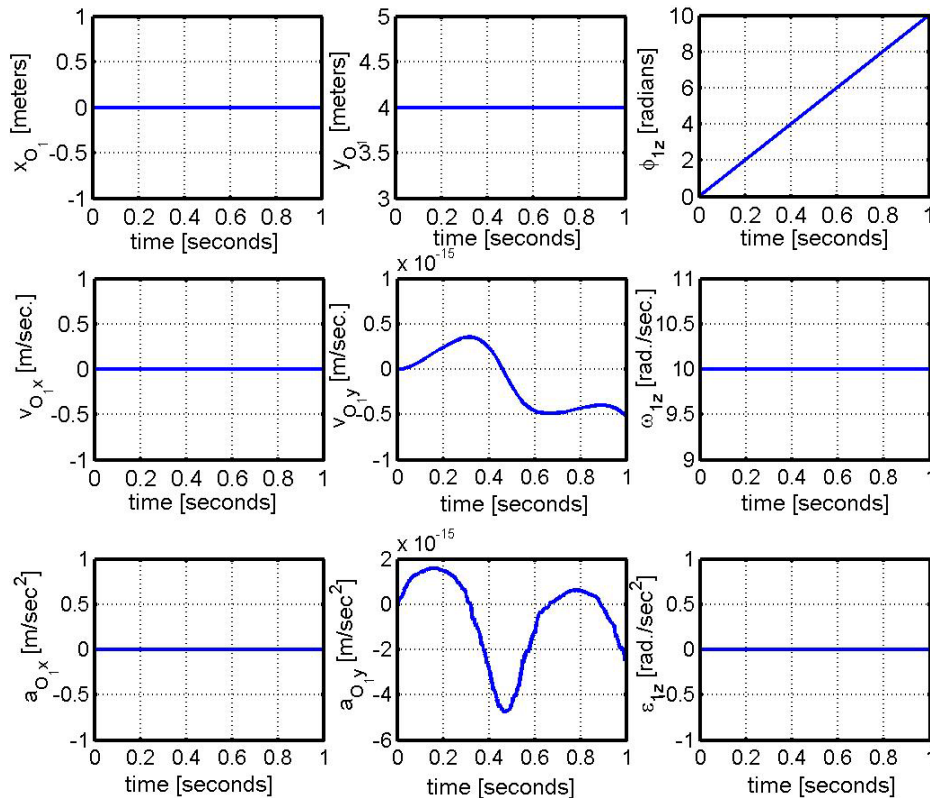


Figure 2.Variation of the kinematical parameters of the"1"element with respect to time

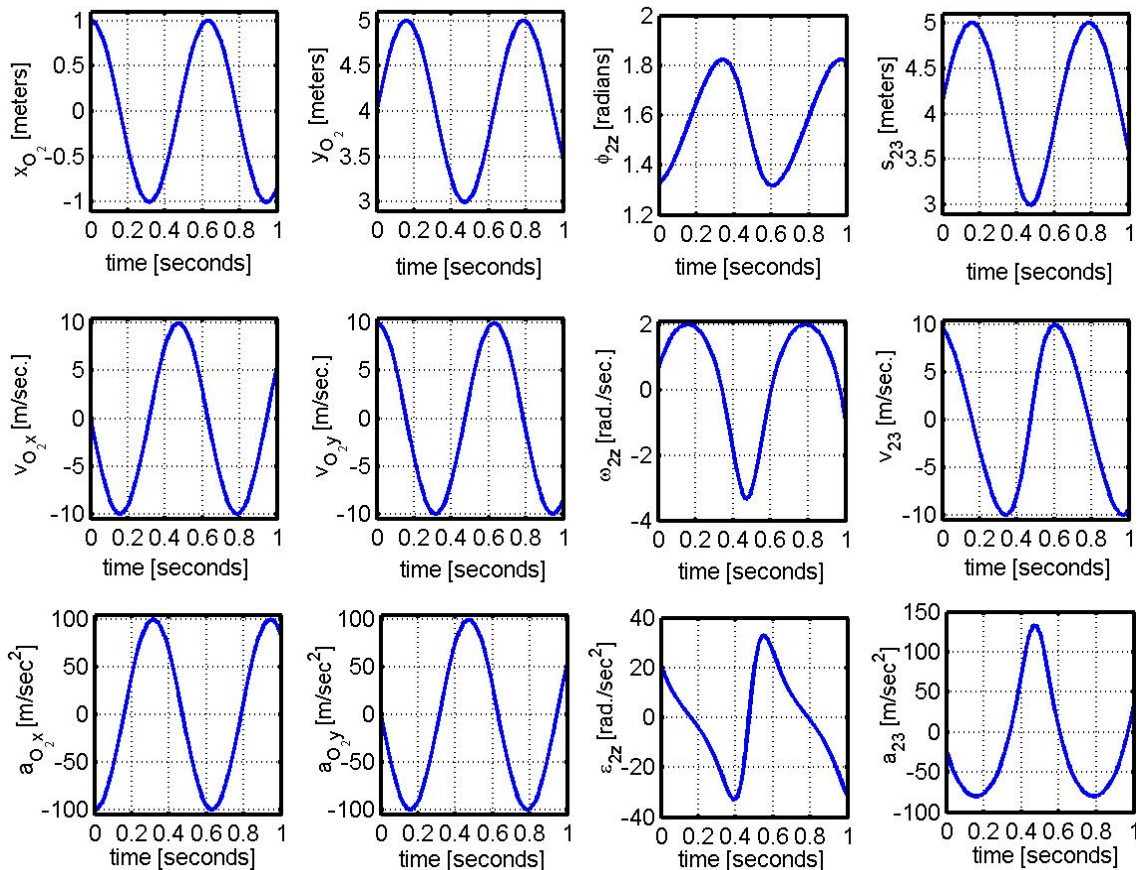


Figure 3.Variation of the kinematical parameters of the"2"element with respect to time

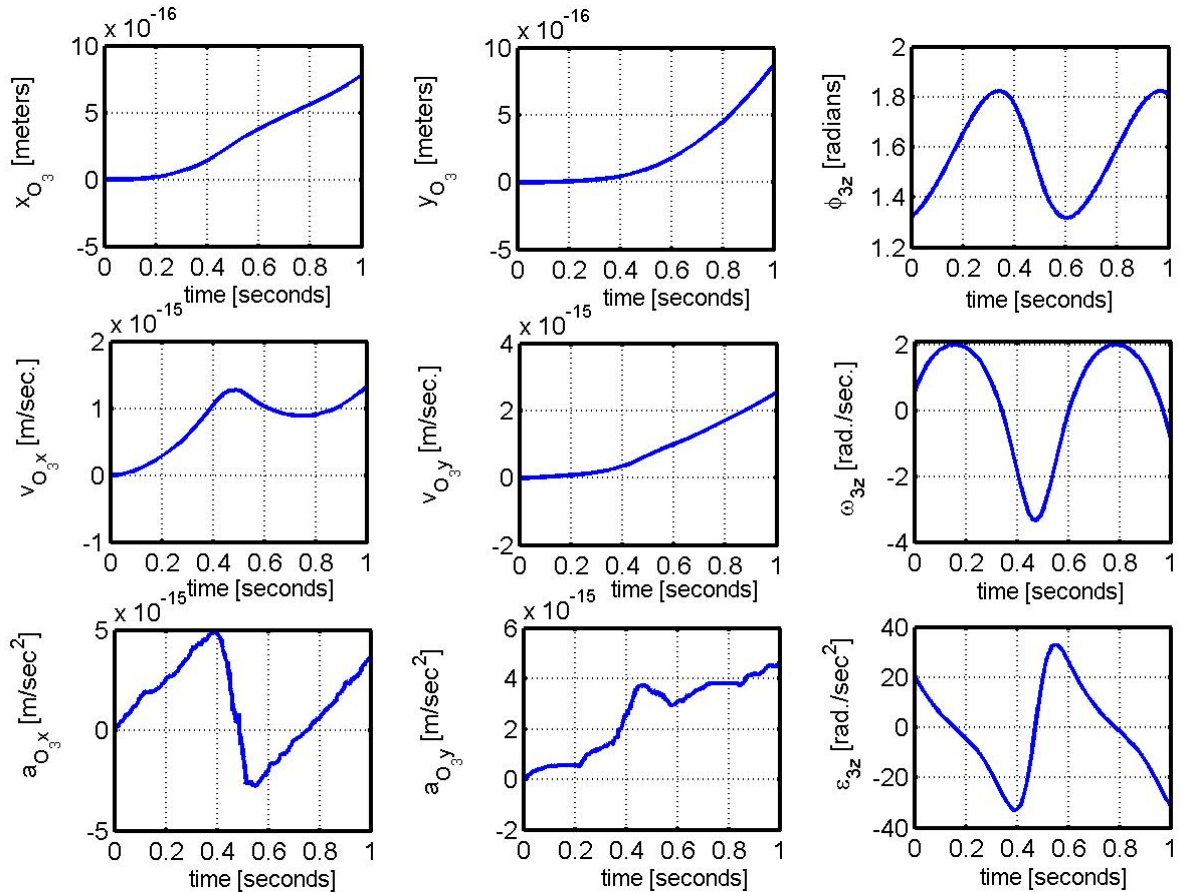


Figure 4. Variation of the kinematical parameters of the "3" element with respect to time

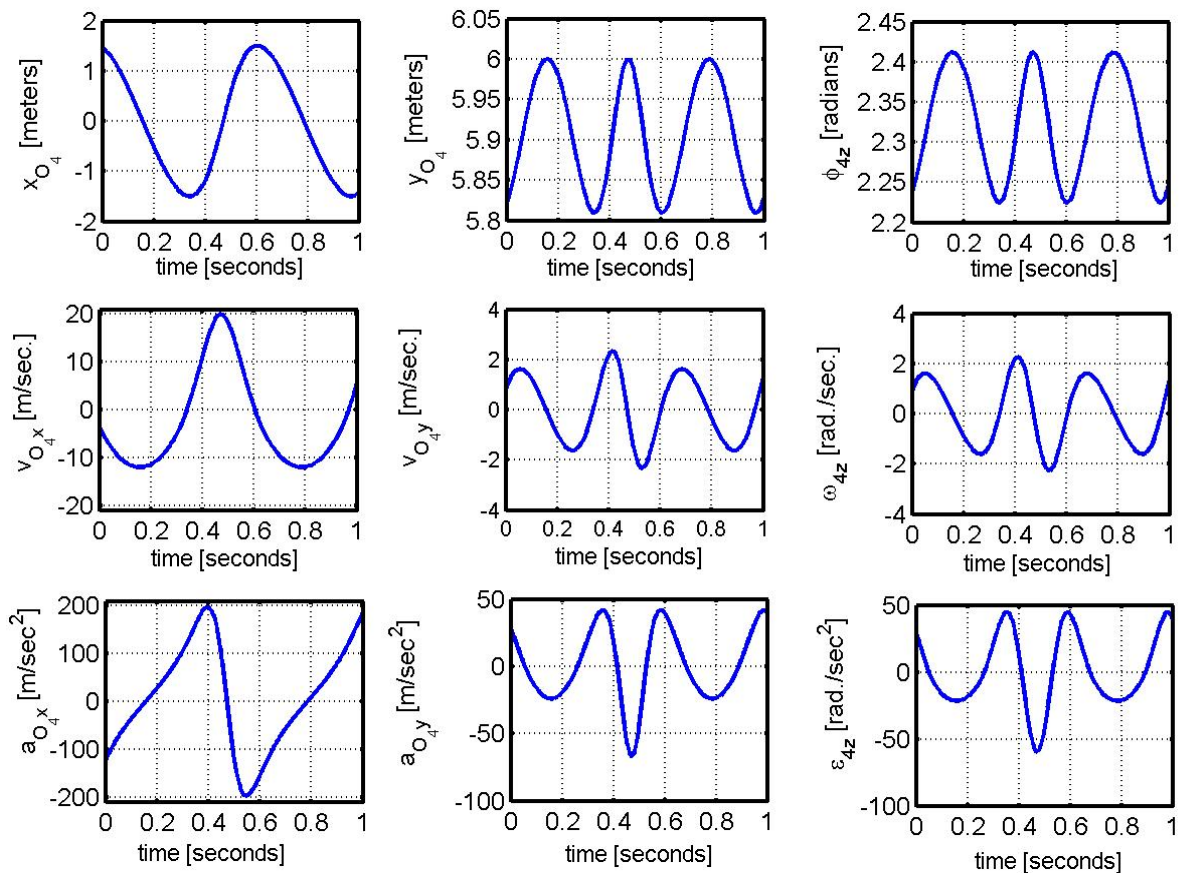


Figure 5. Variation of the kinematical parameters of the "4" element with respect to time

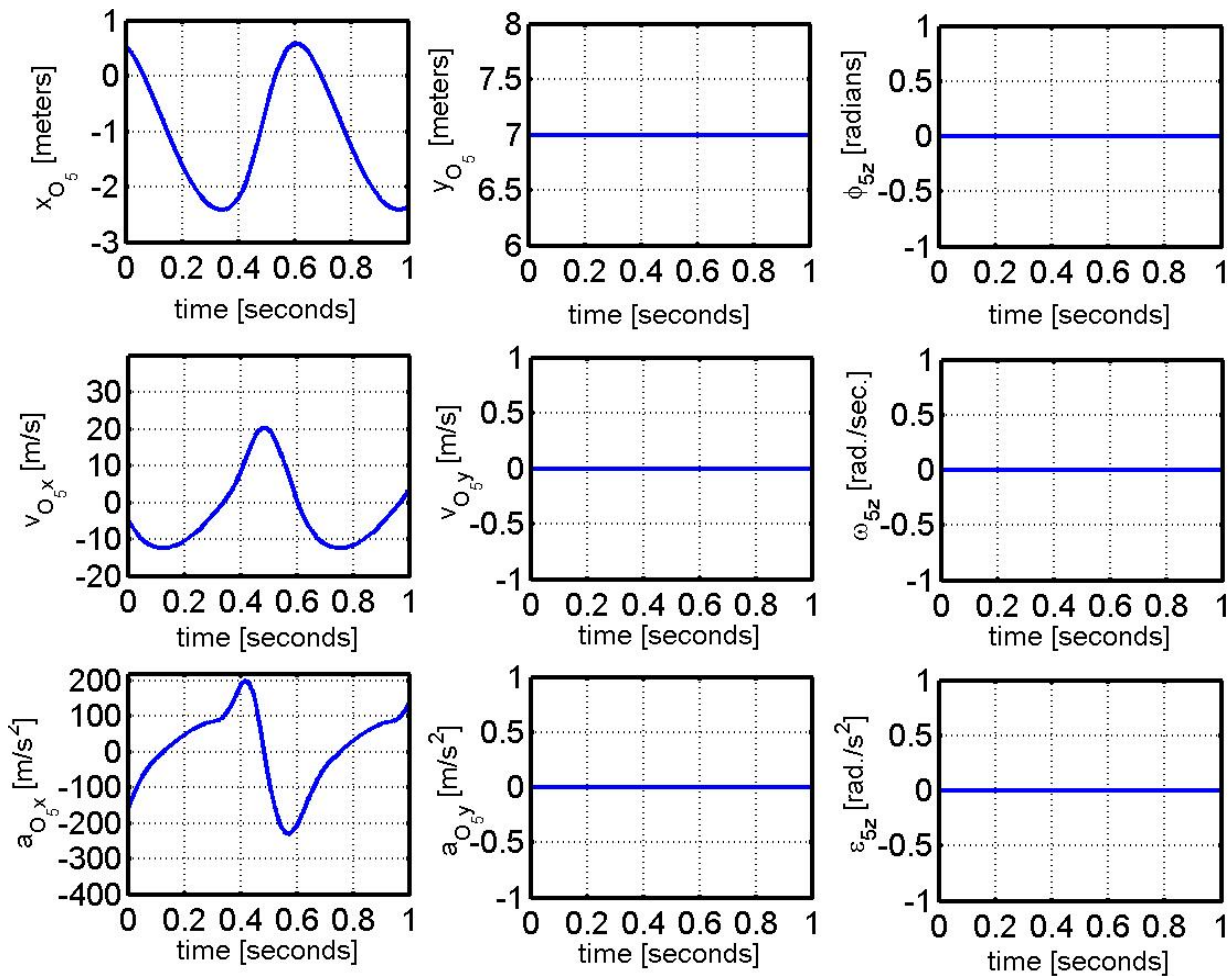


Figure 6. Variation of the kinematical parameters of the "5" element with respect to time

The movement was studied for a period of time of a second. It was considered that the leading element of the mechanism describes a uniform rotation movement all the time of the motion.

5. CONCLUSIONS

The numerical method presented in the paper is based on Euler's relations concerning the distribution of velocities written in projections on the fixed reference system axes. Using the numerical method shown in the paper one can determine the variation in relation to the time of displacement, velocity and acceleration of any point belonging to any element of the mechanism.

REFERENCES

- [1] Vălcovici V., Bălan V., Voinea R., Mecanica Teoretică, Editura Tehnică, București, 1968
- [2] Viorel Handra Luca, Ion Aurel Stoica, Introducere in teoria mecanismelor, vol.I, pp.84, Editura Dacia Cluj-Napoca 1982
- [3] Christian Pelecudi, Dezideriu Maroș, Vasile Merticaru, Nicolae Pandrea, Ion Simionescu, Mecanisme, pp.206-208, Editura Tehnică, 1983
- [4] Voinea R., Stroe I., A general method for kinematics pairs synthesis, Mechanism and Machine Theory, Elsevier, 30(3), pp. 461-470, 1995
- [5] Ștefan Staicu, Mecanica Teoretică.,Editura Didactică și Pedagogică București R.A., 1998
- [6] Florin Bașic, Mecanica Teoretică.Cinematica, Editura Conspress, București, 2004
- [7] Staicu S., Kinematics of translation-rotation parallel robot, Romanian Journal of Technical Sciences-Applied Mechanics, 60, pp. 171-183, 2015

UNFOLDINGS OF THE INTERSECTED SURFACES

Carmen POPA¹, Violeta ANGHELINA¹, Ruxandra-Elena BRATU²

¹ Valahia University Targoviste, Romania, ² Politehnica University of Bucharest

E-mail: carmenpopa2001@yahoo.com

Abstract: The paper proposes to establish the intersection curve and the unfoldings of three cylinders. The intersection of the curves was determined by the classical method, using the AutoCAD program, and the unfolded surfaces were realized by analytical methods. For this the Mathematica program was used.

Keywords: unfolding, coupling, Mathematica program

1. INTRODUCTION

The design of the unfoldings comprises the following phases:

- writing the equations of the curves resulting at the intersections of the surfaces;
- writing the equations of the transforms by unfolding the intersection curves.

2. CONTENTS

The Ox and Oz axes are considered, for the vertical projection and Ox_d and Oy_d as axes for the unfolding of the cylinder. The transformation of the equation of the vertical projection of a curve drawn on the cylinder into the equation of the unfolded curve can be done by expressing the x and z coordinates depending on x_d and x_d [1-3].

$$ab = x_d = r \cdot \alpha \rightarrow \alpha = \frac{x_d}{r} \quad (1)$$

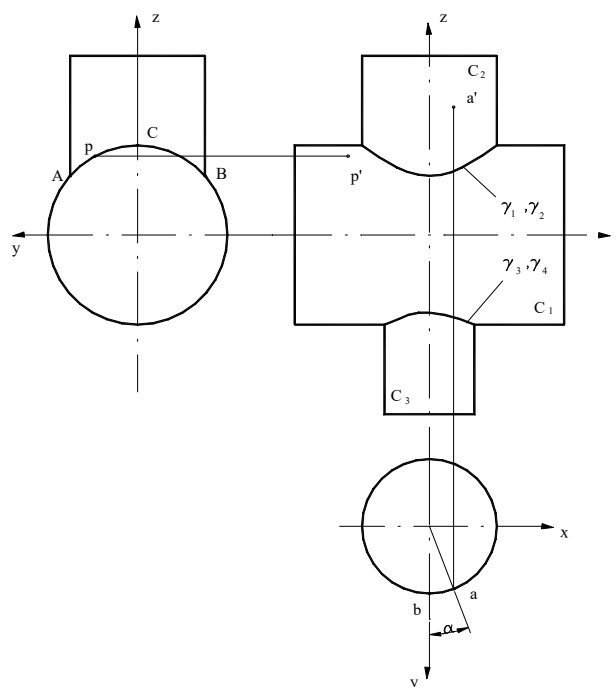


Figure 1. Design of the cylinders

$$\sin \alpha = \frac{x}{r} \rightarrow x = r \cdot \sin \alpha \quad (2)$$

$$x = r \cdot \sin \frac{x_d}{r} \quad (3)$$

$$z = z_d$$

To find out the γ_1 curve unfolding of the C_1 cylinder we take the C_1 and C_2 cylinders, whose equations are:

$$C_1 : z^2 + y^2 = R_1^2, \quad (4)$$

$$C_{22} : y^2 + x^2 = R_2^2. \quad (5)$$

By eliminating the y variable, we obtain the equation of the vertical projection:

$$z^2 - x^2 - R_1^2 + R_2^2 = 0. \quad (6)$$

The equation of the plane curve, boundary of the unfolding of the C_2 cylinder, is obtained by applying the (3) relations to the (6) equation:

In this case the equation will be:

$$R_2^2 \sin^2 x_d / R_2 - z_d^2 + R_1^2 - R_2^2 = 0. \quad (7)$$

$$\text{Then: } z_d = \pm \sqrt{R_1^2 - R_2^2 \cos^2 \frac{x_d}{R_2}} \quad (8)$$

$$\text{where: } x_d \in [-\pi R_2, \pi R_2]. \quad (9)$$

The 2 figure shows the unfolding of the intersection curve for the C_2 cylinder.

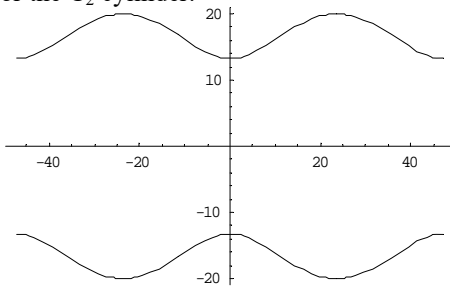


Figure 2. Unfolding of the γ_1 curve of the C_2 cylinder

The equation of the plane curve, γ_1 , boundary of the unfolding of the C_1 cylinder to the C_2 cylinder, is obtained by applying the relations:

$$x = x_d, \quad (10)$$

$$z = R_1 \cos z_d / R_1,$$

In this case the (6) equation will be:

$$x_d^2 - R_1^2 \cos^2 z_d / R_1 - R_1^2 + R_2^2 = 0 \quad (11)$$

$$\text{Then: } x_d = \pm \sqrt{R_2^2 - R_1^2 \sin^2 \frac{z_d}{R_1}} \quad (12)$$

$$\text{where: } z_d \in [AC, BC], \quad (13)$$

$$\text{so: } z_d \in [-R_1 \arcsin R_2 / R_1, R_1 \arcsin R_2 / R_1] \quad (14)$$

The drawing of the curves in the program Mathematica takes place as in the 3 figure.

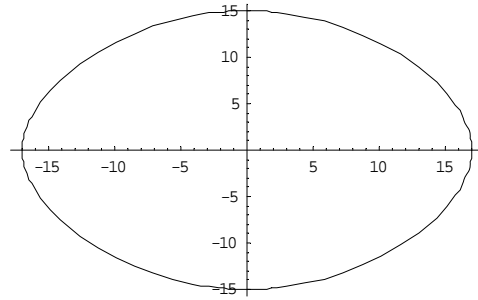


Figure 3. Unfolding of the γ_2 curve of the C_1 cylinder

The equation of the plane curve, γ_3 , boundary of the C_1 and C_3 cylinders, but belonging to the C_1 cylinder, is obtained by replacing the concrete data in the (12) and (14) equations. In this case we get the 4 figure.

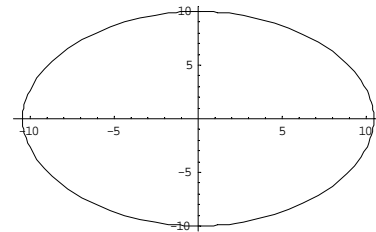


Figure 4. Unfolding of the γ_3 curve of the C_1 cylinder

The equation of the γ_4 curve, boundary of the C_3 cylinder is obtained by replacing the cylinder data in the (8) and (9) equations. In the latter case we obtain the 5 figure.

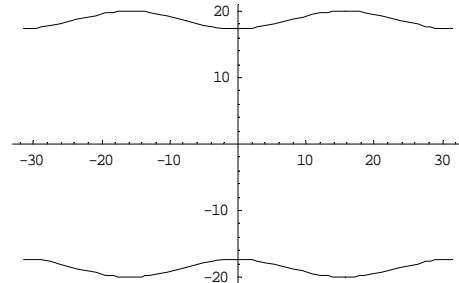


Figure 5. Unfolding of the γ_4 curve of the C_3 cylinder

3. CONCLUSIONS

The presented method is very speedy and exactly and following the program we can obtain the unfoldings of cylinders for any other dimensions.

REFERENCES

- [1] Vlasov, A. K.: Curs de matematică superioară, Editura Tehnică, Timișoara, 1971;
- [2] Popa, Carmen, Petre, Ivona: Mathematical methods to determinate the intersection curves of the cylinders, International Conference on Manufacturing Systems ICMS, București, 2004, tome 49, p. 595, ISBN 973-27-1102-7, ISSN 0035-4074
- [3] Popa, Carmen: Mathematical method to unfold an oblique pyramid, Modelling and optimization in the machines building field, Bacau, 2004, vol I, 40.

NUMERICAL KINEMATICAL ANALYSIS OF THE ARTICULATED QUADRILATERAL MECHANISM

Mircea Bogdan TĂTARU¹, Vladimir Dragoş TĂTARU²

¹ University of Oradea, ² University “Valahia” of Târgovişte

E-mail: btataru@uoradea.ro, vdtataru@gmail.com

Abstract: *The paper presents a numerical method of kinematical analysis of the articulated quadrilateral mechanism. Starting from Euler’s relation concerning the distribution of speeds written in projections on the fixed reference system axes, a system of differential equations describing the movement of the mechanism was obtained. This system of differential equations was then solved using numerical integration methods and the variation with respect to time of the position kinematical parameters, of the velocities (the first order kinematical parameters), and of the accelerations (the second order kinematical parameters), was obtained. Matrix writing of the differential equations was used in order to make the differential equations set out in the paper easier to solve using the electronic computer.*

Keywords: *kinematical analysis, numerical method, numerical integration methods, quadrilateral mechanism, leading element*

NOMENCLATURE

$T(Oxyz)$ -fixed reference frame

x_{O_1}, y_{O_1} - O_1 point coordinates relative to the $T(Oxyz)$

v_{O_1x}, v_{O_1y} -projections of the O_1 point velocities on the axes of the fixed reference frame $T(Oxyz)$

a_{O_1x}, a_{O_1y} -projections of the O_1 point accelerations on the axes of the fixed reference frame $T(Oxyz)$

x_{O_2}, y_{O_2} - O_2 point coordinates relative to the $T(Oxyz)$

v_{O_2x}, v_{O_2y} -projections of the O_2 point velocities on the axes of the fixed reference frame $T(Oxyz)$

a_{O_2x}, a_{O_2y} -projections of the O_2 point accelerations on the axes of the fixed reference frame $T(Oxyz)$

x_{O_3}, y_{O_3} - O_3 point coordinates relative to the $T(Oxyz)$

v_{O_3x}, v_{O_3y} -projections of the O_3 point velocities on the axes of the fixed reference frame $T(Oxyz)$

a_{O_3x}, a_{O_3y} -projections of the O_3 point accelerations on the axes of the fixed reference frame $T(Oxyz)$

x_{O_4}, y_{O_4} - O_4 point coordinates relative to the $T(Oxyz)$

v_{O_4x}, v_{O_4y} -projections of the O_4 point velocities on the axes of the fixed reference frame $T(Oxyz)$

a_{O_4x}, a_{O_4y} -projections of the O_4 point accelerations on the axes of the fixed reference system $T(Oxyz)$

l_1, l_2, l_3 -lengths of the elements 1, 2 and 3 respectively

$\varphi_{1z}, \varphi_{2z}, \varphi_{3z}$ -self-rotation angles of the elements 1, 2 and 3 respectively

$\omega_{1z}, \omega_{2z}, \omega_{3z}$ -angular velocities of the elements 1, 2 and 3 respectively

$\varepsilon_{1z}, \varepsilon_{2z}, \varepsilon_{3z}$ -angular accelerations of the elements 1, 2 and 3 respectively

T -exponent that indicates the transposition matrix operation

1. INTRODUCTION

The articulated quadrilateral mechanism presented in the figure below (Fig.1) will be taken into consideration. It consists of three mobile elements. The leading element is denoted by “1”. The three mobile elements are connected each other and to the fixed element by cylindrical joints. The mechanism is presented in a configuration corresponding to a certain moment “ t ”. The mechanism in discussion may be regarded as a mechanical system having one degree of freedom.

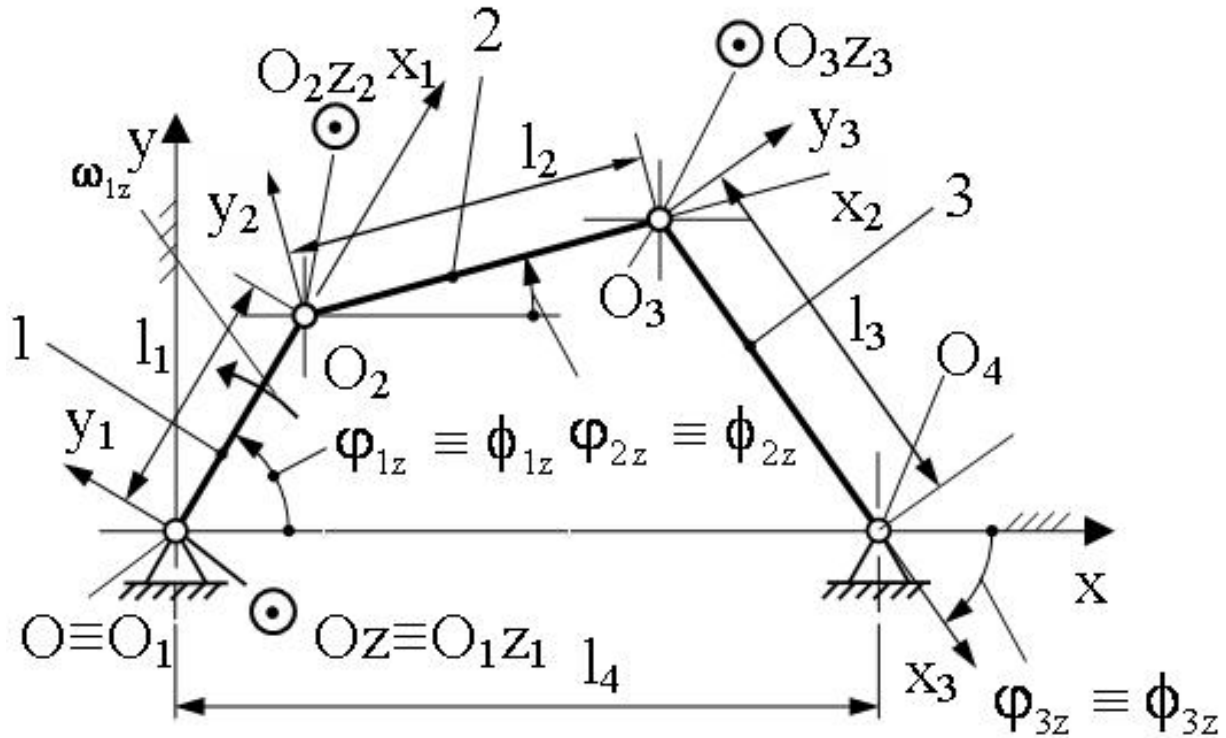


Figure 1. Articulated quadrilateral mechanism [2]

In [2], an analytical method of the positional kinematical analysis was presented while in [8] an incremental numerical method with the aid of which the position of the mechanism can be determined for each moment of the movement. Further on, we intend to perform the complete cinematic analysis of the articulated quadrilateral mechanism.

In matrix form the vector relationship (2) may be written like this:

$$\mathbf{v}_{O_1} + \tilde{\omega}_1 \cdot (\mathbf{r}_{O_2} - \mathbf{r}_{O_1}) - \mathbf{v}_{O_2} = \mathbf{0} = [0 \ 0]^T \quad (3)$$

2. ESTABLISHING THE RELATIONSHIPS BETWEEN THE FIRST ORDER KINEMATICAL PARAMETERS

Taking into account Euler's relation concerning the velocities distribution, between the O_1 point velocity and the O_2 point velocity, regarded as points belonging to the same solid rigid body, the following vector relationship in projections on the fixed reference system axes $T(Oxyz)$ may be written:

$$\vec{v}_{O_1} + \vec{\omega}_1 \times \vec{O_1O_2} - \vec{v}_{O_2} = \vec{0} \quad (1)$$

The vector relationship (1) may be written in the following equivalent form:

$$\vec{v}_{O_1} + \vec{\omega}_1 \times (\mathbf{r}_{O_2} - \mathbf{r}_{O_1}) - \mathbf{v}_{O_2} = \vec{0} \quad (2)$$

$$\mathbf{v}_{O_1} = [v_{O_1,x} \ | \ v_{O_1,y}]^T \quad (4)$$

$$\tilde{\omega}_1 = \begin{bmatrix} 0 & -\omega_{1z} \\ \omega_{1z} & 0 \end{bmatrix} \quad (5)$$

$$\mathbf{r}_{O_1} = [x_{O_1} \ | \ y_{O_1}]^T \quad (6)$$

$$\mathbf{r}_{O_2} = [x_{O_2} \ | \ y_{O_2}]^T \quad (7)$$

$$\mathbf{v}_{O_2} = [v_{O_2,x} \ | \ v_{O_2,y}]^T \quad (8)$$

The matrix relationship (3) is equivalent with the following two scalar relationships:

$$v_{O_1,x} - \omega_{1z} \cdot (y_{O_2} - y_{O_1}) - v_{O_2,x} = 0 \quad (9)$$

$$v_{O_1y} + \omega_{1z} \cdot (x_{O_2} - x_{O_1}) - v_{O_2y} = 0 \quad (10)$$

The scalar relationships (9) and (10) may be written together in matrix form as follows:

$$\mathbf{A}_{11} \cdot \mathbf{v}_1 + \mathbf{A}_{12} \cdot \mathbf{v}_2 = \underset{2 \times 1}{\mathbf{0}} = [0 \mid 0]^T \quad (11)$$

$$\mathbf{A}_{11} = \begin{bmatrix} 1 & 0 & -(y_{O_2} - y_{O_1}) \\ 0 & 1 & (x_{O_2} - x_{O_1}) \end{bmatrix} \quad (12)$$

$$\mathbf{A}_{12} = \begin{bmatrix} -1 & 0 \\ 0 & -1 \end{bmatrix} \quad (13)$$

$$\mathbf{v}_1 = [v_{O_1x} \mid v_{O_1y} \mid \omega_{1z}]^T \quad (14)$$

$$\mathbf{v}_2 = [v_{O_2x} \mid v_{O_2y} \mid \omega_{2z}]^T \quad (15)$$

Between the speed of O_2 point and the speed of O_3 point, regarded as points belonging to the same solid rigid body “2” the following matrix relationship may be written:

$$\mathbf{v}_{O_2} + \tilde{\boldsymbol{\omega}}_2 \cdot (\mathbf{r}_{O_3} - \mathbf{r}_{O_2}) - \mathbf{v}_{O_3} = \underset{2 \times 1}{\mathbf{0}} = [0 \mid 0]^T \quad (16)$$

$$\mathbf{v}_{O_2} = [v_{O_2x} \mid v_{O_2y}]^T \quad (17)$$

$$\mathbf{r}_{O_3} = [x_{O_3} \mid y_{O_3}]^T \quad (18)$$

$$\mathbf{v}_{O_3} = [v_{O_3x} \mid v_{O_3y}]^T \quad (19)$$

$$\tilde{\boldsymbol{\omega}}_2 = \begin{bmatrix} 0 & -\omega_{2z} \\ \omega_{2z} & 0 \end{bmatrix} \quad (20)$$

The matrix relationship (16) is equivalent with the following two scalar relationships:

$$v_{O_2x} - \omega_{2z} \cdot (y_{O_3} - y_{O_2}) - v_{O_3x} = 0 \quad (21)$$

$$v_{O_2y} + \omega_{2z} \cdot (x_{O_3} - x_{O_2}) - v_{O_3y} = 0 \quad (22)$$

The scalar relationships (21) and (22) may be written together in matrix form as follows:

$$\mathbf{A}_{22} \cdot \mathbf{v}_2 + \mathbf{A}_{23} \cdot \mathbf{v}_3 = \underset{2 \times 1}{\mathbf{0}} = [0 \mid 0]^T \quad (23)$$

$$\mathbf{A}_{22} = \begin{bmatrix} 1 & 0 & -(y_{O_3} - y_{O_2}) \\ 0 & 1 & (x_{O_3} - x_{O_2}) \end{bmatrix} \quad (24)$$

$$\mathbf{v}_2 = [v_{O_2x} \mid v_{O_2y} \mid \omega_{2z}]^T \quad (25)$$

$$\mathbf{A}_{23} = \begin{bmatrix} -1 & 0 \\ 0 & -1 \end{bmatrix} \quad (26)$$

$$\mathbf{v}_3 = [v_{O_3x} \mid v_{O_3y} \mid \omega_{3z}]^T \quad (27)$$

Between the speed of O_3 point and the speed of O_4 point, regarded as points belonging to the same solid rigid body “3” the following relationship in matrix form may be written:

$$\mathbf{v}_{O_3} + \tilde{\boldsymbol{\omega}}_3 \cdot (\mathbf{r}_{O_4} - \mathbf{r}_{O_3}) - \mathbf{v}_{O_4} = \underset{2 \times 1}{\mathbf{0}} = [0 \mid 0]^T \quad (28)$$

$$\mathbf{v}_{O_3} = [v_{O_3x} \mid v_{O_3y}]^T \quad (29)$$

$$\tilde{\boldsymbol{\omega}}_3 = \begin{bmatrix} 0 & -\omega_{3z} \\ \omega_{3z} & 0 \end{bmatrix} \quad (30)$$

$$\mathbf{r}_{O_3} = [x_{O_3} \mid y_{O_3}]^T \quad (31)$$

$$\mathbf{r}_{O_4} = [x_{O_4} \mid y_{O_4}]^T \quad (32)$$

$$\mathbf{v}_{O_4} = [v_{O_4x} \mid v_{O_4y}]^T \quad (33)$$

$$v_{O_1x} = \dot{x}_{O_1} = dx_{O_1}/dt = 0 \quad (43)$$

The matrix relationship (28) is equivalent with the following two scalar relationships:

$$v_{O_1y} = \dot{y}_{O_1} = dy_{O_1}/dt = 0 \quad (44)$$

$$v_{O_3x} - \omega_{3z} \cdot (y_{O_4} - y_{O_3}) - v_{O_4x} = 0 \quad (34)$$

$$v_{O_4x} = \dot{x}_{O_4} = dx_{O_4}/dt = 0 \quad (45)$$

$$v_{O_3y} + \omega_{3z} \cdot (x_{O_4} - x_{O_3}) - v_{O_4y} = 0 \quad (35)$$

$$v_{O_4y} = \dot{y}_{O_4} = dy_{O_4}/dt = 0 \quad (46)$$

The scalar relationships (34) and (35) may be written together in matrix form as follows:

The relationships (41) and (42) may be written in an equivalent matrix form as follows:

$$\mathbf{A}_{33} \cdot \mathbf{v}_3 + \mathbf{A}_{34} \cdot \mathbf{v}_4 = \mathbf{0} = [0 \mid 0]^T \quad (36)$$

$$\mathbf{A}_{41} \cdot \mathbf{v}_1 = \mathbf{0} = [0 \mid 0]^T \quad (47)$$

$$\mathbf{A}_{33} = \begin{bmatrix} 1 & 0 & -(y_{O_4} - y_{O_3}) \\ 0 & 1 & (x_{O_4} - x_{O_3}) \end{bmatrix} \quad (37)$$

$$\mathbf{A}_{54} \cdot \mathbf{v}_4 = \mathbf{0} = [0 \mid 0]^T \quad (48)$$

$$\mathbf{v}_3 = [v_{O_3x} \mid v_{O_3y} \mid \omega_{3z}]^T \quad (38)$$

$$\mathbf{A}_{41} = \begin{bmatrix} 1 & 0 & 0 \\ 0 & 1 & 0 \end{bmatrix} \quad (49)$$

$$\mathbf{A}_{34} = \begin{bmatrix} -1 & 0 \\ 0 & -1 \end{bmatrix} \quad (39)$$

$$\mathbf{A}_{54} = \begin{bmatrix} 1 & 0 \\ 0 & 1 \end{bmatrix} \quad (50)$$

$$\mathbf{v}_4 = [v_{O_4x} \mid v_{O_4y}]^T \quad (40)$$

The relationships (11), (23), (36) and (48) may be written together in matrix form as follows:

The elements “1” and “3” are linked to fixed element in O_1 and O_4 points respectively. Because of this their velocities will be equal to zero throughout the movement. In mathematical form that will be expressed as follows:

$$\mathbf{A} \cdot \mathbf{v} = \mathbf{0} = [0 \dots 0]^T \quad (51)$$

$$\mathbf{v}_{O_1} = [v_{O_1x} \mid v_{O_1y}]^T = \mathbf{0} = [0 \mid 0]^T \quad (41)$$

$$\mathbf{v}_{O_4} = [v_{O_4x} \mid v_{O_4y}]^T = \mathbf{0} = [0 \mid 0]^T \quad (42)$$

$$\mathbf{A} = \begin{bmatrix} \mathbf{A}_{11} & \mathbf{A}_{12} & \mathbf{0} & \mathbf{0} \\ \mathbf{0} & \mathbf{A}_{22} & \mathbf{A}_{23} & \mathbf{0} \\ \mathbf{0} & \mathbf{0} & \mathbf{A}_{33} & \mathbf{A}_{34} \\ \mathbf{A}_{41} & \mathbf{0} & \mathbf{0} & \mathbf{0} \\ \mathbf{0} & \mathbf{0} & \mathbf{0} & \mathbf{A}_{54} \end{bmatrix} \quad (52)$$

The matrix relations (41) and (42) are equivalent to the following scalar relationships:

$$\mathbf{v} = [\mathbf{v}_1^T \mid \mathbf{v}_2^T \mid \mathbf{v}_3^T \mid \mathbf{v}_4^T]^T \quad (53)$$

At the matrix relation (51) the following scalar relation will be added:

$$\omega_{1z} = \omega_{10} + \varepsilon_{10} \cdot t \quad (54)$$

The scalar relationship (54) may be written in matrix form as follows:

$$\mathbf{B} \cdot \mathbf{v} = \omega_{10} + \varepsilon_{10} \cdot t \quad (55)$$

$$\mathbf{B} = [0 \ 0 \ 1 \ 0 \ 0 \ 0 \ 0 \ 0 \ 0 \ 0 \ 0 \ 0] \quad (56)$$

The matrix relationships (51) and (55) may be written together in matrix form as follows:

$$\mathbf{C} \cdot \mathbf{v} = \mathbf{D} \cdot (\omega_{10} + \varepsilon_{10} \cdot t) \quad (57)$$

$$\mathbf{C} = [\mathbf{A}^T \ \mathbf{B}^T]^T \quad (58)$$

$$\mathbf{D} = [0 \ 0 \ 0 \ 0 \ 0 \ 0 \ 0 \ 0 \ 0 \ 0 \ 0 \ 1]^T \quad (59)$$

Using the matrix relationship (57) in the next chapter we will establish the differential equations that characterize the movement of the mechanism from a cinematic point of view.

3. ESTABLISHING THE DIFFERENTIAL EQUATIONS DESCRIBING THE CINEMATIC OF THE ARTICULATED QUADRILATERAL MECHANISM

In order to determine that cinematically characterize the movement of the articulated quadrilateral mechanism, we will derive the matrix relation (57) twice in relation to time and we will obtain:

$$\mathbf{C} \cdot \dot{\mathbf{v}} + \dot{\mathbf{C}} \cdot \mathbf{v} = \mathbf{D} \cdot \varepsilon_{10} \quad (60)$$

$$\mathbf{C} \cdot \ddot{\mathbf{v}} + 2 \cdot \dot{\mathbf{C}} \cdot \dot{\mathbf{v}} + \ddot{\mathbf{C}} \cdot \mathbf{v} = \underset{11 \times 1}{\mathbf{0}} \quad (61)$$

$$\dot{\mathbf{C}} = [\dot{\mathbf{A}}^T \ \dot{\mathbf{B}}^T]^T \quad (62)$$

$$\dot{\mathbf{B}} = \underbrace{[0 \ 0 \ 0 \ 0 \ 0 \ 0 \ 0 \ 0 \ 0 \ 0 \ 0 \ 0]}_{1 \times 11} \quad (63)$$

$$\dot{\mathbf{A}} = \begin{bmatrix} \dot{\mathbf{A}}_{11} & \dot{\mathbf{A}}_{12} & \mathbf{0} & \mathbf{0} \\ \mathbf{0} & \dot{\mathbf{A}}_{22} & \dot{\mathbf{A}}_{23} & \mathbf{0} \\ \mathbf{0} & \mathbf{0} & \dot{\mathbf{A}}_{33} & \dot{\mathbf{A}}_{34} \\ \dot{\mathbf{A}}_{41} & \mathbf{0} & \mathbf{0} & \mathbf{0} \\ \mathbf{0} & \mathbf{0} & \mathbf{0} & \dot{\mathbf{A}}_{54} \end{bmatrix} \quad (64)$$

$$\dot{\mathbf{A}}_{11} = \begin{bmatrix} 0 & 0 & -(v_{O_2y} - v_{O_1y}) \\ 0 & 0 & (v_{O_2x} - v_{O_1x}) \end{bmatrix} \quad (65)$$

$$\dot{\mathbf{A}}_{12} = \begin{bmatrix} 0 & 0 & 0 \\ 0 & 0 & 0 \end{bmatrix} = \underset{2 \times 3}{\mathbf{0}} \quad (66)$$

$$\dot{\mathbf{A}}_{22} = \begin{bmatrix} 0 & 0 & -(v_{O_3y} - v_{O_2y}) \\ 0 & 0 & (v_{O_3x} - v_{O_2x}) \end{bmatrix} \quad (67)$$

$$\dot{\mathbf{A}}_{23} = \begin{bmatrix} 0 & 0 & 0 \\ 0 & 0 & 0 \end{bmatrix} = \underset{2 \times 3}{\mathbf{0}} \quad (68)$$

$$\dot{\mathbf{A}}_{33} = \begin{bmatrix} 0 & 0 & -(v_{O_4y} - v_{O_3y}) \\ 0 & 0 & (v_{O_4x} - v_{O_3x}) \end{bmatrix} \quad (69)$$

$$\dot{\mathbf{A}}_{34} = \begin{bmatrix} 0 & 0 \\ 0 & 0 \end{bmatrix} = \underset{2 \times 2}{\mathbf{0}} \quad (70)$$

$$\dot{\mathbf{A}}_{41} = \begin{bmatrix} 0 & 0 & 0 \\ 0 & 0 & 0 \end{bmatrix} = \underset{2 \times 3}{\mathbf{0}} \quad (71)$$

$$\dot{\mathbf{A}}_{54} = \begin{bmatrix} 0 & 0 \\ 0 & 0 \end{bmatrix} = \underset{2 \times 2}{\mathbf{0}} \quad (72)$$

$$\ddot{\mathbf{C}} = [\ddot{\mathbf{A}}^T \mid \ddot{\mathbf{B}}^T]^T \quad (73)$$

$$\ddot{\mathbf{B}} = \underbrace{[0 \mid 0 \mid 0]}_{1 \times 11} \quad (74)$$

$$\ddot{\mathbf{A}} = \begin{bmatrix} \ddot{\mathbf{A}}_{11} & \ddot{\mathbf{A}}_{12} & \mathbf{0} & \mathbf{0} \\ \mathbf{0} & \ddot{\mathbf{A}}_{22} & \ddot{\mathbf{A}}_{23} & \mathbf{0} \\ \mathbf{0} & \mathbf{0} & \ddot{\mathbf{A}}_{33} & \ddot{\mathbf{A}}_{34} \\ \ddot{\mathbf{A}}_{41} & \mathbf{0} & \mathbf{0} & \mathbf{0} \\ \mathbf{0} & \mathbf{0} & \mathbf{0} & \ddot{\mathbf{A}}_{54} \end{bmatrix} \quad (75)$$

$$\ddot{\mathbf{A}}_{11} = \begin{bmatrix} 0 & 0 & -(a_{O_2y} - a_{O_1y}) \\ 0 & 0 & (a_{O_2x} - a_{O_1x}) \end{bmatrix} \quad (76)$$

$$\ddot{\mathbf{A}}_{12} = \begin{bmatrix} 0 & 0 & 0 \\ 0 & 0 & 0 \end{bmatrix} = \mathbf{0}_{2 \times 3} \quad (77)$$

$$\ddot{\mathbf{A}}_{22} = \begin{bmatrix} 0 & 0 & -(a_{O_3y} - a_{O_2y}) \\ 0 & 0 & (a_{O_3x} - a_{O_2x}) \end{bmatrix} \quad (78)$$

$$\ddot{\mathbf{A}}_{23} = \begin{bmatrix} 0 & 0 & 0 \\ 0 & 0 & 0 \end{bmatrix} = \mathbf{0}_{2 \times 3} \quad (79)$$

$$\ddot{\mathbf{A}}_{33} = \begin{bmatrix} 0 & 0 & -(a_{O_4y} - a_{O_3y}) \\ 0 & 0 & (a_{O_4x} - a_{O_3x}) \end{bmatrix} \quad (80)$$

$$\ddot{\mathbf{A}}_{34} = \begin{bmatrix} 0 & 0 \\ 0 & 0 \end{bmatrix} = \mathbf{0}_{2 \times 2} \quad (81)$$

$$\ddot{\mathbf{A}}_{41} = \begin{bmatrix} 0 & 0 & 0 \\ 0 & 0 & 0 \end{bmatrix} = \mathbf{0}_{2 \times 3} \quad (82)$$

$$\ddot{\mathbf{A}}_{54} = \begin{bmatrix} 0 & 0 \\ 0 & 0 \end{bmatrix} = \mathbf{0}_{2 \times 2} \quad (83)$$

$$\dot{\mathbf{v}} = [\dot{\mathbf{v}}_1^T \mid \dot{\mathbf{v}}_2^T \mid \dot{\mathbf{v}}_3^T \mid \dot{\mathbf{v}}_4^T]^T = \mathbf{a} \quad (84)$$

$$\mathbf{a} = [\mathbf{a}_1^T \mid \mathbf{a}_2^T \mid \mathbf{a}_3^T \mid \mathbf{a}_4^T]^T \quad (85)$$

$$\mathbf{a}_1 = [a_{O_1x} \mid a_{O_1y} \mid \varepsilon_{1z}]^T \quad (86)$$

$$\mathbf{a}_2 = [a_{O_2x} \mid a_{O_2y} \mid \varepsilon_{2z}]^T \quad (87)$$

$$\mathbf{a}_3 = [a_{O_3x} \mid a_{O_3y} \mid \varepsilon_{3z}]^T \quad (88)$$

$$\mathbf{a}_4 = [a_{O_4x} \mid a_{O_4y}]^T \quad (89)$$

$$\ddot{\mathbf{v}} = [\ddot{\mathbf{v}}_1^T \mid \ddot{\mathbf{v}}_2^T \mid \ddot{\mathbf{v}}_3^T \mid \ddot{\mathbf{v}}_4^T]^T = \dot{\mathbf{a}} \quad (90)$$

$$\dot{\mathbf{a}} = [\dot{\mathbf{a}}_1^T \mid \dot{\mathbf{a}}_2^T \mid \dot{\mathbf{a}}_3^T \mid \dot{\mathbf{a}}_4^T]^T \quad (91)$$

$$\dot{\mathbf{a}}_1 = [\dot{a}_{O_1x} \mid \dot{a}_{O_1y} \mid \dot{\varepsilon}_{1z}]^T \quad (92)$$

$$\dot{\mathbf{a}}_2 = [\dot{a}_{O_2x} \mid \dot{a}_{O_2y} \mid \dot{\varepsilon}_{2z}]^T \quad (93)$$

$$\dot{\mathbf{a}}_3 = [\dot{a}_{O_3x} \mid \dot{a}_{O_3y} \mid \dot{\varepsilon}_{3z}]^T \quad (94)$$

$$\dot{\mathbf{a}}_4 = [\dot{a}_{O_4x} \mid \dot{a}_{O_4y}]^T \quad (95)$$

In the relationship (91) the elements of the $\dot{\mathbf{a}}$ column matrix represents the second order accelerations. They represent the variations of the accelerations during a certain period of time. The system of the second order differential equations (61) will be transformed into a system of differential equations of the first order. In order to do this, the following notation will be inserted:

$$\dot{\mathbf{v}} = \mathbf{a} \quad (96)$$

By replacing relationship (96) in the matrix relationship (61) we will obtain:

$$\mathbf{C} \cdot \dot{\mathbf{a}} + 2 \cdot \dot{\mathbf{C}} \cdot \mathbf{a} + \ddot{\mathbf{C}} \cdot \mathbf{v} = \underset{11 \times 1}{\mathbf{0}} \quad (97)$$

$$l_2 = 3 [\text{meters}] \quad (105)$$

$$l_3 = 4 [\text{meters}] \quad (106)$$

$$l_4 = 5 [\text{meters}] \quad (107)$$

$$\omega_1 = 10 [\text{radians / sec.}] = \text{const.} \quad (108)$$

$$\dot{\mathbf{x}} = \mathbf{v} \quad (98)$$

The initial conditions characterizing the configuration of the mechanism are as follows:

In the matrix relationship (98) the column matrix $\dot{\mathbf{x}}$ will be written as follows:

$$\dot{\mathbf{x}} = [\dot{\mathbf{x}}_1^T \mid \dot{\mathbf{x}}_2^T \mid \dot{\mathbf{x}}_3^T \mid \dot{\mathbf{x}}_4^T]^T \quad (99)$$

$$x_{O_1}^0 = 0 [\text{meters}] \quad (109)$$

$$y_{O_1}^0 = 0 [\text{meters}] \quad (110)$$

$$\dot{\mathbf{x}}_1 = [\dot{x}_{O_1} \mid \dot{y}_{O_1} \mid \dot{\phi}_{1z}]^T \quad (100)$$

$$\phi_1^0 = 0 [\text{radians}] \quad (111)$$

$$\dot{\mathbf{x}}_2 = [\dot{x}_{O_2} \mid \dot{y}_{O_2} \mid \dot{\phi}_{2z}]^T \quad (101)$$

$$x_{O_2}^0 = 1 [\text{meters}] \quad (112)$$

$$\dot{\mathbf{x}}_3 = [\dot{x}_{O_3} \mid \dot{y}_{O_3} \mid \dot{\phi}_{3z}]^T \quad (102)$$

$$y_{O_2}^0 = 0 [\text{meters}] \quad (113)$$

$$\dot{\mathbf{x}}_4 = [\dot{x}_{O_4} \mid \dot{y}_{O_4}]^T \quad (103)$$

$$\phi_2^0 = 1.1864 [\text{radians}] \quad (114)$$

The matrix relationships (96), (97) and (98) form together a system of thirty three differential equations having thirty three unknowns.

$$x_{O_3}^0 = 2.125 [\text{meters}] \quad (115)$$

4. INTEGRATING THE SYSTEM OF DIFFERENTIAL EQUATIONS AND OBTAINING THE RESULTS

$$y_{O_3}^0 = 2.7810744 [\text{meters}] \quad (116)$$

The system of differential equations expressed by the matrix relationships (96), (97) and (98) will be integrated using numerical integration methods. To do this, using MATLAB software a computational program that integrates the differential equations system mentioned above was designed. In order to run the program the following input data are required:

$$\phi_3^0 = -0.7688 [\text{radians}] \quad (117)$$

$$x_{O_4}^0 = 5 [\text{meters}] \quad (118)$$

$$y_{O_4}^0 = 0 [\text{meters}] \quad (119)$$

$$l_1 = 1 [\text{meters}] \quad (104)$$

The initial conditions concerning the velocities, the first order kinematical parameters, are the followings:

$$v_{O_1x}^0 = 0 \text{ [meters / sec.]} \quad (120)$$

$$v_{O_1y}^0 = 0 \text{ [meters / sec.]} \quad (121)$$

$$\omega_{1z}^0 = 10 \text{ [radians / sec.]} \quad (122)$$

$$v_{O_2x}^0 = 0 \text{ [meters / sec.]} \quad (123)$$

$$v_{O_2y}^0 = 10 \text{ [meters / sec.]} \quad (124)$$

$$\omega_{2z}^0 = -2.5 \text{ [radians / sec.]} \quad (125)$$

$$v_{O_3x}^0 = 6.95268 \text{ [meters / sec.]} \quad (126)$$

$$v_{O_3y}^0 = 7.1875 \text{ [meters / sec.]} \quad (127)$$

$$\omega_{3z}^0 = -2.5 \text{ [radians / sec.]} \quad (128)$$

$$v_{O_4x}^0 = 0 \text{ [meters / sec.]} \quad (129)$$

$$v_{O_4y}^0 = 0 \text{ [meters / sec.]} \quad (130)$$

As for accelerations, the second order kinematical parameters, the following initial conditions are required::

$$a_{O_1x}^0 = 0 \text{ [meters / sec}^2\text{]} \quad (131)$$

$$a_{O_1y}^0 = 0 \text{ [meters / sec}^2\text{]} \quad (132)$$

$$\varepsilon_{1z}^0 = 0 \text{ [radians / sec}^2\text{]} \quad (133)$$

$$a_{O_2x}^0 = -100 \text{ [meters / sec}^2\text{]} \quad (134)$$

$$a_{O_2y}^0 = 0 \text{ [meters / sec}^2\text{]} \quad (135)$$

$$\varepsilon_{2z}^0 = -32.30541 \text{ [radians / sec}^2\text{]} \quad (136)$$

$$a_{O_3x}^0 = -17.1875 \text{ [meters / sec}^2\text{]} \quad (137)$$

$$a_{O_3y}^0 = -53.7253 \text{ [meters / sec}^2\text{]} \quad (138)$$

$$\varepsilon_{3z}^0 = 12.6412 \text{ [radians / sec}^2\text{]} \quad (139)$$

$$a_{O_4x}^0 = 0 \text{ [meters / sec}^2\text{]} \quad (140)$$

$$a_{O_4y}^0 = 0 \text{ [meters / sec}^2\text{]} \quad (141)$$

Following integration, the results shown in the figures below are obtained (Fig.2, Fig.3, Fig.4, Fig.5).At the initial moment, the leading element of the mechanism is considered at rest. One can see that the ϕ_{1z} angular parameter varies linearly with respect to time since it was considered from the beginning that the leading element “1” describes a uniform rotation motion around the O_1z axis. For this reason, the angular velocity of the leading element has a constant value throughout the movement. It can also be observed that the O_2 point describes a circular uniform motion around the O_1z axis. The variation of the kinematical parameters of the “2” element in relation to time is shown in figure 3 (Fig.3).Figure 4 presents the variation with respect to time of the “3” element kinematical parameters. It may be observed that the third element of the mechanism describes an oscillatory rotational motion around the Oz axis. Analyzing figure 5 (Fig.5) it may be observed that the kinematical parameters of O_4 point are constant throughout the movement since it is considered to be fix.

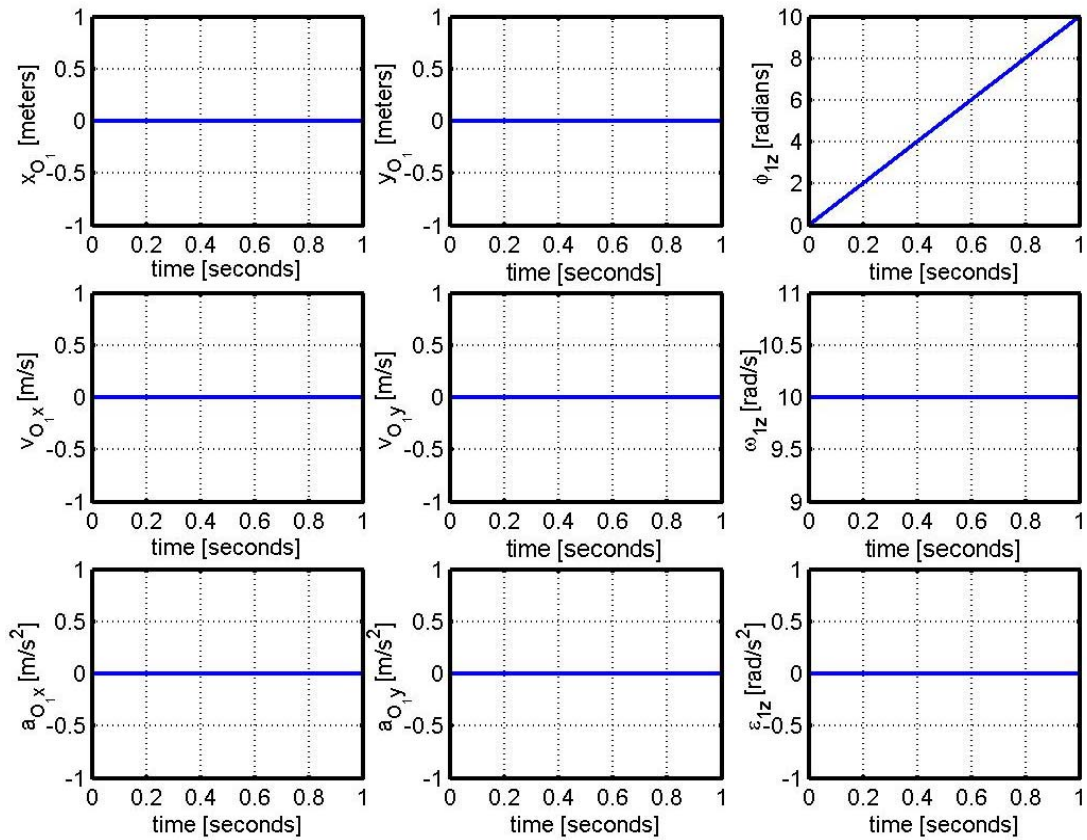


Figure 2. Variations of the kinematical parameters of the “1” element with respect to time

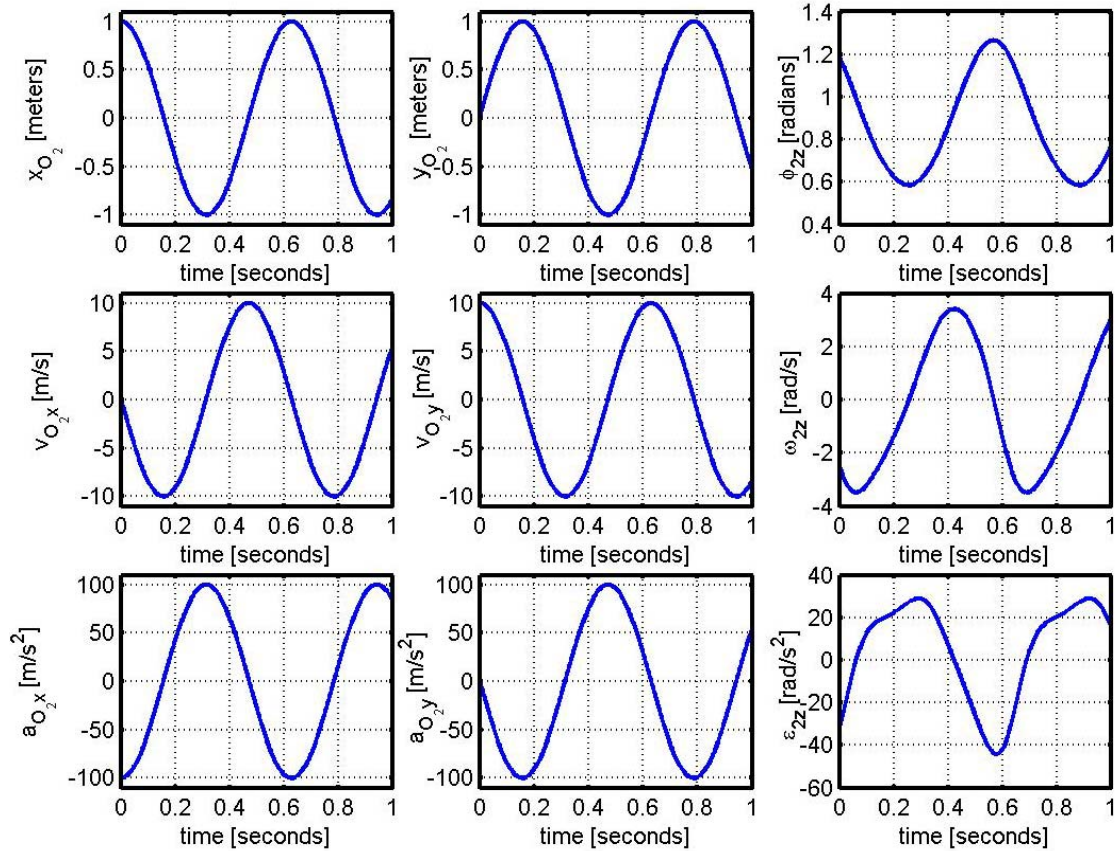


Figure 3. Variation of the kinematical parameters of the “2” element with respect to time

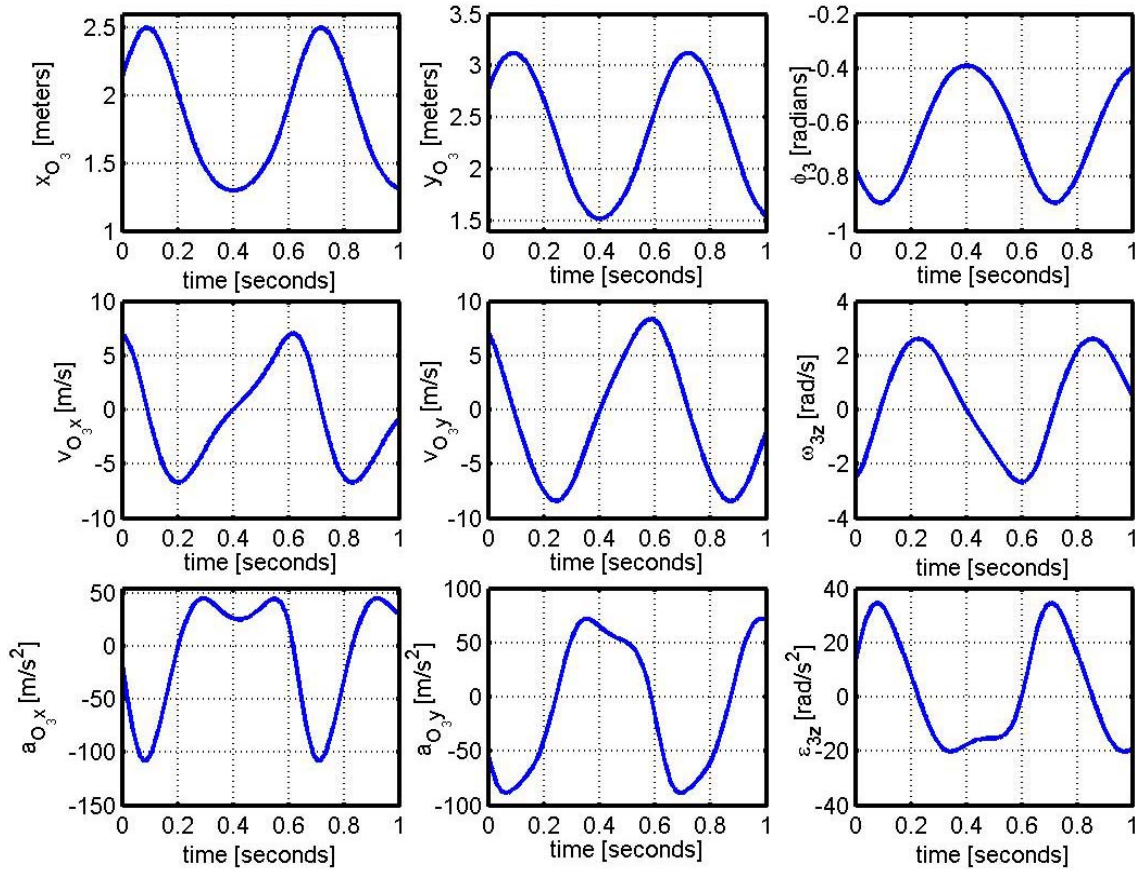


Figure 4. Variation of the kinematical parameters of the "3" element with respect to time

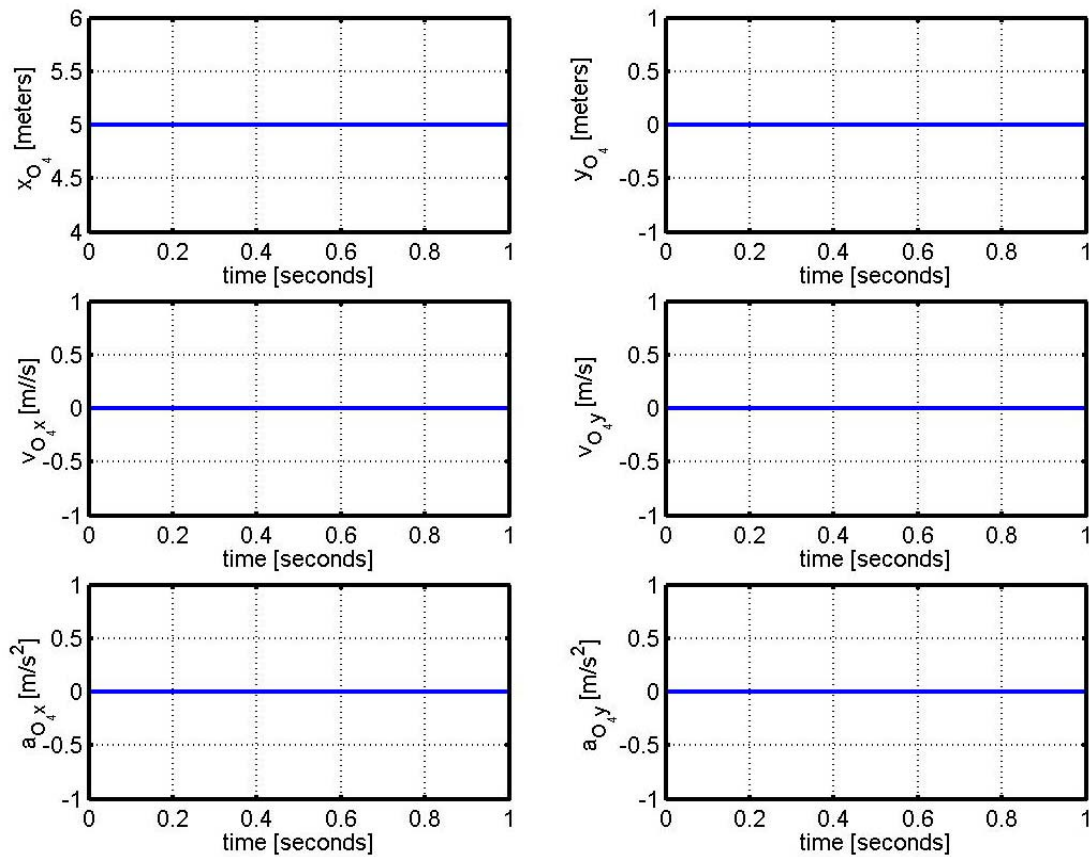


Figure 5. Variation of the kinematical parameters of the O_4 point with respect to time

The case when the leading element of the mechanism describes a uniform rotational motion was considered.

5. CONCLUSIONS

The numerical method presented in the paper is based on Euler's relations concerning the distribution of velocities written in projections on the fixed reference system axes. Using the numerical method presented in the paper the variation in relation to time of the displacements, speeds and accelerations can be determined.

REFERENCES

- [1] Vălcovici V., Bălan V., Voinea R., Mecanica Teoretică, Editura Tehnică, București, 1968
- [2] Viorel Handra Luca, Ion Aurel Stoica, Introducere in teoria mecanismelor, vol.I, pp.84, Editura Dacia Cluj-Napoca 1982
- [3] Christian Pelecudi, Dezideriu Maroș, Vasile Merticaru, Nicolae Pandrea, Ion Simionescu, Mecanisme, pp.206-208, Editura Tehnică, 1983
- [4] Voinea R., Stroe I., A general method for kinematics pairs synthesis, Mechanism and Machine Theory, Elsevier, 30(3), pp. 461-470, 1995
- [5] Ștefan Staicu, Mecanica Teoretică.,Editura Didactică și Pedagogică București R.A., 1998
- [6] Florin Baușic, Mecanica Teoretică.Cinemática, Editura Conspress, București, 2004
- [7] Staicu S., Kinematics of translation-rotation parallel robot, Romanian Journal of Technical Sciences-Applied Mechanics, 60, pp. 171-183, 2015
- [8] Tătaru V.D., Tătaru M.B., Incremental numerical method used for the cinematic analysis of the four-bar linkage mechanism, Romanian Journal of Technical Sciences-Applied Mechanics, 61(3), pp. 221-231, 2016

MATHEMATICAL METHOD TO UNFOLDING COUPLINGS

Carmen POPA¹, Ivona PETRE¹, Ruxandra-Elena BRATU²

¹ Valahia University Targoviste, Romania, ² Politehnica University of Bucharest

E-mail: carmenpopa2001@yahoo.com

Abstract: The purpose of this paper is to establish the intersection curves between cylinders, using Mathematica program. The equations curves which are inferred by mathematical methods are introduced in this program. This paper takes into discussion the case of four cylinders.

Keywords: unfolding, coupling, Mathematica program

1. INTRODUCTION

The transition elements or couplings are met in all the industrial and of pipes equipments and they are formed from intersections of pieces with thin or thick walls. In practice is necessary to know their unfolding, to obtain these couplings using the welding technological process. This paper proposes to establish the unfolded curves of one of this coupling, using a different proceeding against the classical method of descriptive geometry.

2. CONTENTS

The characteristics of the cylinders are presented in the figure 1. The transition element presented in the figure 1 is met in pneumatic equipments. This coupling makes connection between pipes with displaced parallel axes.

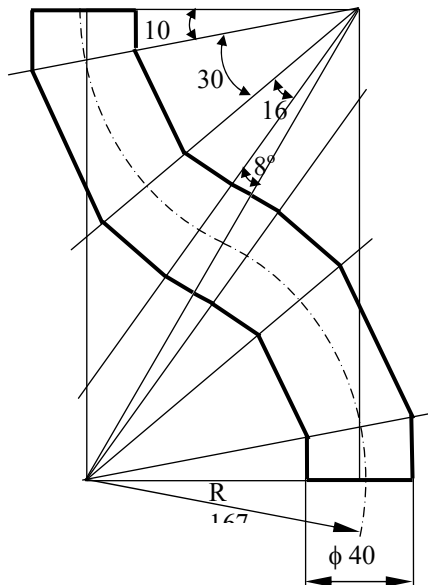


Figure 1. Coupling

For the first cylinder, presented in the figure 2, the transformation curve equation, is obtain by applying the relations (2), (3) to the equation (1), [1,2].

$$\sin 10 = \frac{AB}{OA} = AB = 167 \cdot \sin 10 = 28,9992$$

$$z = (x+R) \operatorname{tg} \beta, x \in [-R, R] \tag{1}$$

$$x = R \sin \alpha \tag{2}$$

$$z = z_d, \alpha \in [0, 2\pi] \tag{3}$$

$$\begin{aligned} m t = x_d = R \alpha \\ x = R \sin (x_d/R) \\ z = z_d \end{aligned}$$

We obtain:

$$z_d = \operatorname{tg} \beta \left(R \sin \frac{x_d}{R} + R \right), x_d \in [0, 2\pi R] \tag{4}$$

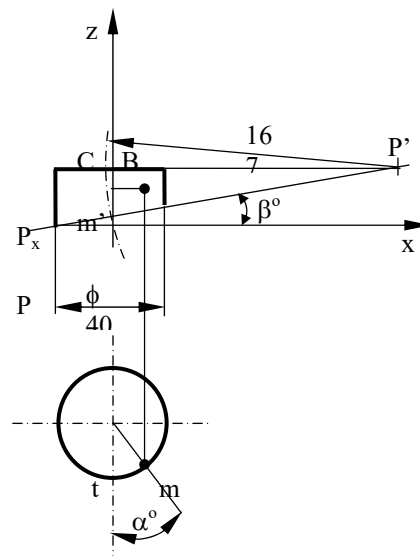


Figure 2. Base cylinder

For an angle $\beta = 10^\circ$ and a cylinder radius $R = 20$, we have the figure 3, by introducing the equation (4) into Mathematica program [3,4,5].

$$z_d = \operatorname{tg} 10^\circ \left(20 \sin \frac{x_d}{20} + 20 \right), x_d \in [0, \pi 40]$$

Plot[{Tan[10Degree]*(20*Sin[xd/20]+20)}, {xd,0,Pi*40}]]

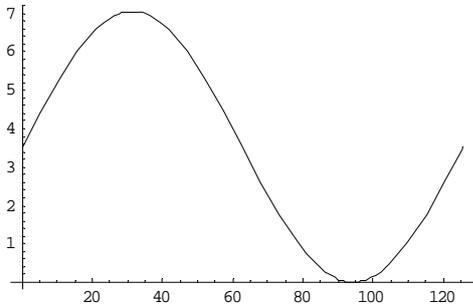


Figure 3. The unfolding cylinder for $\beta = 10^\circ$

For an angle $\beta = 17^\circ$, respectively 13° and a radius of cylinder, $R = 20$, we obtain the figure 4 and 5, by introducing the equation (4) into Mathematica program.

$$z_d = \operatorname{tg} 13^\circ \left(20 \sin \frac{x_d}{20} + 20 \right), x_d \in [0, \pi 40]$$

$$z_d = \operatorname{tg} 17^\circ \left(20 \sin \frac{x_d}{20} + 20 \right), x_d \in [0, \pi 40]$$

Plot[{Tan[13Degree]*(20*Sin[xd/20]+20)}, {xd,0,Pi*40}]]

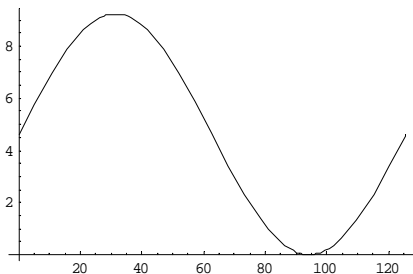


Figure 4. The unfolding cylinder for $\beta = 13^\circ$

Plot[{Tan[17Degree]*(20*Sin[xd/20]+20)}, {xd,0,Pi*40}]]

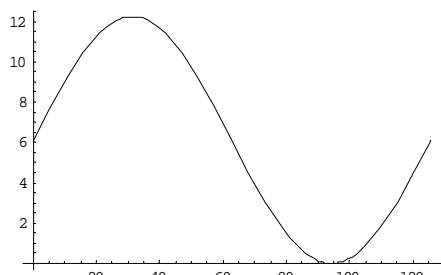


Figure 5. The unfolding cylinder for $\beta = 17^\circ$

The third cylinder, for an angle $\beta = 8^\circ$ and a radius of cylinder $R = 20$, we obtain the figure 6, by introducing the equation (4) into Mathematica program.

$$z_d = \operatorname{tg} 8^\circ \left(20 \sin \frac{x_d}{20} + 20 \right), x_d \in [0, \pi 40]$$

Plot[{Tan[8Degree]*(20*Sin[xd/20]+20)}, {xd,0,Pi*40}]]

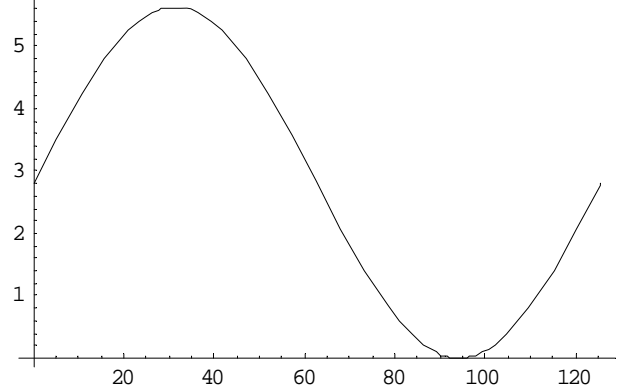


Figure 6. The unfolding cylinder for $\beta = 8^\circ$

The fourth cylinder, for an angle $\beta = 4^\circ$ and a radius of cylinder $R = 20$, we obtain the figure 7, by introducing the equation (4) into Mathematica program.

$$z_d = \operatorname{tg} 4^\circ \left(20 \sin \frac{x_d}{20} + 20 \right), x_d \in [0, \pi 40]$$

Plot[{Tan[4Degree]*(20*Sin[xd/20]+20)}, {xd,0,Pi*40}]]

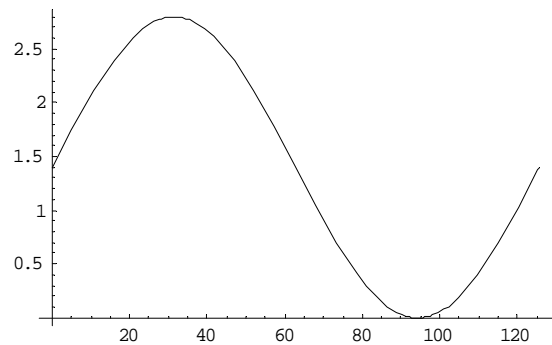


Figure 7. The unfolding cylinder for $\beta = 4^\circ$

3. CONCLUSIONS

The presented method is very speedy and exactly and following the program we can obtain the unfoldings of cylinders for any other dimensions.

REFERENCES

- [1] Vlasov, A. K.: Curs de matematică superioară, Editura Tehnică, Timișoara, 1971;
- [2] Ivănceanu, T., Șofroneșcu, E., Buzilă, V.: Geometrie descriptivă și desen tehnic, Editura Didactică și Pedagogică, București, 1979;
- [3]**Release notes Matematica Program.
- [4] Popa, Carmen, Petre, Ivona: Mathematical methods to determinate the intersection curves of the cylinders, International Conference on Manufacturing Systems ICMS, București, 2004, tome 49, p. 595, ISBN 973-27-1102-7, ISSN 0035-4074
- [5] Popa, Carmen: Mathematical method to unfold an oblique pyramid, Modelling and optimization in the machines building field, Bacau, 2004, vol I, 40.